ABSTRACT

Title of Thesis: THE DYNAMIC CHARACTERIZATION OF IMPACT-MITIGATING MATERIALS USING ELECTROMAGNETIC VELOCITY GAUGES

Garrett Scott Wiles, Master of Science, 2020

Thesis Directed By: Dr. William L. Fourney

Professor of Mechanical and Aerospace Engineering

The use of certain polymers is actively being examined as means to passively reduce the damaging effects of impact loading. With uncertainty of the dynamic environments in which these materials achieve optimal performance, a further investigation is necessary to analyze the dynamic behavior of the viscoelastic material as loading rate varies. This study was conducted using a polymeric Split-Hopkinson pressure bar while using electromagnetic velocity gauges for measuring stress-strain data to obtain material characteristics of the test specimens. Frequency domain characteristics were obtained by fitting a rheological model to test data. Strain-rates observed during the study were on the order of 10^3 s^{-1}. A polymeric Split-Hopkinson pressure bar was used instead of a conventional elastic bar to reduce the impedance mismatch with the test specimens. Electromagnetic velocity gauges were employed to justifiably neglect the dispersion and attenuation effects that accompany the use of viscoelastic bars.

THE DYNAMIC CHARACTERIZATION OF IMPACT-MITIGATING MATERIALS USING ELECTROMAGNETIC VELOCITY GAUGES

by

Garrett Scott Wiles

Thesis submitted to the Faculty of the Graduate School of the
University of Maryland, College Park, in partial fulfillment
of the requirements for the degree of
Master of Science
2020

Advisory Committee:
Professor William L. Fourney, Chair
Professor Balakumar Balachandran
Professor Amr M. S. Baz

I. Acknowledgements

I would like to acknowledge and thank the U.S. Navy STEM Student Employment Program (SSEP) and its associates at the Naval Surface Warfare Center, Dahlgren Division for supporting me and helping fund my education at the University of Maryland, College Park. Furthermore, I would like to thank Dr. Daniel Casem and Dr. Amr Baz for their kind feedback throughout this research process.

To Dr. Fourney, thank you for the gracious opportunity for me to pursue research in the Dynamic Effects Laboratory. I am fortunate to have been surrounded by such thoughtful individuals with whom I share a similar passion for engineering.

To my wonderful family, my successes continue to be a result of your ever-present encouragement and love.

In loving memory of my grandfather, Meredith “Pop” Wisner.

II. Table of Contents

III. List of Tables

IV. List of Figures

V. List of Abbreviations

AWG: American Wire Gauge

BNC: Bayonet Neill-Concelman

BSP: Boltzmann Superposition Principle

DAQ: Data Acquisition System

GMM: Generalized Maxwell Model

Op-Amp: Operational Amplifier

SHPB: Split-Hopkinson Pressure Bar

QLV: Quasilinear Viscoelasticity

1. Overview of the Conventional Split-Hopkinson Pressure Bar

1.1 Introduction

Historically, the conventional Split-Hopkinson pressure bar (SHPB) is accredited to Kolsky when he utilized a split bar test setup for recording material stress-strain data from stress wave measurements [1]. Kolsky's work follows single bar methods for measuring stress waves established by Hopkinson and Davies [2,3]. Among Kolsky [4], there are others whose work is widely referenced for understanding longitudinal wave propagation in bars and the common SHPB test [5,6]. Although a non-traditional SHPB test method was used for characterizing material in this study, it is essential to first understand the theory behind the conventional SHPB test. This chapter will first review wave theory through elastic, uniform cross-section bars and then apply the derived findings to the conventional SHPB.

1.2 Conventional SHPB Theory

1.2.1 *Longitudinal Waves in Uniform Cross-Section Bars*

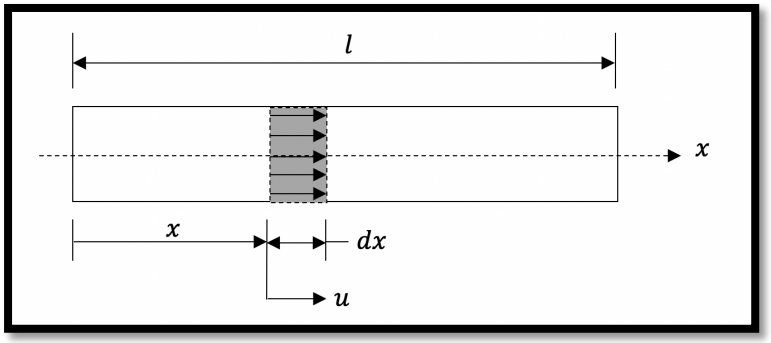

Figure 1.1: Longitudinal motion through a uniform cross-section bar.

To understand the theory behind the commonly used linear-elastic Split-Hopkinson pressure bar, it is first necessary to understand how longitudinal waves

propagate through a bar with uniform cross-sectional area. First, consider a long, thin, and dispersion-free linear-elastic bar of length l as seen in *Figure 1.1*. The bar's axial displacement is represented by u. The kinetic energy of the bar is given by the following equation:

$$T = \frac{1}{2}\int_0^l m\dot{u}^2 dx \tag{1.1}$$

where m is the mass per unit length. Rewriting the linear density in terms of the volumetric density ρ and constant cross-sectional area A gives:

$$T = \frac{1}{2}\rho A\int_0^l \dot{u}^2 dx \tag{1.2}$$

The potential energy of the bar is written in terms of axial stress σ, strain ε, and cross-sectional area. It is then rewritten using the relationship between stress, Young's modulus E, and strain as seen below.

$$V = \frac{1}{2}\int_0^l \sigma\varepsilon A dx = \frac{1}{2}\int_0^l (E\varepsilon)\varepsilon A dx = \frac{1}{2}EA\int_0^l \varepsilon^2 dx \tag{1.3}$$

Recognizing that the strain of the bar is the partial differentiation of u with respect to x leads to the equation:

$$V = \frac{1}{2}EA\int_0^l \left(\frac{\partial u}{\partial x}\right)^2 dx \tag{1.4}$$

The Lagrangian and the variation of the Lagrangian are given by:

$$\mathcal{L} = T - V = \frac{1}{2}\int_0^l \rho A\dot{u}^2 dx - \frac{1}{2}\int_0^l EA\left(\frac{\partial u}{\partial x}\right)^2 dx \tag{1.5}$$

$$\delta\mathcal{L} = \int_0^l \rho A\ddot{u}\delta\dot{u} dx - \int_0^l EA\left(\frac{\partial u}{\partial x}\right)\delta\left(\frac{\partial u}{\partial x}\right) dx \tag{1.6}$$

Applying the extended Hamilton's principle [7] to acquire the equation of motion yields:

$$\int_{t_1}^{t_2} \delta\mathcal{L}\, dt = 0 \tag{1.7}$$

$$\int_{t_1}^{t_2} \delta\mathcal{L}\, dt = \int_{t_1}^{t_2} \left[\int_0^l \rho A \ddot{u} \delta \ddot{u} dx - \int_0^l EA \left(\frac{\partial u}{\partial x}\right) \delta \left(\frac{\partial u}{\partial x}\right) dx \right] dt = 0$$

$$\int_{t_1}^{t_2} \delta\mathcal{L}\, dt = \int_{t_1}^{t_2} \left[\int_0^l -\rho A \ddot{u} \delta u dx - EA \left(\frac{\partial u}{\partial x}\right) \delta u \Big|_0^l + \int_0^l \frac{\partial}{\partial x} EA \left(\frac{\partial u}{\partial x}\right) \delta u dx \right] dt = 0 \quad (1.8)$$

with $\quad EA \left(\frac{\partial u}{\partial x}\right) \delta u \Big|_0^l = 0$

Here, the time from t_1 to t_2 represents some fixed time interval. The above equations imply that the following must be true:

$$\rho A \ddot{u} - \frac{\partial}{\partial x} EA \left(\frac{\partial u}{\partial x}\right) = 0$$

$$\text{or} \qquad \rho A \ddot{u} = \frac{\partial}{\partial x} \left[EA \left(\frac{\partial u}{\partial x}\right) \right] \quad (1.9)$$

Using the notation:

$$\frac{\partial \boxdot}{\partial x} = \boxdot_{,x} \quad ; \quad \frac{\partial^2 \boxdot}{\partial x^2} = \boxdot_{,xx} \quad ; \quad \frac{d \boxdot}{dx} = \boxdot_{x} \quad ; \quad \frac{d^2 \boxdot}{dx^2} = \boxdot_{xx}$$

and letting $c = \sqrt{\frac{E}{\rho}}$, which is the wave speed in the solid, alters *Equation 1.9* to the form:

$$\frac{1}{c^2} \ddot{u} = u_{,xx} \quad (1.10)$$

which is the familiar wave equation, and the equation of motion for the one-dimensional bar of uniform cross-section. Next, the separation of variables principle is used to express the axial displacement as:

$$u(x,t) = U(x)T(t) \quad (1.11)$$

where $U(x)$ is a spatial function of x, and $T(t)$ is the temporal function $T(t) = e^{i\omega t}$. ω represents the oscillation frequency of the longitudinal waves propagating through the bar. Applying the separation of variables principle to the bar's equation of motion gives:

$$\frac{1}{c^2}\ddot{T}U = U_{xx}T \tag{1.12}$$

Rearranging and substituting the temporal function into *Equation 1.12* yields the following relationship:

$$\frac{\ddot{T}}{T} = c^2\frac{U_{xx}}{U} = -\omega^2 \tag{1.13}$$

Let $k = \frac{\omega}{c}$ which, by definition, is the wave number. Then, the spatial equation of motion is given as:

$$U_{xx} + k^2U = 0 \tag{1.14}$$

The above ordinary differential equation has the solution:

$$U(x) = \left[Ae^{-ikx} + Be^{ikx}\right] \tag{1.15}$$

where A and B are constants. In space and time, the displacement u is:

$$u(x,t) = \left[Ae^{-ikx} + Be^{ikx}\right]e^{i\omega t} \tag{1.16}$$

where the first term refers to an outgoing wave and the second refers to an incoming wave. This wave displacement equation will be applied in the context of the conventional SHPB in the subsequent section.

1.2.2 *Stress-Strain Relations of the SHPB*

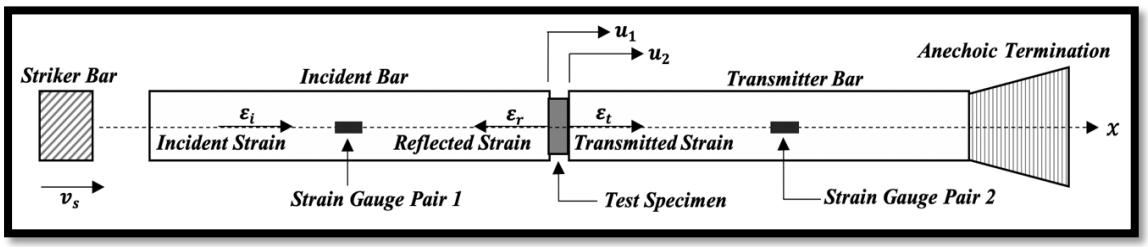

Figure 1.2: Conventional Split-Hopkinson pressure bar test setup.

The conventional Split-Hopkinson pressure bar, in its simplest description, consists of two separate linear-elastic cylindrical bars (rods) that are free to move axially.

A material specimen of interest is placed between the two bars, and when an axial wave is passed through the assembly, a portion of the wave gets reflected by the specimen and a portion of the wave continues. The reflection is due to a change in waveguide material from that of the bar to that of the test specimen. By measuring the magnitudes of these waves throughout the event, material properties of the test specimen can be determined.

The following analysis is based on Baz [8]. From the conventional Split-Hopkinson pressure bar setup shown in *Figure 1.2*, a striker bar, moving with velocity v_s, impacts an incident bar. The resulting wave displacement, u_1, in the incident bar is the sum of the displacement due to the incident (outgoing) wave and reflection (incoming) wave. From the previous analysis of wave motion through a uniform bar in *Section 1.2.1*, the displacement of the incident bar can be represented by:

$$u_1(x,t) = \left[Ae^{-ikx} + Be^{ikx}\right]e^{i\omega t} = u_i + u_r \tag{1.17}$$

where the subscripts *i* and *r* refer to the incident wave and reflection wave respectively. The incident strain is:

$$\varepsilon_1 = \frac{\partial u_1}{\partial x} = \left[-ikAe^{-ikx} + ikBe^{ikx}\right]e^{i\omega t} = \varepsilon_i + \varepsilon_r \tag{1.18}$$

The strain of the incident bar is typically measured by two diametrically opposed strain gauges, *Strain Gauge Pair 1* in *Figure 1.2*, at the bisection of the bar. In addition, a Wheatstone bridge circuit is implemented to negate the measurement of bar bending effects. The velocity of the incident bar can be found by differentiating *Equation 1.17* with respect to time t. The results are given by:

$$\dot{u}_1 = i\omega\left[Ae^{-ikx} + Be^{ikx}\right]e^{i\omega t} = \dot{u}_i + \dot{u}_r \tag{1.19}$$

Rewriting *Equation 1.19* in terms of the incident and reflection strains yields:

$$\dot{u}_1 = \dot{u}_i + \dot{u}_r = c(-\varepsilon_i + \varepsilon_r) \tag{1.20}$$

Equation 1.20 reveals the relationship between axial particle velocity and axial strain as:

$$\dot{u} = \pm c\varepsilon \tag{1.21}$$

with the $\pm$ indicating a possible modification to the sign to comply with the datum being used. Given that the continuation of the wave through a transmitter bar, represented by the subscript *t*, is ideally terminated anechoically; there is no reflection wave. Thus, the transmitter bar velocity takes the same form as the outgoing wave velocity in the incident bar, shown by:

$$\dot{u}_2 = -c\varepsilon_t \tag{1.22}$$

where the strain of the transmitter bar can be measured using *Strain Gauge Pair 2* in *Figure 1.2* and another Wheatstone bridge circuit. The strain-rate of the specimen is:

$$\dot{\varepsilon}_s = \frac{(\dot{u}_1 - \dot{u}_2)}{l_s} \tag{1.23}$$

where l_s is the length of the specimen. Substituting *Equation 1.20* and *Equation 1.22* into *Equation 1.23* yields:

$$\dot{\varepsilon}_s = \frac{c}{l_s}(-\varepsilon_i + \varepsilon_r + \varepsilon_t) \tag{1.24}$$

Using the relationship $\varepsilon_t = \varepsilon_i + \varepsilon_r$ yields:

$$\dot{\varepsilon}_s = \frac{2c}{l_s}\varepsilon_r \tag{1.25}$$

And thus, the strain of the specimen, shown by *Equation 1.26*, is obtained by integrating *Equation 1.25*:

$$\varepsilon_s = \int_{t_0}^{t} \dot{\varepsilon}_s dt = \frac{2c}{l_s}\int_{t_0}^{t} \varepsilon_r dt \tag{1.26}$$

where t_0 is a time at which the reflection wave is first measurable and t represents the time at which the wave passes. To perform a stress analysis, it is assumed that the

specimen reaches a quasi-static equilibrium. At the interface of the test specimen (represented by subscript *s2*) and the transmitter bar, the force/stress relationships between the two faces are:

$$F_{s2} = F_t$$

$$A_s\sigma_{s2} = A_b\sigma_t = A_b(E\varepsilon_t) \tag{1.27}$$

where E is the Young's modulus of the transmitter bar. Because it is assumed the specimen reaches stress equilibrium ($\sigma_{s2} = \sigma_s$), the specimen stress is:

$$\sigma_s = \frac{A_b}{A_s}E\varepsilon_t \tag{1.28}$$

The interface of the specimen and transmitter bar is used for the stress analysis because if one were to equate the forces at the interface with the incident bar, one would have to sum the incident strain signal and reflection strain signal to write the force-balance equation. For soft materials, the incident and reflection strains are typically similar in magnitude but opposite sign; thus, this leaves the stress calculation vulnerable to error due to poor signal resolution following the summation.

2. Overview of the Velocity Gauge Instrumented Split-Hopkinson Pressure Bar

2.1 Introduction

The need for a velocity gauge instrumented SHPB arises from having to use low-impedance bars to test low-impendence test specimens, like those of interest. Acquiring accurate results from testing a low-impedance material using typical elastic bars made from steel or aluminum can be difficult, because so little of the incident wave is transmitted through the material due to the impedance mismatch of the bar and the specimen. If one were to use the conventional test setup in *Figure 1.2*, standard strain gauges would not be sensitive enough to accurately measure the low-level transmitted strain. One solution to the issue of a small transmission wave is to use polymeric bars to reduce the impedance mismatch and to allow more of the incident wave to be transmitted. However, viscoelastic effects like attenuation and dispersion must be considered with the use of such bars. If using a conventional SHPB setup with strain gauges at the bar bisections to capture the wave propagation, one would have to account for these effects to predict what waveforms are occurring at the test specimen interfaces. While there are manners in which to account for the change in wave shape as it propagates through a polymeric bar, the analytical process is more complex and does not always guarantee accurate results.

The use of wire velocity gauges offers non-perturbing means to simplify much of the test analyses needed for a viscoelastic SHPB test. Velocity gauges, when instrumented at the ends of the pressure bars, are able to measure axial velocity directly at the test specimen interfaces without the need to account for viscoelastic effects.

Although, when it comes to determining specimen stress, viscoelastic effects do play a role by affecting the wave speed. Wave speed is dependent on wave frequency in a viscoelastic bar, and attenuation further complicates the circumstances. At this point, viscoelastic wave modelling is seemingly unavoidable. However, Casem demonstrated that if one were to neglect viscoelastic effects and use a linear-elastic approximation while testing with polymeric bars and velocity gauges, the error in measurement was insignificant, which contrasts the error found when the same approximation was made using strain gauges in a conventional SHPB test setup [9,10]. In his works [9,10], Casem further elaborates on sources of this error when making a linear-elastic approximation with strain gauge measurements, but in a few words, a large error source is the projection of measured waves from the mid-bar strain gauge location to the test specimen location. In other words, the linear-elastic approximation is more appropriate when the point of interest (the test specimen) and the point of measurement are collocated. Since strain gauges on a SHPB cannot be placed near the test specimen because they have to measure wave trains independently, strain gauges, unlike velocity gauges, cannot be collocated with test specimens. In summary, no account for viscoelastic effects is necessary to perform an accurate specimen stress-strain analysis when using the velocity gauge SHPB setup like that described in detail in *Section 2.2*.

2.2 Velocity Gauge Instrumented SHPB Theory

2.2.1 *Velocity Gauges*

An electromagnetic velocity gauge, for the purpose of the SHPB tests to be conducted, can be made by diametrically inserting a small insulated wire through a

pressure bar as close to the test specimen interface as possible, as shown in *Figure 2.1*. The wire, measuring l_g in length, will generate an electric potential, E, proportional to an axial velocity, v, should it cross an orthogonal magnetic field, B. This relationship is dictated by Faraday's law of induction and is given by *Equation 2.1* [11]. Since it is desired to only measure the axial velocity within the bar, the lead wires (the portion of the wire not within the bar) that carry the electric potential to a data acquisition system (DAQ) must be oriented parallel to the magnetic field (orthogonal to gauge wire), as shown in *Figure 2.1*. This is in order to reduce unwanted disturbances in measurement as the wires move with the bar. Because the function of these gauges is reliant on the use of a magnetic field, it should be noted that these gauges are only suitable for non-conductive pressure bars.

$$E = Bvl_g \tag{2.1}$$

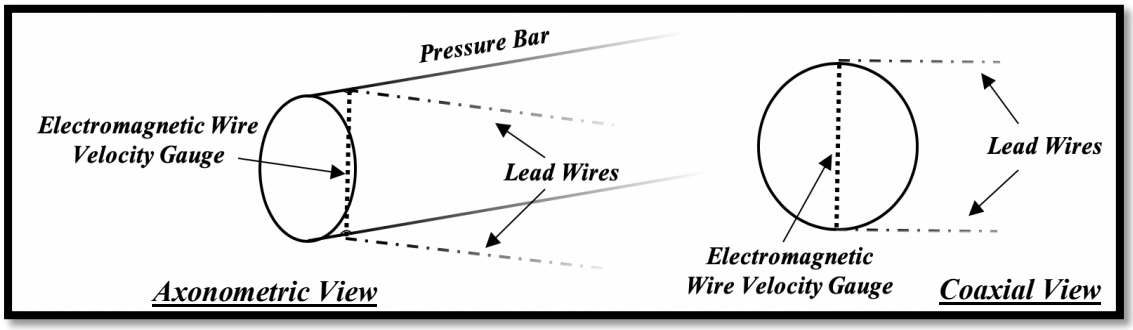

Figure 2.1: Electromagnetic velocity gauge in a pressure bar.

2.2.2 *Helmholtz Coils*

Helmholtz coils can be used to generate a uniform magnetic field in which the velocity gauges can operate. The coils consist of numerous loops of enameled magnet wire that will generate a magnetic field should a current flow through them. When two same-sized coils are spaced at a radius length apart from each other, they generate a

region of uniform magnetic field parallel to the coil axes and centered at the midway point between them. As seen in *Figure 2.2*, if the Helmholtz coils are positioned so that the pressure bars and the velocity gauges are located at this midway point, the gauges will have a proper field to measure the axial velocity of a wave propagating through the pressure bars.

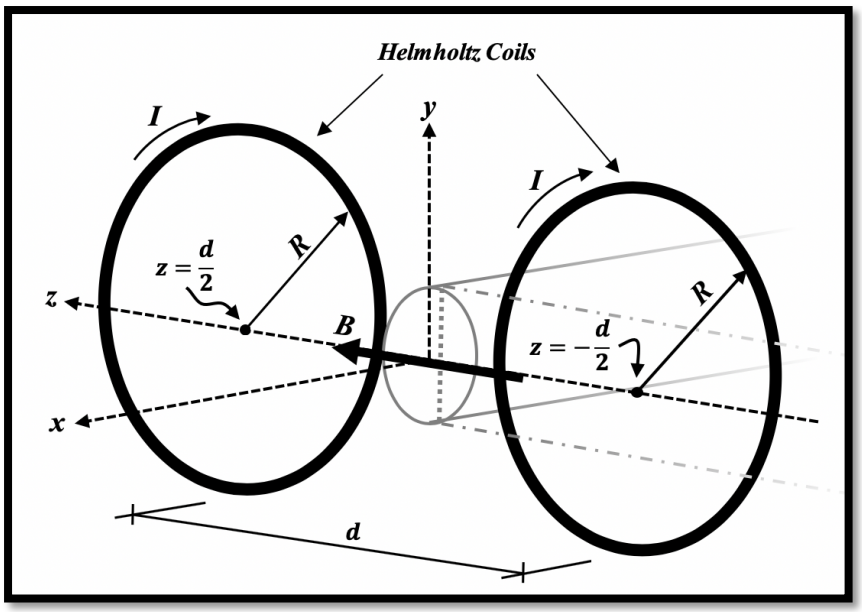

Figure 2.2: Helmholtz coil datum and configuration.

Consider the datum shown in *Figure 2.2*, where the origin is coaxially located midway between two d-spaced coils. A single coil of radius R, n number of wire loops, and a current flow I, that's center is located at $z = \pm d/2$ will generate a magnetic field on the z-axis in the positive z-direction represented by *Equation 2.2* [12]. It is assumed that all n number of wire loops are of the same radius and position.

$$B = \frac{\mu_0 n I R^2}{2\left[R^2 + \left(z \pm \frac{d}{2}\right)^2\right]^{3/2}} \tag{2.2}$$

Here, μ_0 is the permeability constant, $4\pi \times 10^{-7}\ \frac{T \cdot m}{A}$. One can calculate the z-directional magnetic field, along the z-axis, of two operating coils symmetrically

positioned about the xy-plane by applying the principle of superposition to *Equation 2.2* and a similar equation adjusted for a coil located at $z = \mp d/2$. This function is represented by *Equation 2.3*. Recall, to generate a uniform magnetic field region about the origin, two coils must be spaced at a radius length ($d = R$).

$$B = \frac{\mu_0 nIR^2}{2\left[R^2+\left(z\pm\frac{d}{2}\right)^2\right]^{3/2}} + \frac{\mu_0 nIR^2}{2\left[R^2+\left(z\mp\frac{d}{2}\right)^2\right]^{3/2}} \tag{2.3}$$

2.2.3 Stress-Strain Relations of the SHPB

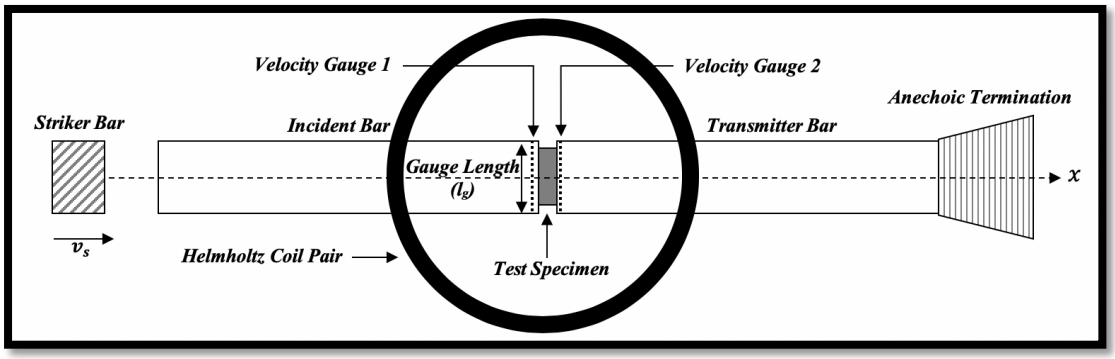

Figure 2.3: SHPB test setup instrumented with electromagnetic velocity gauges.

With the test setup shown in *Figure 2.3*, the striker bar, moving with velocity v_s, impacts the polymeric incident bar and produces a longitudinal wave that propagates through the incident bar with an axial velocity, v. In addition, with the Helmholtz coils spaced at a radius distance apart from each other, the coils generate a uniform magnetic field about the velocity gauges and a test specimen between the pressure bars. When the wave propagates through *Velocity Gauge 1*, an electric potential, E_1, is generated, and when the wave propagates through *Velocity Gauge 2*, an electric potential, E_2, is generated. These potentials can be converted to their respective velocities by rearranging *Equation 2.1* to give:

$$v_j = \frac{E_j}{G_j B l_g} \ , \ j = 1, 2 \tag{2.4}$$

where G_j is any gain applied to the electric potential within the DAQ. Because the velocity gauges are measuring the axial wave velocity directly at the test specimen interfaces, the specimen strain-rate can be calculated using:

$$\dot{\varepsilon}_s = \frac{(v_1 - v_2)}{l_s} \tag{2.5}$$

an equation of the same form as *Equation 1.23* for the linear-elastic conventional SHPB test setup in *Section 1.2.2*. Shown by *Equation 2.*6, the specimen strain is then found by integrating *Equation 2.5*.

$$\varepsilon_s = \int_{t_0}^{t} \dot{\varepsilon}_s dt \tag{2.6}$$

After substituting *Equation 1.21* into *Equation 1.28,* utilizing the equation for wave speed in the bar (See *Section 1.2.1*), and then reducing, the following is generated as the equation for specimen stress in terms of *Velocity Gauge 2*:

$$\sigma_s = \rho c_0 \frac{A_b}{A_s} v_2 \tag{2.7}$$

As mentioned in *Section 2.1*, wave speed is dependent on frequency in a viscoelastic pressure bar, but *Equation 2.7* is using an acceptable linear-elastic approximation under the condition that velocity gauges are being used at the specimen interfaces. Here, c_0 reflects the approximation and is called the static (zero-frequency) wave speed, which utilizes the static modulus, a value that remains constant at low frequencies much like in an elastic, non-dispersive case.

3. Frequency Domain Characterization Theory

3.1 Introduction

Upon capturing strain-rate, strain, and stress data using the SHPB and the relationships derived in *Chapter 2*, additional material characteristics can be determined in the frequency domain with the aid of a rheological model. The ability to extract both time domain stress-stain relationships and meaningful frequency information from a single high strain-rate dynamic test is an advantageous process that provides an abundance of information about the material. The first step in this process is the careful choice of a rheological model that displays realistic viscoelastic response characteristics. The Generalized Maxwell Model (GMM) or Maxwell-Wiechert Model is one of the simplest rheological models that encompasses all of these fundamental characteristics that will be underlined in *Section 3.2*. The key to joining this model with the SHPB test data is the application of the Boltzmann Superposition Principle. This principle, presented in *Section 3.3*, allows the parametric rheological model to act as the test material's relaxation modulus, and using a proper optimization algorithm, the model can be fitted to experimental data until it accurately represents the material during a certain test event. With the parameters of the model optimal to represent the material, the parameters can be carried over to the model's frequency domain relationships, where storage modulus, an elastic quantity, and loss factor, a dissipative quantity, are obtained. These quantities provide insight to whether the material, at certain bandwidths, responds satisfactory according to one's requirements.

3.2 Generalized Maxwell Model

A viscoelastic test specimen can be realistically represented by the Generalized Maxwell Model. The model is comprised of a spring in parallel with *n* number of elements containing a spring and damper in series. The springs and dampers in the model introduce known stiffness and damping relationships, with which a constitutive differential equation can be derived. The model's unaccompanied parallel spring is to ensure that the model maintains elasticity responding to excitation frequencies near zero. Note that some fundamental characteristics of viscoelastic material are an increase in elasticity with an increase in excitation frequency and lower dissipation at low and high excitation frequencies. The GMM encompasses these qualities. The application of the GMM in the context of the SHPB can be seen in work done by Baz [8] and Akl and Baz [13]. Baz's text utilizes the Boltzmann Superposition Principle to find the unknown model parameters using data from the entire SHPB test event, whereas the publication with Akl examines a material that responds in such a way that only the relaxation portion of the test event is required to be observed. The application of the GMM via the Boltzmann Superposition Principle is a more applicable method and therefore will be used for this research.

3.2.1 *Constitutive Equation*

To characterize the GMM, the constitutive equation must first be determined by applying a stress load, σ, to the model, as shown in the rheological diagram of the GMM in *Figure 3.1*. To begin, analyzing the *k*th element of the spring-damper series due to a stress σ_k yields the following relationships:

$$\sigma_k = \sigma_E = \sigma_\eta \tag{3.1}$$

$$\varepsilon_k = \varepsilon_E + \varepsilon_\eta \tag{3.2}$$

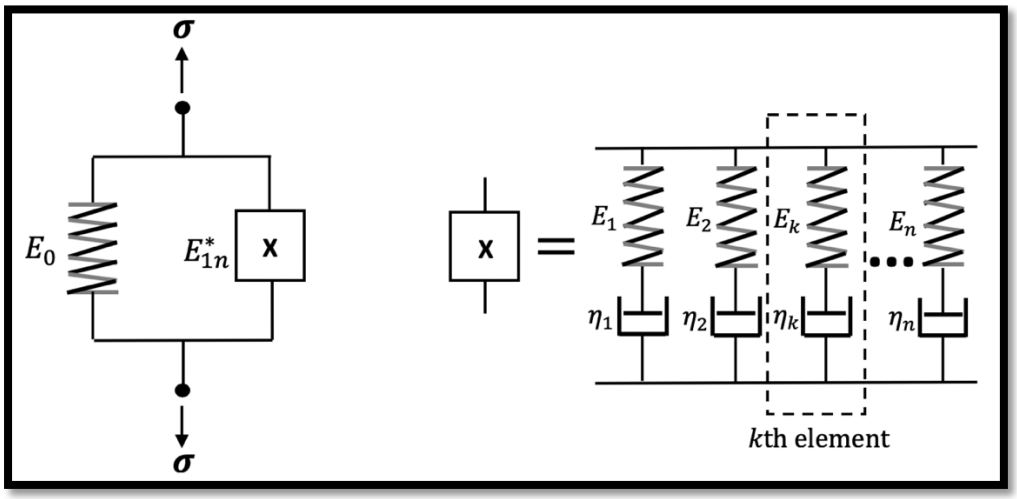

Figure 3.1: Generalized Maxwell Model rheological diagram.

Where σ_E and σ_η are the stresses on the spring and damper in the *k*th element respectively, and ε_E and ε_η are the strains across the spring and damper in the *k*th element respectively. The relationships between stress and strain for the spring and damper are:

$$\sigma_E = E_k \varepsilon_E \tag{3.3}$$

$$\sigma_\eta = \eta_k \dot{\varepsilon}_\eta \tag{3.4}$$

Here E_k is the element modulus and η_k is the element viscosity. Differentiating *Equation 3.1, Equation 3.2* and *Equation 3.3* with respect to time gives:

$$\dot{\sigma}_k = \dot{\sigma}_E = \dot{\sigma}_\eta \tag{3.5}$$

$$\dot{\varepsilon}_k = \dot{\varepsilon}_E + \dot{\varepsilon}_\eta \tag{3.6}$$

$$\dot{\sigma}_E = E_k \dot{\varepsilon}_E \tag{3.7}$$

Substituting the strain-rate relationships from *Equation 3.4* and *Equation 3.7* into *Equation 3.6* yields:

$$\dot{\varepsilon}_k = \frac{\dot{\sigma}_E}{E_k} + \frac{\sigma_\eta}{\eta_k} \tag{3.8}$$

Applying the relationships in *Equation 3.1* and *Equation 3.5* to *Equation 3.8* results in the following:

$$\dot{\varepsilon}_k = \frac{\dot{\sigma}_k}{E_k} + \frac{\sigma_k}{\eta_k} \tag{3.9}$$

By multiplying *Equation 3.9* through by η_k and letting $\rho_k = {\eta_k}/{E_k}$, the constitutive equation for the *k*th spring-damper element is found to be:

$$\eta_k \dot{\varepsilon}_k = \rho_k \dot{\sigma}_k + \sigma_k \tag{3.10}$$

3.2.2 *Relaxation Modulus*

The time domain relaxation modulus of the *k*th element can be determined from the constitutive equation by setting conditions that represent a stress relaxation test (i.e. $\dot{\varepsilon}_k = 0$ and $\varepsilon_k(t) = \varepsilon_0$). These conditions when applied to *Equation 3.10* give:

$$\rho_k \dot{\sigma}_k + \sigma_k = 0 \tag{3.11}$$

The solution to this ordinary differential equation is:

$$\sigma_k(t) = \sigma_0 e^{-t/\rho_k} \tag{3.12}$$

where σ_0 is a constant and represents the initial stress. Using the relationship between the initial stress and the initial strain, $\sigma_0 = E_k \varepsilon_0$, alters *Equation 3.12* to:

$$\sigma_k(t) = E_k \varepsilon_0 e^{-t/\rho_k} \tag{3.13}$$

Using *Equation 3.13*, the function for relaxation modulus of the *k*th element can be represented by:

$$E_k^r(t) = \frac{\sigma_k}{\varepsilon_0} = E_k e^{-t/\rho_k} \tag{3.14}$$

The *n*-length parallel combination of the spring-damper elements gives the relaxation modulus as:

$$E_{1n}^{r}(t) = \sum_{k=1}^{n} E_k e^{-t/\rho_k} \tag{3.15}$$

Combining the relaxation modulus of *n* spring-damper elements with the constant relaxation modulus of the single parallel spring (E_0) yields the relaxation modulus equation of the GMM, *Equation 3.16*.

$$E^{r}(t) = E_0 + E_{1n}^{r} = E_0 + \sum_{k=1}^{n} E_k e^{-t/\rho_k} \tag{3.16}$$

Note that at $t = 0$, $E^r(t) = E_0 + \sum_{k=1}^{n} E_k$, which is also equal to the elastic modulus for the material, and at $t = \infty$, $E^r(t) = E_0$, which is known as the equilibrium modulus.

3.2.3 *Complex Modulus*

To solve for the complex modulus of the GMM, the *k*th element is subjected to sinusoidal excitation. The stress and strain of the *k*th element can be represented by *Equation 3.17* and *Equation 3.18* respectively.

$$\sigma_k = \sigma_0 e^{i\omega t} \tag{3.17}$$

$$\varepsilon_k = \varepsilon_0 e^{i\omega t} \tag{3.18}$$

Here σ_0 and ε_0 represent amplitudes of their respective signals. Applying *Equation 3.17* and *Equation 3.18* to *Equation 3.10* and differentiating when necessary yields:

$$(\rho_k i\omega + 1)\sigma_0 = \eta_k i\omega \varepsilon_0 \tag{3.19}$$

The complex modulus of the *k*th element is thus:

$$E_k^* = \frac{\sigma_0}{\varepsilon_0} = \frac{\eta_k i\omega}{\rho_k i\omega + 1} = E_k \frac{\rho_k i\omega}{\rho_k i\omega + 1} \tag{3.20}$$

For an *n*-length parallel combination of the spring-damper elements, the complex modulus is:

$$E_{1n}^{*} = \sum_{k=1}^{n} E_k \frac{\rho_k i\omega}{\rho_k i\omega + 1} \tag{3.21}$$

Combining the moduli of the single spring and the spring-damper elements in parallel yields the complex modulus of the GMM, *Equation 3.22*.

$$E^{*} = E_0 + E_{1n}^{*} = E_0 + \sum_{k=1}^{n} E_k \frac{\rho_k i\omega}{\rho_k i\omega + 1} \tag{3.22}$$

After separating *Equation 3.22* into its real and imaginary parts, the storage modulus, E', and the loss factor, η, can be generated from the following relationship:

$$E^{*} = E^{'}[1 + i\eta] \tag{3.23}$$

3.3 Boltzmann Superposition Principle

The Boltzmann Superposition Principle (BSP), as explained in detail by Brinson and Brinson [14], is a principle that states that the current stress state of a viscoelastic material is dictated by the cumulative effect of the accompanying strain history. The relationship that defines the manner in which the strain history affects the current stress state is represented by *Equation 3.24*: a convolution integral of the relaxation modulus and strain-rate.

$$\sigma(t) = \int_0^t E^r(t-\tau) \frac{\partial \varepsilon(\tau)}{\partial \tau} d\tau \tag{3.24}$$

If the relaxation modulus of the material is modeled by the GMM, then substituting *Equation 3.16* into *Equation 3.24* reveals how the test specimen stress can be described using the GMM:

$$\sigma_{GMM}(t) = \int_0^t \left[E_0 + \sum_{k=1}^{n} E_k e^{-(t-\tau)/\rho_k}\right] \frac{\partial \varepsilon_s(\tau)}{\partial \tau} d\tau \tag{3.25}$$

Now, upon recording stress-strain data from a SHPB test, the unknown parameters E_0, E_k, and ρ_k for $k = 1, \dots, n$ can be determined by running an optimization algorithm that fits *Equation 3.25* to the experimental stress data. As described by Baz [8], the optimization problem, is:

$$\left\langle \begin{array}{c} \text{Solve for } E_0, E_k, \text{and } \rho_k \text{ for } k = 1, \dots, n \\ \text{to minimize } F = \sum_{t=0}^{t=T} [\sigma_s(t) - \sigma_{GMM}(t)]^2 \\ \text{such that } E_0 > 0, E_k > 0, \text{and } \rho_k > 0 \text{ for } k = 1, \dots, n \end{array} \right\rangle$$

where $t = 0$ marks the time at the beginning of the stress signal (prior to $t = 0$ there is only zero-valued stress and strain), T marks the end time of the test event, and $\sigma_s(t)$ is the experimental stress data. Because discrete data points from SHPB tests are being handled and not continuous functions, MATLAB's conv( ) function can be used to convolve the GMM relaxation modulus and the strain-rate data, and the optimization can be carried out using MATLAB's fmincon( ) function. The script in *Appendix A* provides additional detail on how to perform this optimization procedure.

Once the GMM parameters in *Equation 3.25* have been optimized to fit the model to the experimental stress data, the parameters can then be substituted in *Equation 3.22* to extract the storage modulus, E', and loss factor, η, for the specimen during that particular SHPB test. *Figure 3.2* shows a flow chart to clarify the process and the equations that will be used to determine frequency domain characteristics from the SHPB tests.

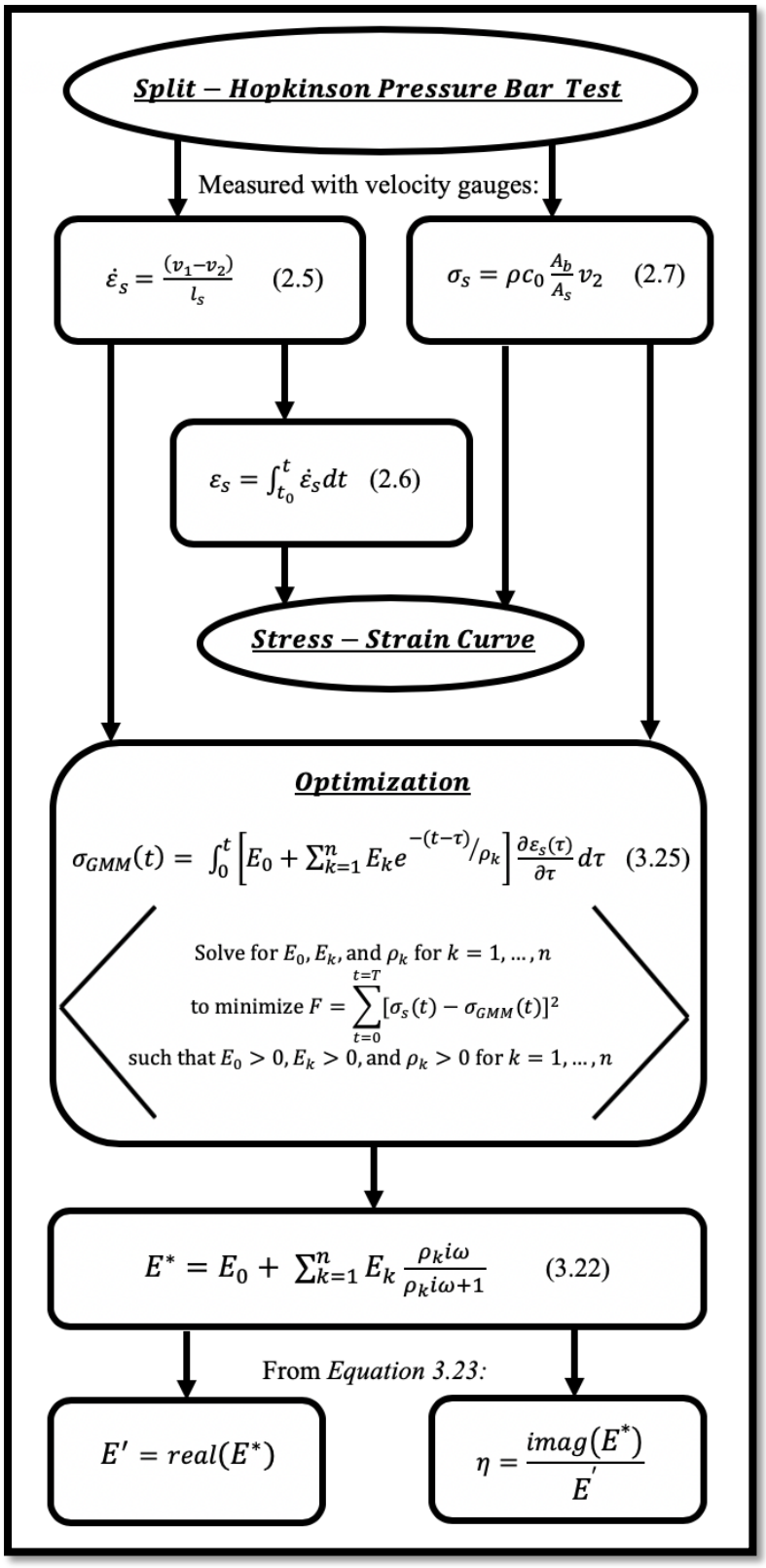

Figure 3.2: Flow chart displaying the procedure for extracting frequency domain characteristics from SHPB test.

4. Test Preparation

4.1 Introduction

The following chapter reviews the design process and the construction of main equipment within the experimental setup. Furthermore, this chapter covers procedures that were carried out to verify the proper function of each working element in the setup. This includes calibrating the constructed Helmholtz coils to produce a uniform magnetic field, analyzing the effects that an amplifier circuit has on measured signals, and calibrating the velocity gauges to determine the relationship between electric potential and axial velocity. Upon proving the proper function of all equipment, including a data acquisition system (DAQ), which is to be considered the combination of an amplifier circuit and an oscilloscope, then the equipment setup is deemed ready for material testing.

4.2 Equipment and Data Acquisition System

4.2.1 *Split-Hopkinson Pressure Bar*

The SHPB components that remain unchanged for all of the tests conducted consist of polycarbonate pressure bars measuring 1219.2 mm in length and 15.875 mm in diameter. The polycarbonate density is 1200 kg/m^3 and the static modulus was taken to be 2.2 GPa, resulting in a static wave speed of c_0 = 1354 m/s. These pressure bars are mounted 101.6 mm above an aluminum beam base while using low-friction dry bearings to allow linear motion of the bars with minimal friction. Striker bars will be propelled by a nitrogen gas gun that has pressure regulation components, a digital pressure read-out, and a Whitey pneumatic actuator that acts as a trigger mechanism. Using a Phantom

high-speed camera, a small study was conducted to find the relationship between gas gun firing pressure, in psi, to striker bar velocity, in m/s. The two strikers used for research were fired at increasing gun pressures and recorded with the high-speed camera. The strikers are both polycarbonate with 15.875 mm diameters, but the lengths differ with values of 152.4 mm and 304.8 mm. Upon video capture, digital measuring software was utilized to obtain the striker velocities. *Figure 4.1* shows the experimental results and curve fit lines. The curve fit equations were used to approximate striker velocities for tests with firing pressures greater than 10 psi and different than those not performed in the study.

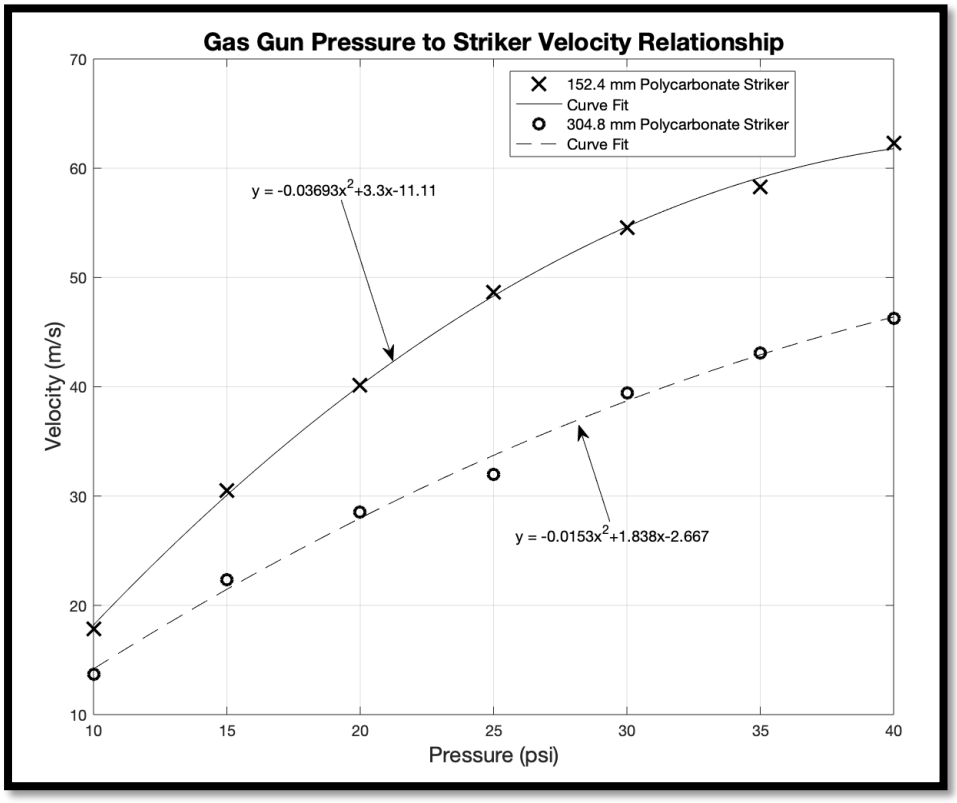

Figure 4.1: Gas gun striker velocity as a function of firing pressure.

Effective anechoic termination materials are a luxury; therefore, solid polyurethane rubber was used instead as a damping material to receive the impact of the

transmitter bar. As long as data from the first passing of the propagating wave can be analyzed independently and the measurements thereafter can be ignored, the use of anechoic termination materials is unnecessary. *Figure 4.2* is a detailed diagram of the test equipment in its entirety. The striker bar and gas pressure regulation components are not shown. Some equipment will be explained further in detail throughout the chapter. *Figure 4.3* is photographs of the SHPB and coils. Not all of the components from the diagram can be seen in the photographs.

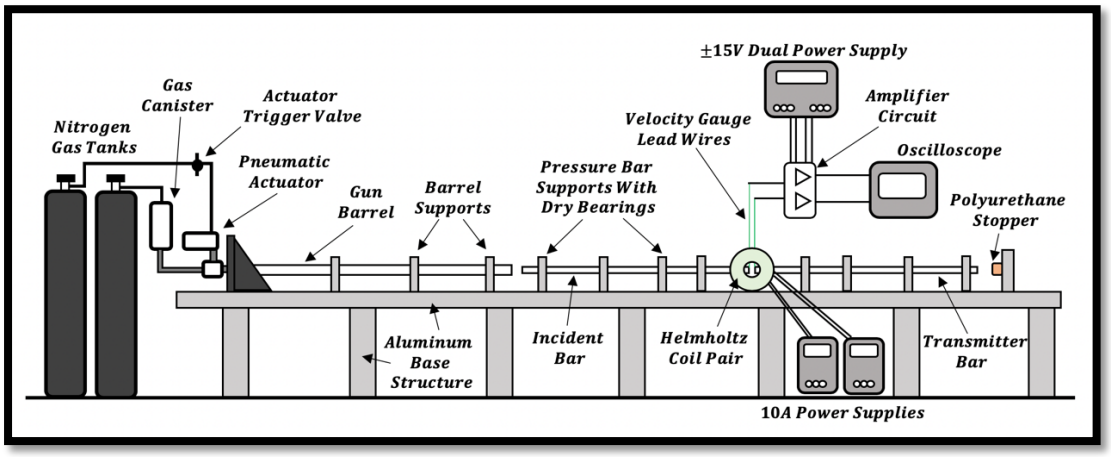

Figure 4.2: Diagram of equipment to be used for testing.

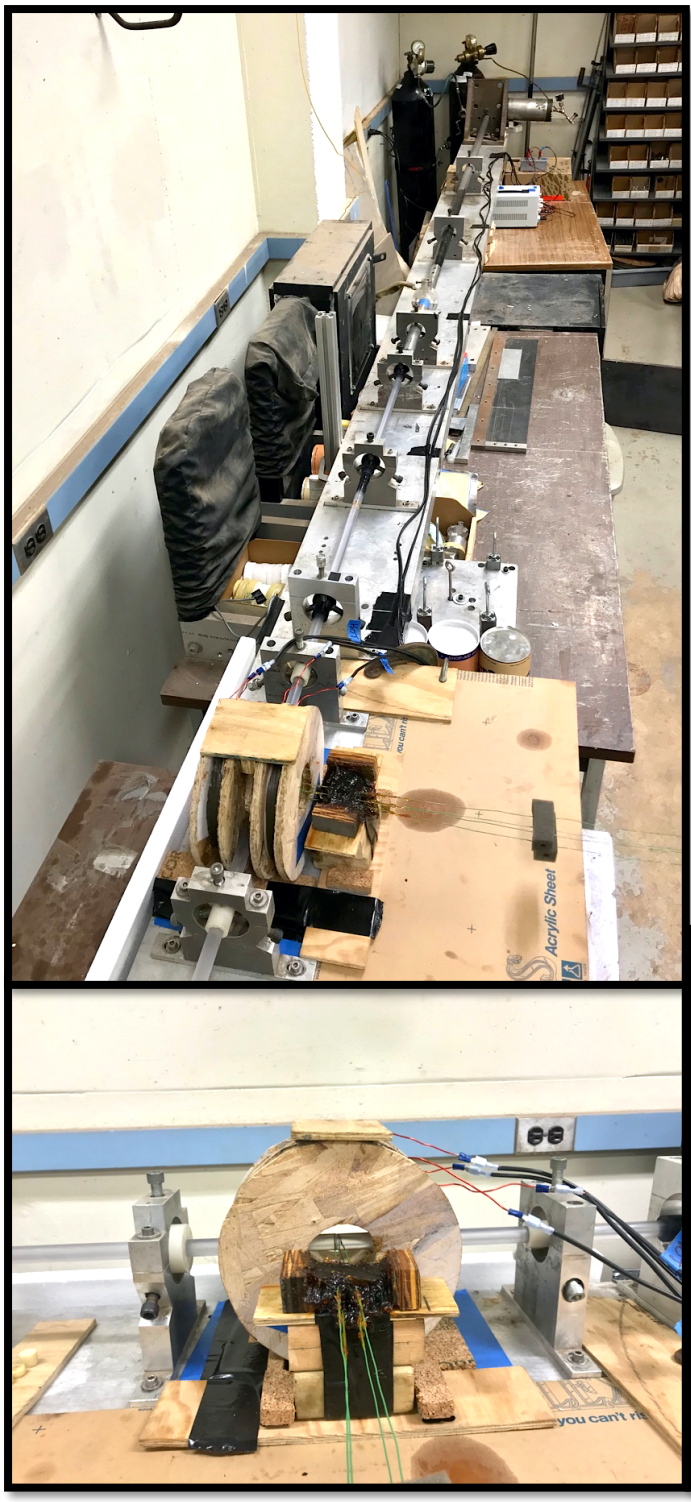

Measurement/ Property	Magnitude
Striker Static Modulus	2.2 GPa
Striker Density	1200 kg/m^3
Striker Diameter	15.875 mm
Striker Length	152.4 mm/304.8 mm
Pressure Bar Static Modulus	2.2 GPa
Pressure Bar Density	1200 kg/m^3
Pressure Bar Diameter	15.875 mm
Pressure Bar Length	1219.2 mm

Figure 4.3: Photos of assembled test equipment and table of bar dimensions/properties.

4.2.2 *Helmholtz Coils*

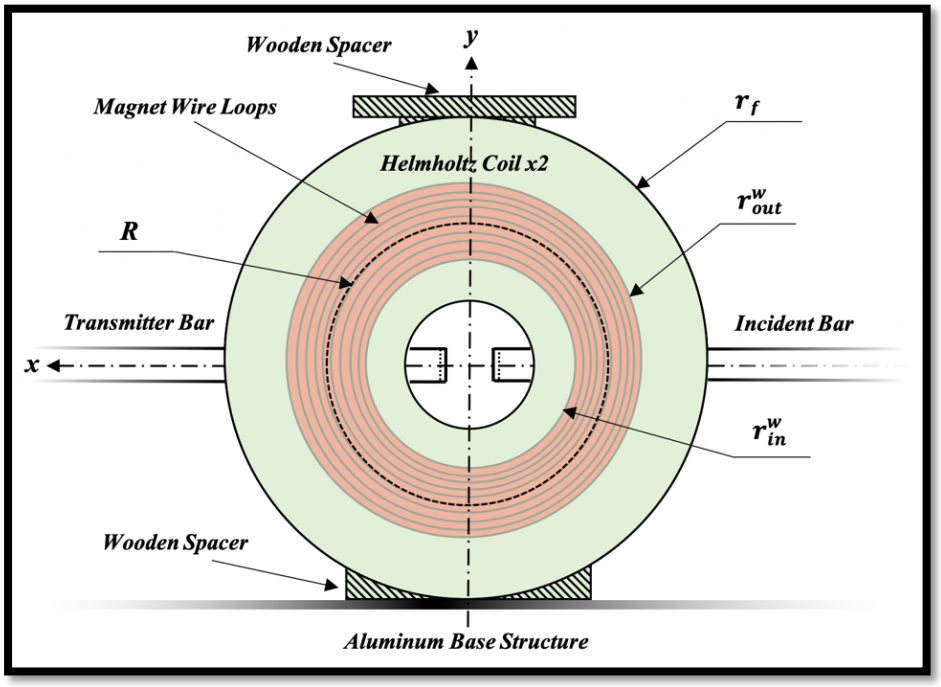

Figure 4.4: Diagram of constructed Helmholtz coils used for testing – coaxial to coils view.

The Helmholtz coils constructed for the velocity gauge instrumented SHPB experiments are represented by the diagrams in *Figure 4.4* and *Figure 4.5*. The measurements to accompany *Figures 4.4* and *4.5* are listed in *Table 4.1*. The 101.6 mm flange radius was chosen so that the pressure bars, located 101.6 mm above the aluminum beam base structure supporting the SHPB, would be parallel with the coils' midplane. The coils are of wooden construction and contain 300 loops of 16 AWG (American Wire Gauge) enameled magnet wire. The 16 AWG wire was chosen to appropriately accommodate the 10 amperes that were supplied to each coil by two 30V, 10A DC switch-mode power supplies.

Symbol	Measurement Name	Magnitude
r_f	Coil flange radius	101.6 mm
r_{out}^{w}	Outermost wire loop radius	79.375 mm
r_{in}^{w}	Innermost wire loop radius	50.8 mm
R	Equivalent wire loop radius	65.1 mm
t_f	Coil flange thickness	9.525 mm
t_s	Coil spool thickness	19.05 mm
d	Coil separation distance	65.1 mm

Table 4.1: Key dimensions of the constructed Helmholtz coils.

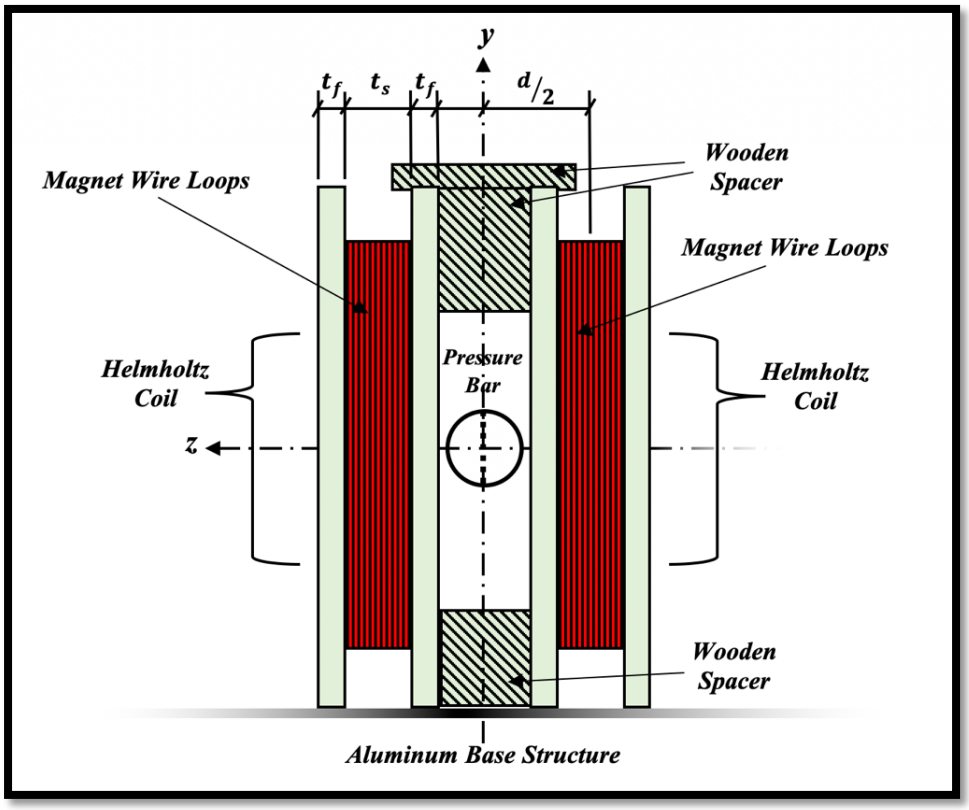

Figure 4.5: Diagram of constructed Helmholtz coils used for testing – coaxial to pressure bar view.

As stated, the equations for calculating magnetic field in *Section 2.2.2* assume that all of the wire loops are of the same radius; however, as anticipated, when constructing the coils, the radius of the magnet wire loops increased as more loops were added. Thus, to approximately calculate the magnetic field of the constructed coils, the average radius

of the coil loops was taken to be the equivalent wire loop radius (R) for use in the equations in *Section 2.2.2*. Measuring from the middle of the coil spool thickness (t_s), the two Helmholtz coils were spaced at an equivalent wire loop radius ($d = R$) length apart to establish a uniform magnetic field region. Furthermore, appropriately sized wooden spacers were needed to be placed between the coils so that when power was supplied to them, they would not move due to the magnetic attraction towards each other. Using *Equation 2.2* and *2.3* and R, the plot in *Figure 4.6* was generated to display the anticipated magnetic field coaxial to the coils as a function of position. The datum in *Figure 2.2* was maintained, and the effect of the position change due to the distribution of the wire looping along the coil spool thickness was not accounted for. *Figure 4.6* shows that each coil, operated individually with 10 A, is expected to generate 289.6 Gauss (G) at its center and 414.4 G at the midpoint between the coils when both coils are operating. Note that the SI unit for magnetic field strength is the Tesla (T) and 10,000 G = 1 T.

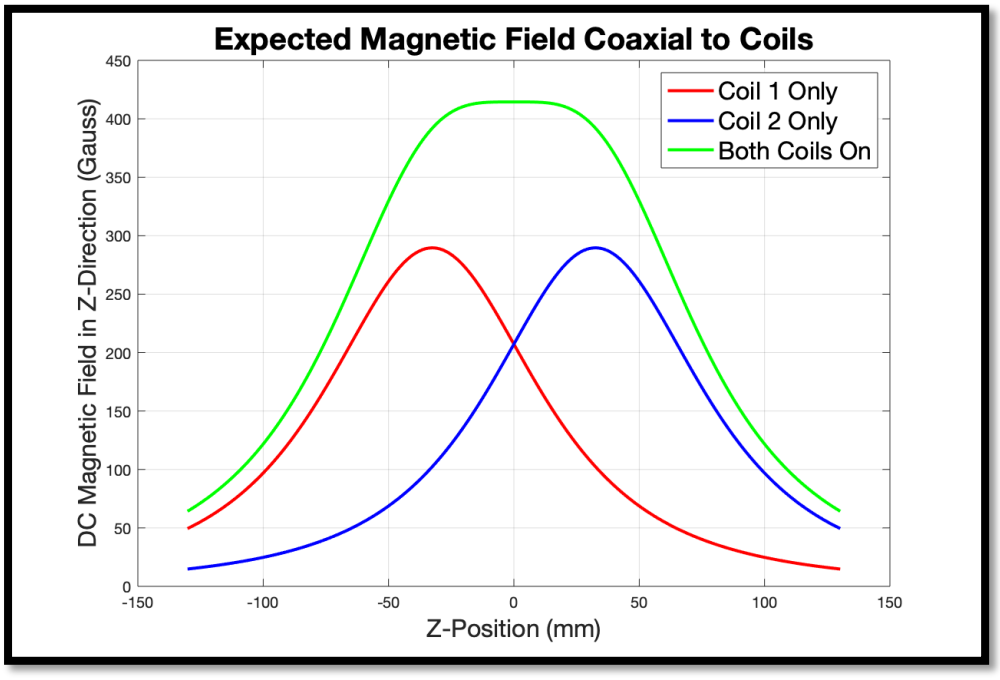

Figure 4.6: Expected magnetic field coaxial to coils.

It was deemed necessary that the powered Helmholtz coils be calibrated, due to nonuniformities in the wire looping. Using an AlphaLab DC Gaussmeter (Model GM1-ST), the magnetic field of each individual coil was measured at its center. One coil, at 10 A, measured 290 G and was deemed already calibrated because of the correspondence with the expected value. The second coil needed a supply of only 9.65 A to achieve a center magnetic field strength of 290 G. With the center of the coils calibrated, it is expected that the magnetic field along the coil axis (z-axis) is now symmetric about the pressure bar axis (x-axis). At the midpoint between the coils, the Gaussmeter measured 421 G, which contrasts the 414.4 G expected value. This difference is most likely due to the wire loop distribution along the coil spool thickness. Hereafter, the velocity gauges are expected to be operating in a magnetic field of 421 G.

4.2.3 *Oscilloscope*

The oscilloscope used throughout experimentation is a LeCroy 9354AM oscilloscope with a bandwidth of 500 MHz. For all of the tests logged throughout experimentation, the sampling rate used for recording was 25 MS/second. Upon capture, data was imported to MATLAB, where it would be processed by a script pertaining to the specific type of experiment.

4.2.4 *Amplifiers*

In order to properly capture the small electric potentials (voltages) generated by the velocity gauges during testing, a two-channel amplifier circuit, represented by the diagram in *Figure 4.7*, was assembled to amplify measurements. The circuit utilizes two

Texas Instruments OPA551PA operational amplifiers (op-amps), two TT Electronics 7286-10K-L.1 potentiometers, and two nominally 100 Ω carbon-film resistors (actual resistor values are shown in *Figure 4.7*). The op-amps are powered by a $\pm$15 V dual supply generated by a Protek 3015B Dual DC Power Supply. The circuit's inputs E_1^{in} and E_2^{in} are directly connected to the lead wires of the velocity gauges for measuring v_1 and v_2 respectively and are amplified by gains, G_1 and G_2, governed by *Equation 4.1* and *Equation 4.2* respectively. The voltage outputs, represented by *Equation 4.3*, are sent via Bayonet Neill-Concelman (BNC) cables to the oscilloscope.

$$G_1 = 1 + \frac{R_2}{R_1} \tag{4.1}$$

$$G_2 = 1 + \frac{R_4}{R_3} \tag{4.2}$$

$$E_j^{out} = G_j E_j^{in}\ ,\ j = 1, 2 \tag{4.3}$$

The range of the potentiometers being used should allow for all gains up to about 101; however, one limitation discovered is that the op-amps did not appear to be stable at unity gain with this configuration. It was also found that to minimize noise within the DAQ, it was paramount to use well-insulated, well-grounded low-voltage cables for any wiring other than the velocity gauge wires, which are limited to noise-reducing luxuries due to their size constraint.

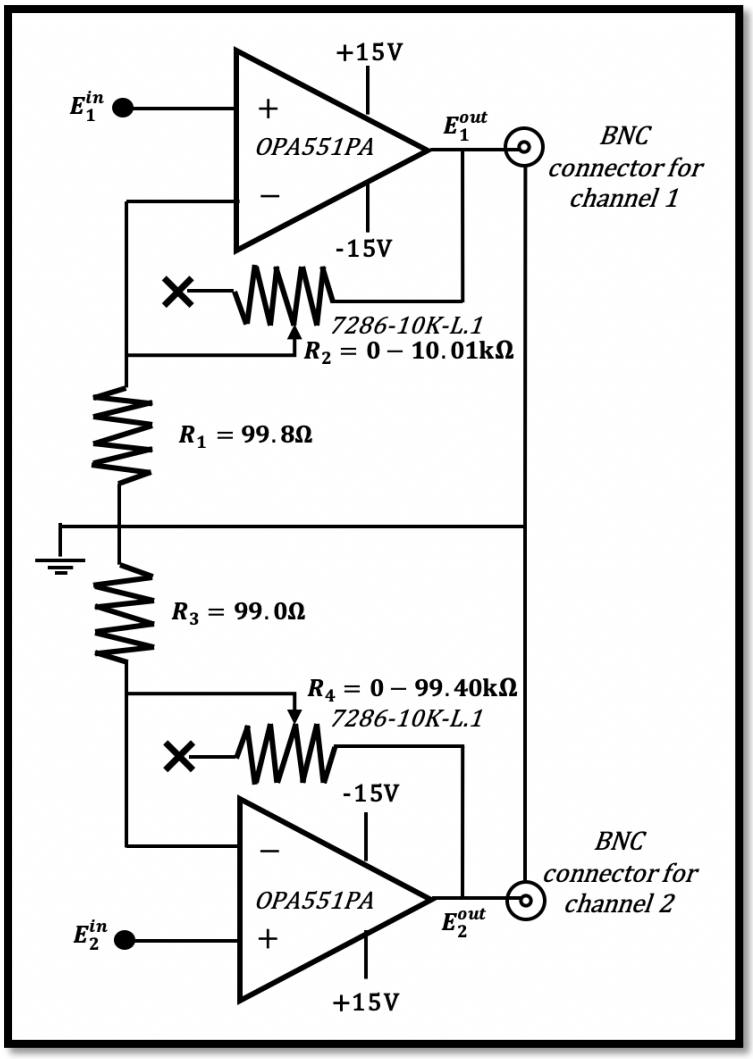

Figure 4.7: Circuit diagram of the two-channel amplifier.

A property of op-amps is that as the gain increases, the frequency response decreases. This is important to note, so that the extent of capturable spectral information can be determined. For the OPA551A op-amps used, at unity gain, their frequency response is 3 MHz. Tracing back from the unity gain value at a slope of -20 dB/decade generates the line that represents the gain and frequency response relationship, as shown in *Figure 4.8*. With a mutual max circuit gain of 101.3 for the channels, the frequency response of the op-amps used is, at minimum, around 29.6 kHz.

A small study was conducted to determine the effect of the amplifier gains, and thus the frequency response, on the quality of the velocity gauge signals. This is to verify that no significant information is lost by utilizing the full range of amplifier gains. First, the potentiometers were adjusted so that the amplifier circuit resulted in mutual channel gains of 101.3, 50, and then 25. Following these adjustments, the pressure bars were placed directly against each other, and the incident bar was impacted with the 304.8 mm polycarbonate striker at a gas gun pressure of 15 psi. The results in *Figure 4.9* reveal only miniscule changes in the wave measured by the velocity gauges, permitting the use of the entire range of amplifications.

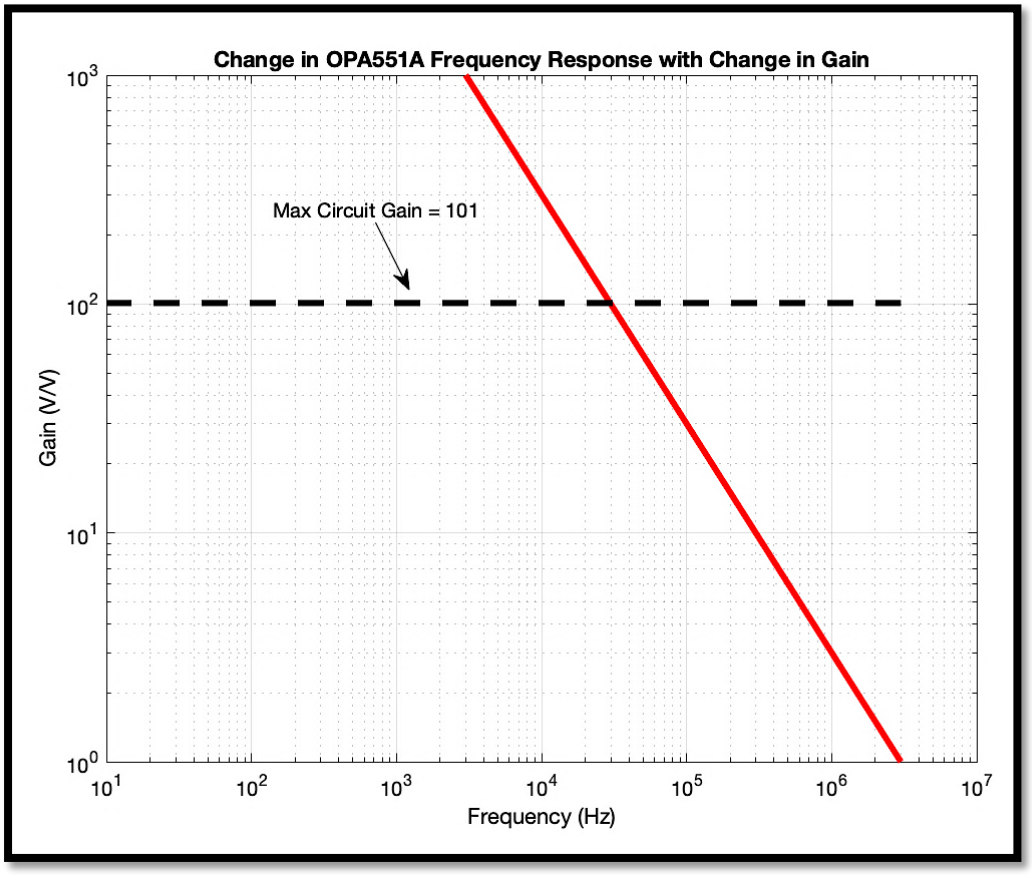

Figure 4.8: Frequency response of the OPA551A operational amplifier.

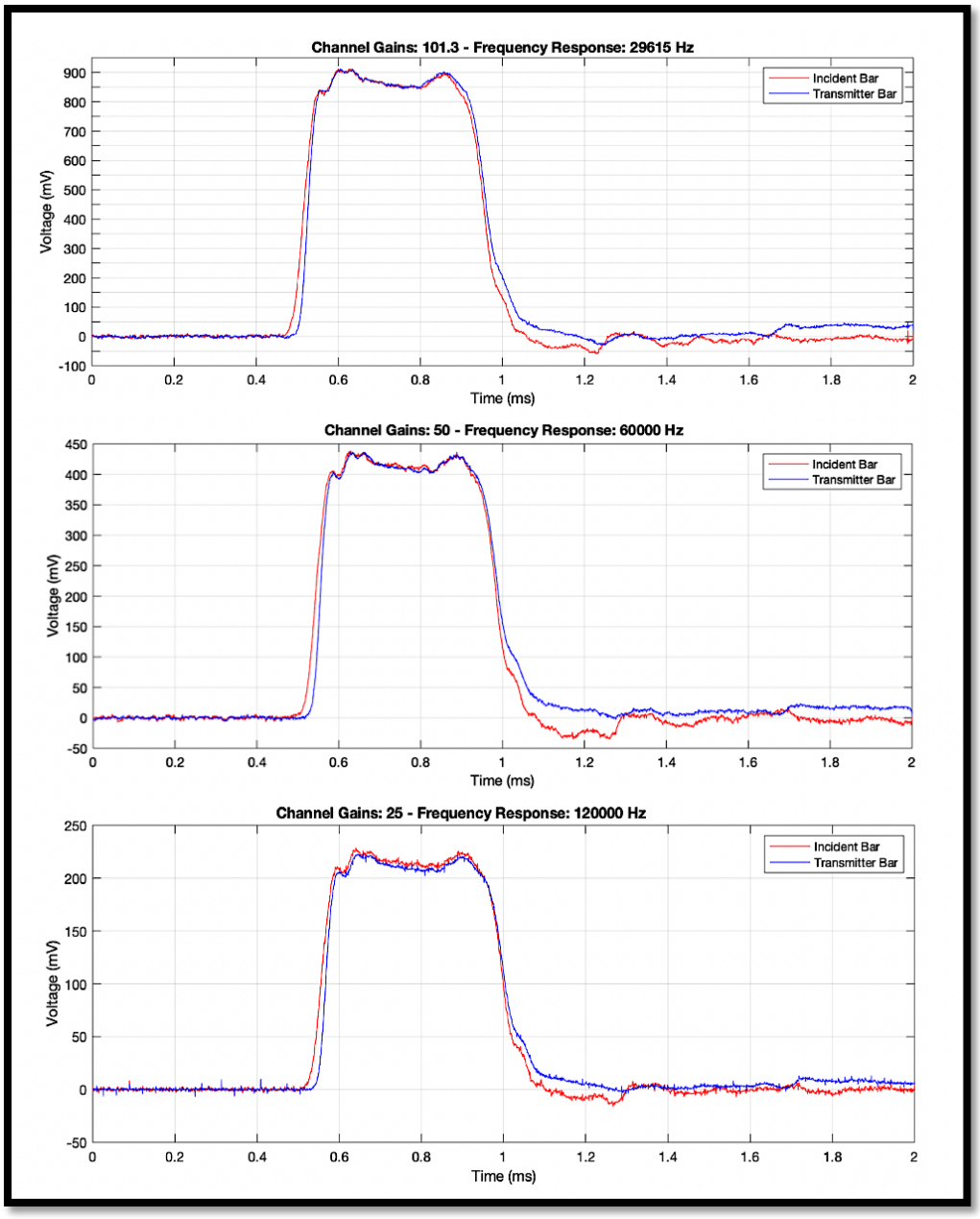

Figure 4.9: The effect of amplifier gains on the quality of velocity gauge signals.

4.2.5 *Velocity Gauges*

The velocity gauges instrumented in the pressure bars are 30 AWG Teflon insulated wires, measuring 0.80 mm in total diameter. Each gauge was diametrically inserted through a 1 mm hole, filled with glue, that is 2 mm from the pressure bar end that contacts test specimens. Due to their small size, the gauges will not disrupt passing

waves, and due to their location, the gauges will, in essence, measure at the test specimen interfaces. Furthermore, to reduce noise generated by the lead wires within the magnetic field, the lead wires were passed through a mass of grease. This is to limit wire oscillations but to allow for forward motion as the gauges move during testing.

Although the length of the wire gauge, the magnetic field, and amplifier gains can be measured to resolve the conversion from electric potential to velocity, variations of these conversion values are possible due to anomalies. One such anomaly could be the influence of gauge lead wire within the magnetic field on measured voltage. Thus, a method to calibrate the gauges was determined to be necessary, and Casem [9] presented a known displacement calibration technique to achieve this. For the following calibration technique, one gauge is truly calibrated, but it is assumed that any anomaly present is affecting both gauges equally. This assumption is reinforced by the symmetry within the test setup; however, a method to calibrate both wires independently would surely be preferred. The calibration constant (μ), or the conversion factor for gauge voltage to velocity, is taken to be the same for each gauge, and μ is revealed when *Equation 2.4* is rearranged to a form shown by *Equation 4.4*. *Equation 4.4* alludes to how a measured μ will contain the combined contributions of G, B, and l_g.

$$\frac{v}{E} = \frac{1}{GBl_g} = \mu \tag{4.4}$$

For the known displacement calibration test, no test specimen is used, and the incident and transmitter bars are spaced at a known displacement, δ, as shown in *Figure 4.10*. Once the Helmholtz coils are operating, the incident bar is then impacted with a striker bar. The voltage generated from the time of non-zero measurement (t_0) of the incident bar velocity gauge to the time of bar impact (t_i) measured by the transmitter

bar velocity gauge can be numerically integrated using MATLAB. The derivation of *Equation 4.6* from *Equation 4.4* shows how μ can be determined from a measured voltage signal.

$$v_1 = \mu E_1$$

$$\int_{t_0}^{t_i} v_1 dt = \mu \int_{t_0}^{t_i} E_1 dt$$

$$\text{with} \quad \delta = \int_{t_0}^{t_i} v_1 dt \tag{4.5}$$

$$\mu = \frac{\delta}{\int_{t_0}^{t_i} E_1 dt} \tag{4.6}$$

Note here that the subscript *1* reflects using the incident bar velocity gauge, and *Equation 4.5* shows how the known displacement, δ, is the time-integral of the incident bar velocity during the test event.

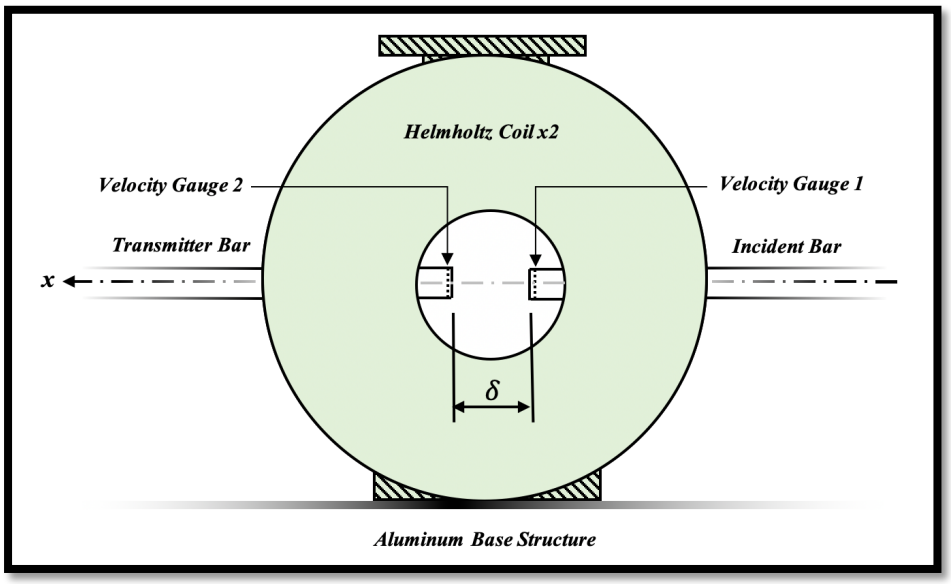

Figure 4.10: Known displacement calibration test setup.

The calibration tests shown in *Table 4.2* were conducted at various gas gun firing pressures and using the 304.8 mm polycarbonate striker. Also, the known displacement was 5 mm and both amplifier channels were set to a high gain of 101.3. An example of

the voltage signals captured by the velocity gauges is shown in *Figure 4.11*. Once a time of impact is determined by identifying a non-zero transmitter bar gauge voltage, the signals are then numerically integrated, as shown in *Figure 4.12*. The displacement measured by the incident bar gauge at the time of impact, in units $V \cdot s$, is the value that is substituted in *Equation 4.6* for that particular test.

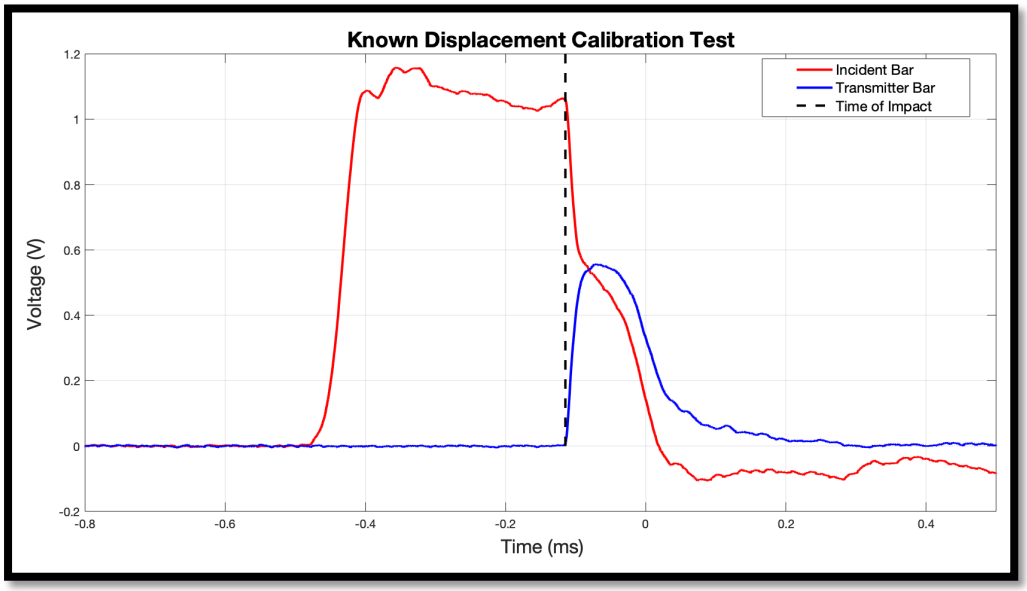

Figure 4.11: A known displacement calibration test voltage plot.

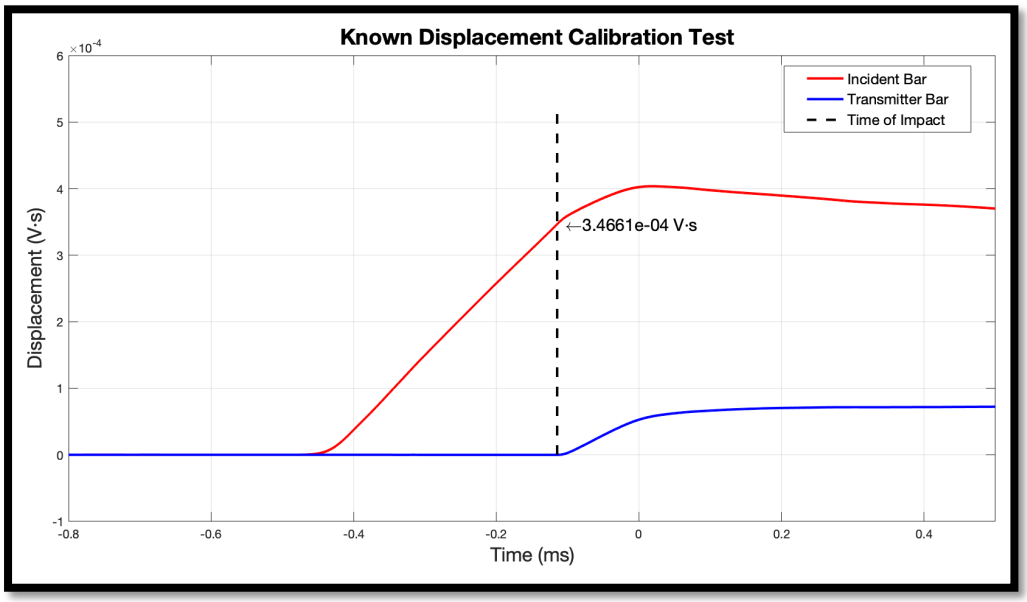

Figure 4.12: A known displacement calibration test integrated-voltage plot.

Calibration Constant Calculation				
Known Displacement of 5mm				
Test #	Known Displacement (mm) δ	Gas Gun Pressure (psi)	Integrated Voltage (volt·s)	Cal. Constant (m/s/V) μ
1	5.00	10.0	3.6002E-04	13.888
2	5.00	10.0	3.6266E-04	13.787
3	5.00	10.0	3.4661E-04	14.425
4	5.00	10.0	3.4588E-04	14.456
5	5.00	15.0	3.5874E-04	13.938
6	5.00	15.0	3.6143E-04	13.834
7	5.00	15.0	3.5599E-04	14.045
8	5.00	20.0	3.4502E-04	14.492
9	5.00	20.0	3.4819E-04	14.360
10	5.00	20.0	3.5635E-04	14.031
		Average:	3.5409E-04	14.126

Table 4.2: Velocity gauge calibration test results.

Across all of the calibration tests conducted, the average calibration constant was found to be $\mu = 14.126$. This value was taken to be the calibration constant for the material tests, all of which were conducted at amplifier gains of 101.3. Understandably, if more calibration tests were to be conducted, the average value would better represent the characteristics of the velocity gauges; however, the results shown in *Table 4.2* are in good agreement and no additional tests were deemed necessary. The determined calibration constant value can be compared with the expected value based on the perceived gauge length (the diameter of the bar), measured magnetic field, and gain used during the experiments. Using *Equation 4.4*, the expected value is therefore:

Magnetic Field (G):	421
Amp Gain:	101.3
Gauge Length (mm):	15.875

$$\mu = \frac{1}{(101.3)(0.0421\ T)(0.015875\ m)} = 14.77\ \frac{m/_s}{V}$$

It is believed that the difference between the calibration test value and the expected value is mainly due to the effect of the gauge wire not within the diameter of the pressure bars. For the wire gauge theory in *Section 2.2.1*, the diameter of the lead wires

spanning through the magnetic field was not addressed, but it could theoretically increase the effective wire cutting orthogonally through the magnetic field. Also, there is additional unaccounted wire that is exposed out from the diameter of the bar so that the wire is able to turn, parallel to the magnetic field, with shielding and all. These additional accounts of wire exposed to the magnetic field may seem insignificant; however, if the gain and measured magnetic field are taken to be absolutely true, using *Equation 4.4* and the calibration constant found through testing would reveal an effective gauge length of $l_g = 16.599\ mm$. This shows that, in this experimental setup, around 0.72 mm of additional unaccounted wire, orthogonal to the central magnetic field, is enough to change measured velocities more than 0.64 m/s per volt. A quantity that could considerably affect test results. Alternatively, if the gain and assumed gauge length (bar diameter) were taken to be absolutely true, the actual central magnetic field strength would be 19.2 G greater than that measured. This is a highly improbable field variation in this region between the coils. Hence, the magnetic field is not likely a source of the calibration constant difference. Furthermore, the amplifier gains determined using circuit theory were verified using known DC inputs and measuring the channel outputs, so the amplifiers are also not likely erroneous. The unaccounted effect of a relatively small amount of wire, however, is certainly possible in the experimental setup. Therefore, it was determined that the difference in the calibration constant expected value and the test value is likely due to an additional wire effect within the magnetic field. The calibration constant found through the calibration tests accounts for such additional effects and thus, is to be considered as a more accurate value for converting voltage to velocity.

5. Experimentation

5.1 Introduction

Once the necessary preliminary steps have been taken to properly record data with the velocity gauges, experimentation can begin. This study will look at two different viscoelastic test specimens: Solid polyurea and banded polyurea foam. The banded foam specimens are a composition of polyurea foam disks with a solid band of polyurea around the outer face. The goal for the experiments is to record a stress and strain history while maintaining as constant of a strain-rate as possible during the compression portion of the test event. Upon conducting a test with an approximately constant strain-rate, the corresponding stress-strain data will provide material-characterizing information for that strain-rate only, as characteristics of viscoelastic material change depending on the rate of loading. Tests will be carried out across a range of strain-rates to illustrate the change in material response as the strain-rate changes. The effect of strain-rate on the stress-strain relationship, energy dissipation, storage modulus, and loss factor were all of interest.

5.2 Pulse Shaping

Pulse shaping is the process of attaching an additional piece of material to the face of the incident bar that interacts with the striker to manipulate the propagating wave prior to reaching the test specimen. The wave is manipulated so that the strain-rate during material loading can be held at a more constant value. Materials with impedances lower than that of the pressure bars are typically effective in altering the wave shape in a way so that these improvements are made. For all tests conducted, cylindrical solid polyurea pulse-shapers with the same diameter of the pressure bars were used. The pulse-shapers

were adhered to the face of the incident bar with a thin layer of grease. The thickness of the pulse shaper used for tests depended on the thickness of the test specimen and the intensity of the test as well. Generally, to hold the strain-rate approximately constant during testing, pulse-shapers with thicknesses equal to or greater than the thickness of the test specimen were needed.

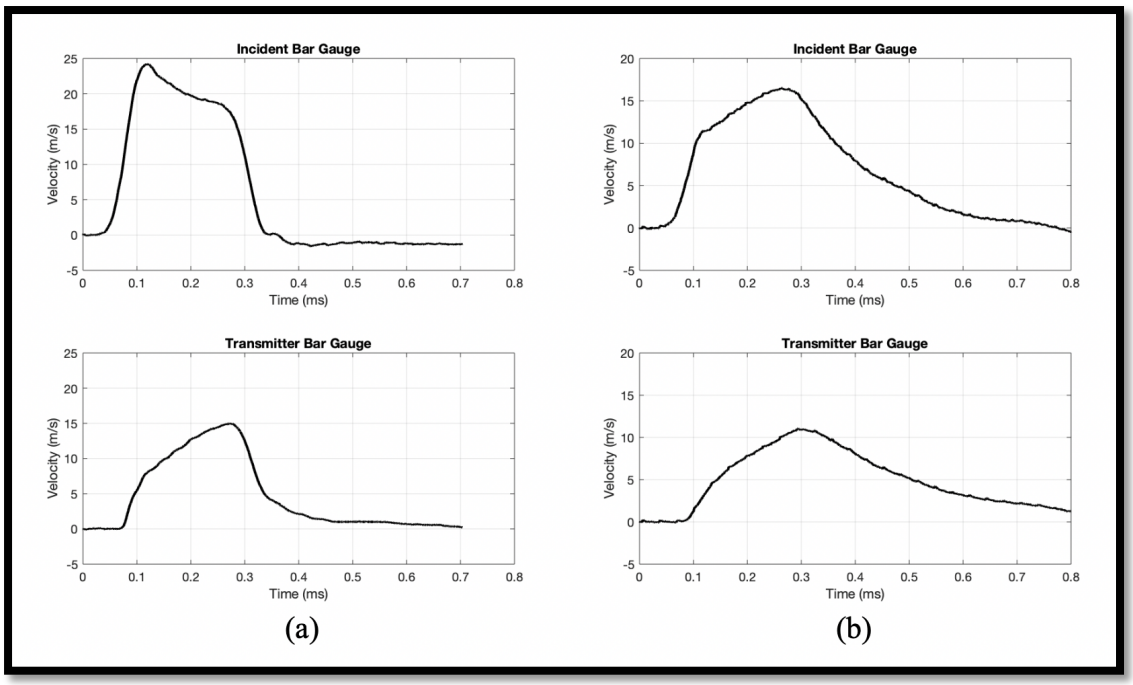

Figure 5.1: Velocity gauge signals from a similar test completed with (a) no pulse-shaper, and (b) a 5 mm pulse-shaper.

To highlight the importance and effect of pulse shaping, two tests were conducted using the same setup with the only difference being the use of a pulse-shaper. Both tests were completed with the 152.4 mm polycarbonate striker at a firing pressure of 15 psi and a 3.20 mm-thick, 15.87 mm-diameter solid polyurea test specimen. *Figure 5.1(a)* shows the velocity signals from the gauges when there is no pulse-shaper, and *Figure 5.1(b)* shows the signals when a 5 mm-thick pulse-shaper was placed on the incident bar. Using *Equations 2.5*, *2.6*, and *2.7*, to convert the signals to strain-rate, strain, and stress respectively, *Figure 5.2* shows the corresponding stress-strain results. Note that when the

pulse-shaper was introduced, the strain-rate, in *Figure 5.2(b),* is improved to a nearly constant value. This acceptable result allows confident conclusions to be made about the viscoelastic material's characteristics at a strain-rate magnitude of about 2200 s^{-1}.

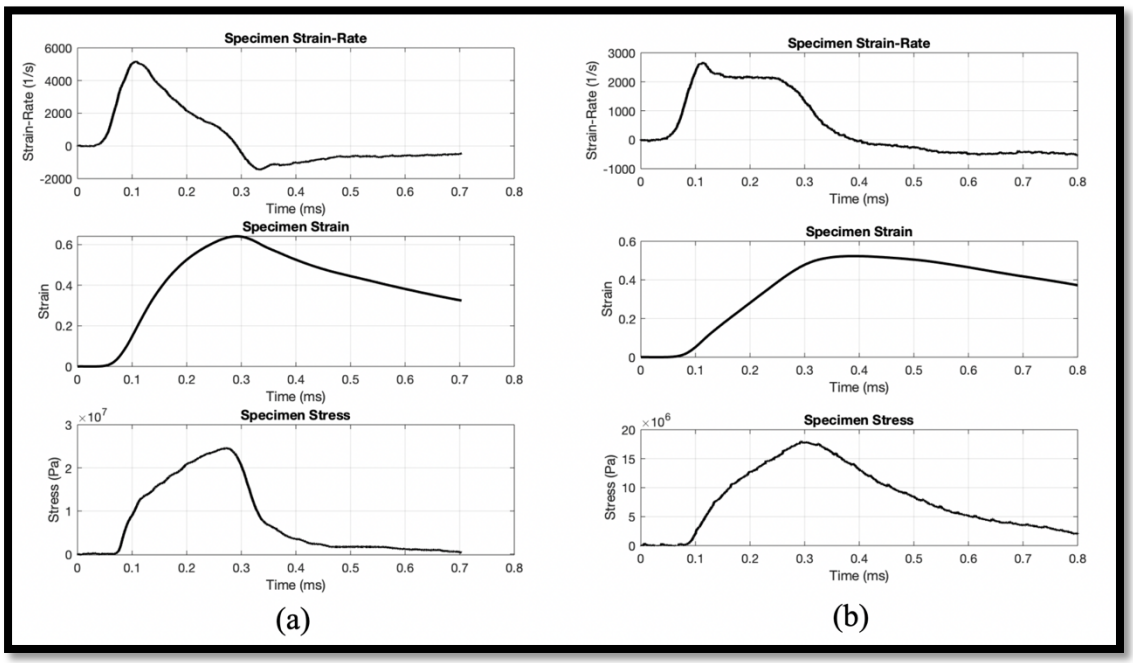

Figure 5.2: Stress-strain results of a similar test completed with (a) no pulse-shaper, and (b) a 5 mm pulse-shaper.

5.3 Solid Polyurea

5.3.1 *Overview*

The solid polyurea test specimens were created by pouring the two-part uncured material mixture into a low-friction acetal plastic cylindrical mold with precise dimensions. When removed from the mold after curing, each specimen was handled with care so that no significant strains were applied prior to the testing. A non-zero strain history prior to testing a specimen could negatively affect the characterization results. Any non-zero pre-test strain history would be unaccounted for when applying the BSP

and carrying out the GMM modeling procedure highlighted in *Section 3.3*. Before testing, the specimens were visually inspected for defects such as air pockets, and using a digital caliper, the specimens were measured to verify the desired dimensions. The tests for the solid polyurea material were conducted using the 152.4 mm striker at room temperature. Initially, the 304.8 mm striker was used to perform testing; however, it became difficult to reach desired higher strain-rates with the achievable gas gun pressures. Using the lighter 152.4 mm striker produced strain-rate results higher than those of the 304.8 mm striker. For the tests conducted, test specimens had thicknesses of 3.25 ± 0.10 mm and diameters of 15.83 ± 0.05 mm. *Figure 5.3* shows a solid polyurea test specimen in between the pressure bars prior to testing. In the photo, the green velocity gauges are also visible within the bars.

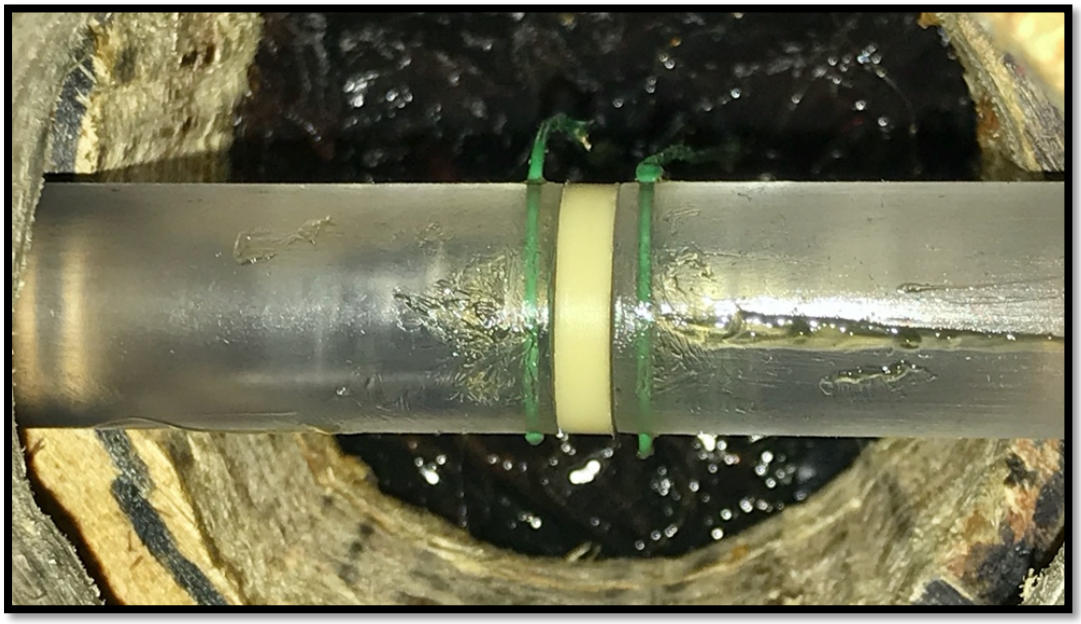

Figure 5.3: A solid polyurea specimen between the pressure bars prior to testing.

5.3.2 *Stress-Strain Results*

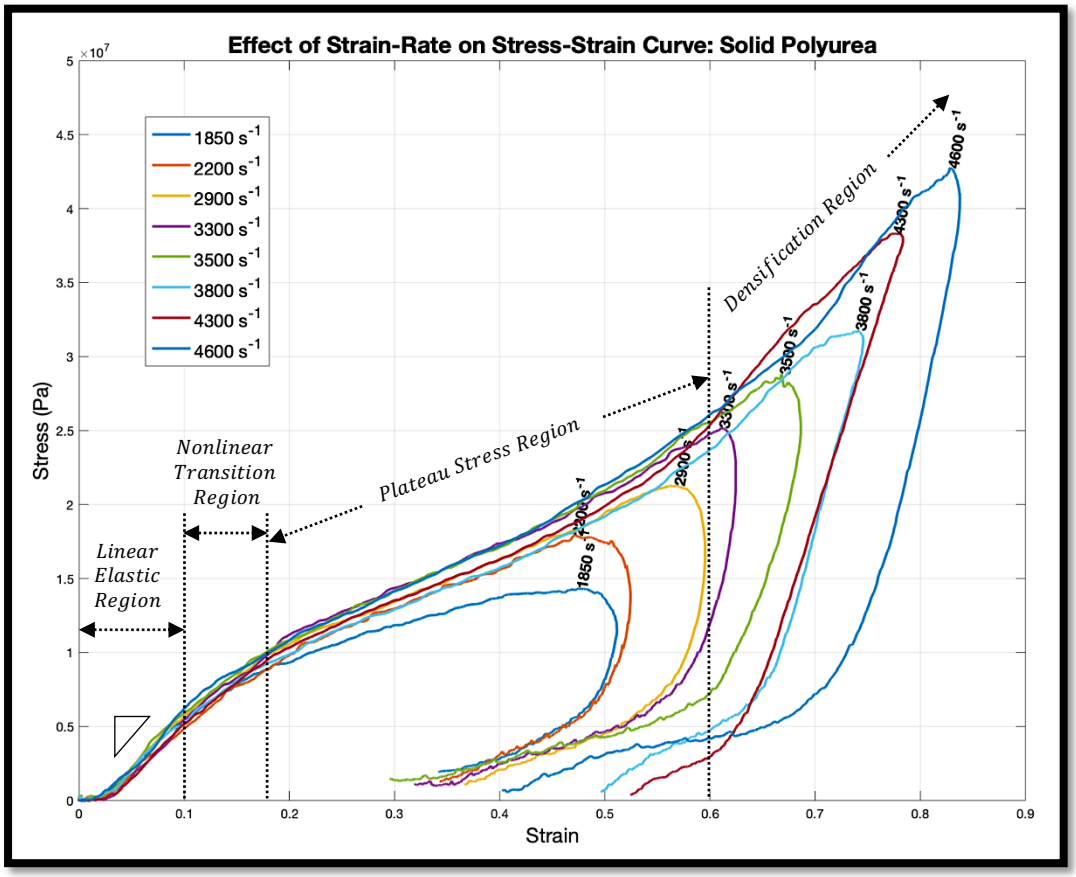

Figure 5.4: Effect of strain-rate on stress-strain curve for solid polyurea.

Tests of varying gas gun firing pressures were carried out with appropriately sized pulse-shapers. Upon capturing multiple datasets (like that in *Figure 5.2(b)*) with a range of strain-rate values, the stress-strain curve assembly in *Figure 5.4* was generated for the solid polyurea material. A total collection of the stress-strain test results can be found in *Appendix B*. For the tests with strain-rates 3800 s^{-1} and above, it was especially difficult to pulse shape in a way that could hold the strain-rates at a constant value. The strain-rate values that characterize these three tests are the maximum values measured. The strain-rate variation for these tests is certainly noteworthy and should be taken into consideration when drawing conclusions about the material at these rates. Regardless, the

stress-strain curves for these tests appear to follow the trends set by those tests of lesser strain-rates, so it is untrue to say that the tests of strain-rates 3800 s^{-1} and above are valueless. In addition, it appears that for these strain-rates, the material experienced notable densification. The densification of viscoelastic material is characterized by a larger increase in material stress accompanied with only slight softening of the material [15]. This densification was difficult to combat when trying to appropriately pulse shape. *Figure 5.4* displays the densification region on the stress-strain curve and also highlights the other stress regions typical of viscoelastic materials.

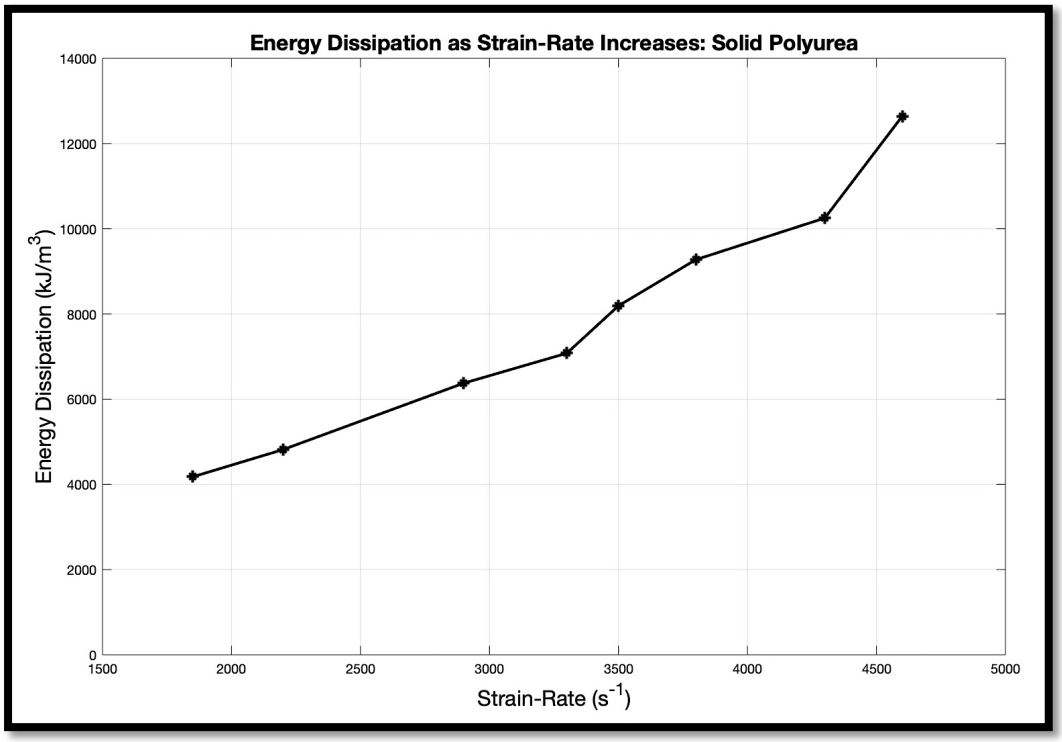

Figure 5.5: Energy dissipation as strain-rate increases for solid polyurea.

The amount of energy the material specimen dissipated per unit volume for each test can be determined by integrating the individual stress-strain curves. *Figure 5.5* displays the energy dissipated by solid polyurea during the tests as a function of strain-rate. These values can also be found in *Appendix C*. The energy dissipation trend appears

to be fairly linear up to 3300 s^{-1}, but above this strain-rate, around when densification effects are observed, larger increases in energy dissipation were recorded.

5.3.3 *Relaxation Modulus, Storage Modulus, and Loss Factor*

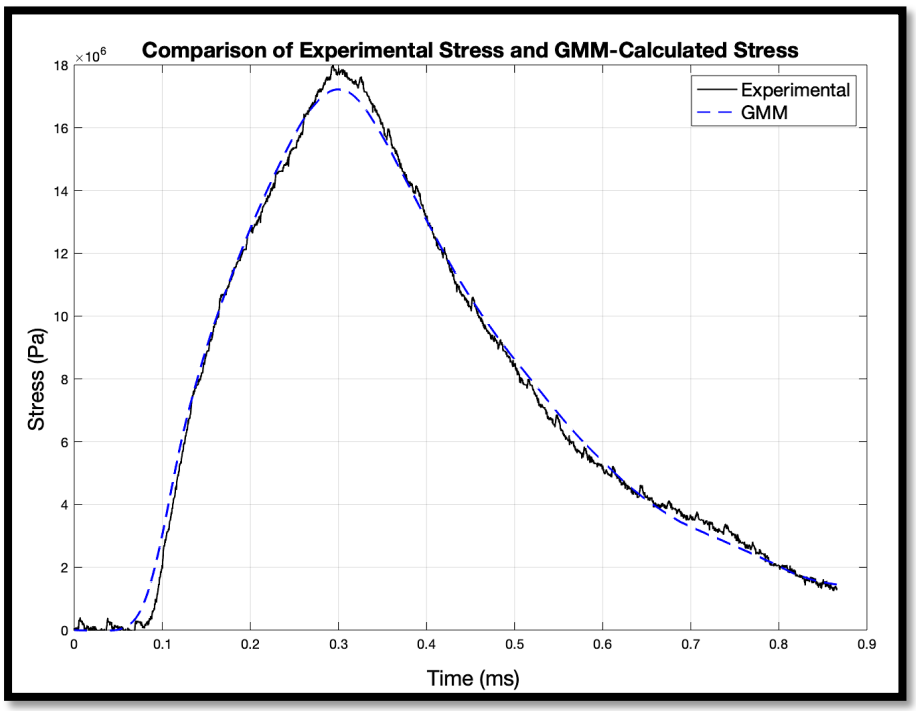

Figure 5.6: Comparison of experimental stress and GMM-calculated stress.

Upon collecting stress-strain data for the various strain-rate values, the optimal GMM parameters were found by solving the optimization problem described in *Section 3.3* with MATLAB. For this material, ten spring-damper elements were included in the optimization process. Note, the model had 21 total parameters to solve for with this quantity of GMM elements. It was observed that the more parametric the optimization became, the more MATLAB's optimization function struggled to converge on a solution. Solving for 21 GMM parameters was feasible; however, it was crucial to give appropriate parameter initial conditions to the MATLAB solver in order to derive a satisfactory set of solution values. The optimal GMM parameter values found by MATLAB and the model-

calculated elastic modulus, for all tests conducted, are given in *Appendix C*. The GMM results suggest that the elastic modulus of the material is around 70 MPa, which agrees with the slopes of the stress-strain curves in the linear-elastic region. *Figure 5.6* exhibits how effective the GMM can be at representing the material's relaxation modulus. The figure compares the experimentally measured specimen stress from the 2200 s^{-1} strain-rate test and the GMM stress computed using the optimized parameters, measured specimen strain-rate, and *Equation 3.25*.

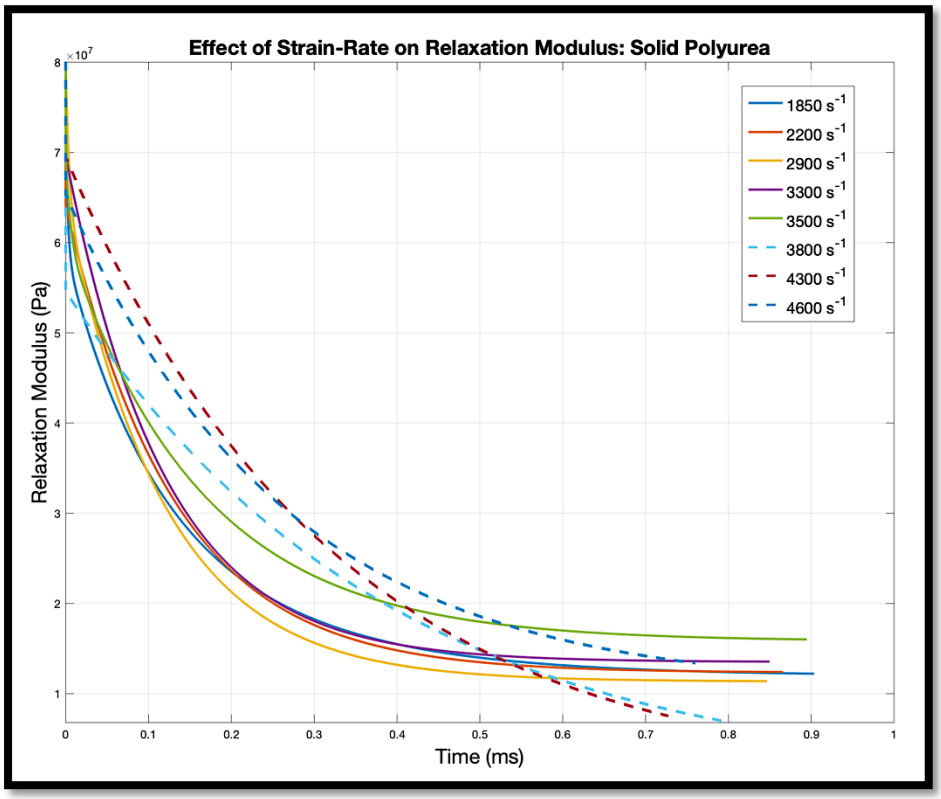

Figure 5.7: Effect of strain-rate on relaxation modulus for solid polyurea.

Figure 5.7 shows the relaxation modulus found by the GMM for the solid polyurea tests. The dashed plot lines correspond to tests where the GMM optimization process produced poor results. The poor fit results for the higher strain-rate tests are likely due to the presence of additional nonlinearities in the material response. These nonlinearities are evident by observing the stress-strain curves in *Figure 5.4* and

comparing them to typical linear-viscoelastic stress-strain curves. The curves reveal that nonlinearities must be present to generate such responses. The nonlinearities could be material geometry related and/or material characteristic related. As Brinson and Brinson describe, geometric nonlinearities can occur with large material strain. For large strain values, the linearized definitions of stress and strain are no longer valid. Furthermore, material nonlinearities occur in the presence of nonlinear constitutive relationships [14]. Recall the constitutive equation for a GMM element, *Equation 3.10*. Since this equation is a linear differential equation, the GMM is likely not suitable for representing the material's nonlinear characteristics at higher strain-rates. Although full of additional complexities, a nonlinear model should be considered instead to accurately analyze frequency domain characteristics across a wider range of strain-rates.

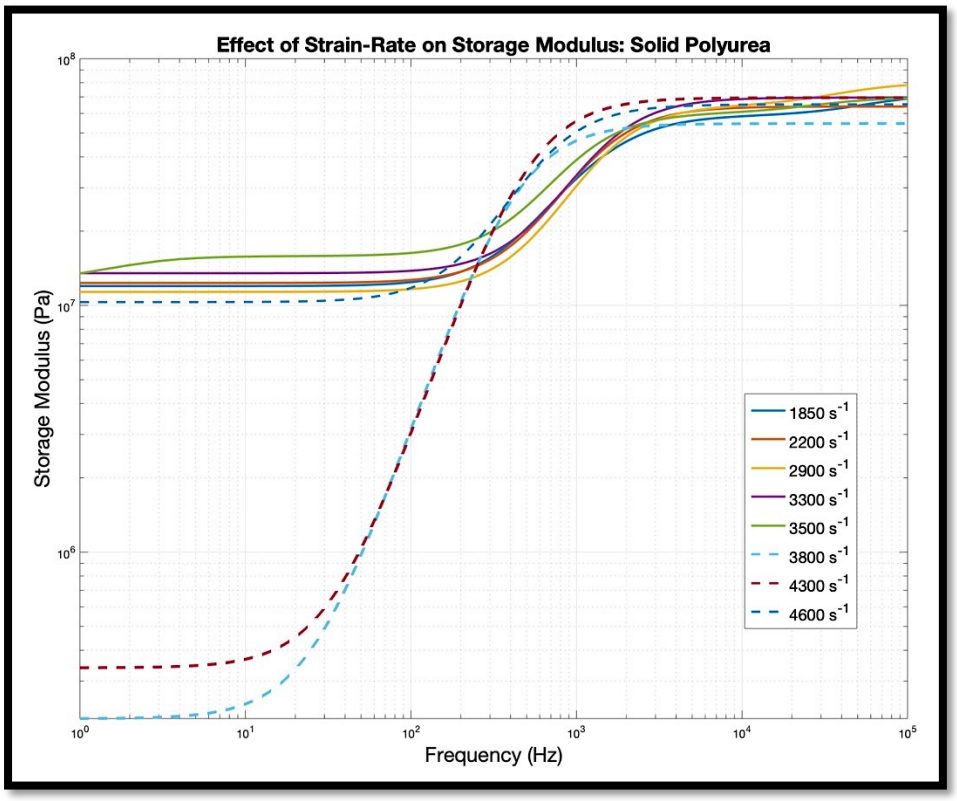

Figure 5.8: Effect of stain-rate on storage modulus for solid polyurea.

Figures 5.8 and *5.9* show the storage modulus and loss factor for the completed tests. Disregarding the poor model fits, no significant differences are observed for these characteristics at the strain-rates tested. The storage modulus results reveal that the material's transitional region from a rubbery plateau region to a glassy region exists between approximately 200 Hz and 4000 Hz. Accordingly, no additional material elasticity is anticipated for excitations above 4000 Hz. The loss factor results reveal that the material has optimal damping characteristics between 475 Hz and 550 Hz.

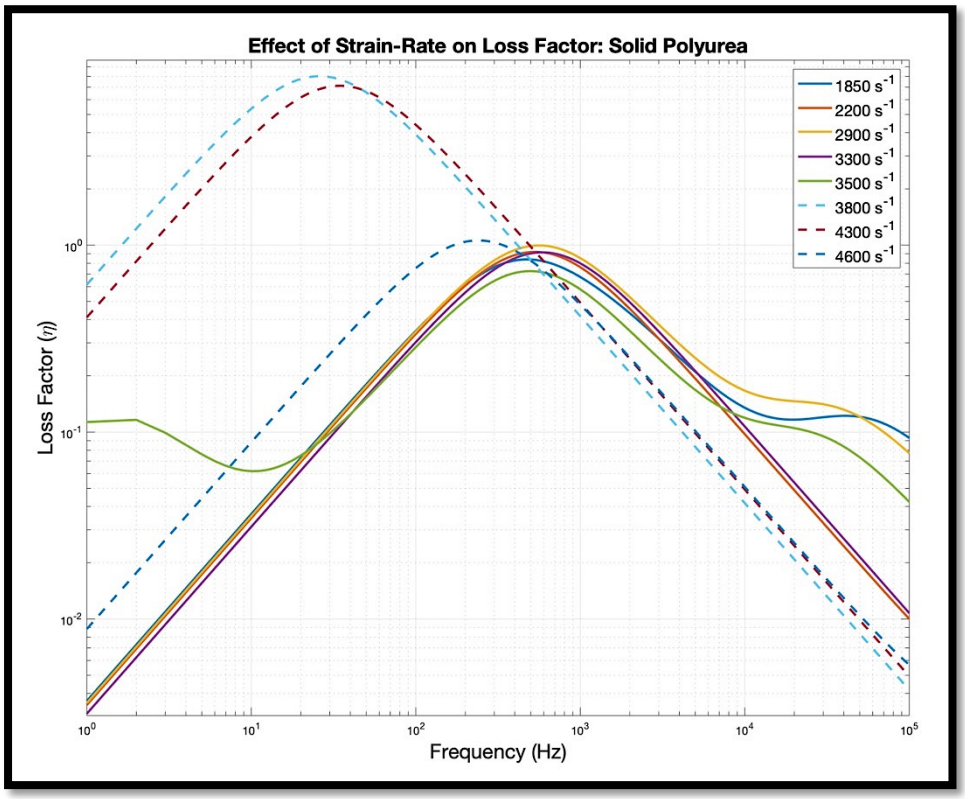

Figure 5.9: Effect of stain-rate on loss factor for solid polyurea.

5.4 Banded Polyurea Foam

5.4.1 *Overview*

The banded polyurea foam specimens were created by pouring the uncured solid polyurea two-part mixture onto a rotating acetal plastic rod wrapped with a thin fiberglass

mesh. Additional hollow acetal cylinders were fitted over the rod to restrict where on the rod the material could adhere. Upon curing, each ring-shaped material piece was carefully removed to ensure no significant strains were applied. To create the polyurea foam centers, the foam was cut to shape with a precision knife and gently pressed within the solid polyurea band. This specimen construction process was carefully carried out so that the specimens would have similar dimensions. However, it should be noted that due to the unique composition of these test specimens, there may have been dimensional variations that could have had minor influences on test results. Of most concern was the variation of the band inner diameter and its uniformity around the foam center. The finalized test specimens can be seen in *Figure 5.10*. The tests for the banded polyurea foam specimens were conducted using the 152.4 mm striker at room temperature. For the tests conducted, test specimens had thicknesses of 3.35 ± 0.15 mm and diameters of 14.40 ± 0.10 mm.

Figure 5.10: Photo of banded polyurea foam test specimens.

5.4.2 *Stress-Strain Results*

Like with the solid polyurea specimens, tests of varying gas gun firing pressures were carried out with appropriately sized solid polyurea pulse-shapers. Upon capturing

multiple datasets with a range of strain-rate values, the stress-strain curve assembly in *Figure 5.11* was generated for the banded polyurea foam composites. A total collection of the stress-strain test results can be found in *Appendix B*. Higher strain-rates were achievable compared to the solid polyurea tests, because the banded foams were softer in nature. Much higher strain-rates could have been recorded, but a high-speed video recording of the 5900 s^{-1} test showed that the specimen expanded radially such that some of the solid polyurea band was no longer in contact with the pressure bars. As a result, higher strain-rate tests were not sought after, since the band of the test specimens would no longer be contributing to the specimen responses for full test durations.

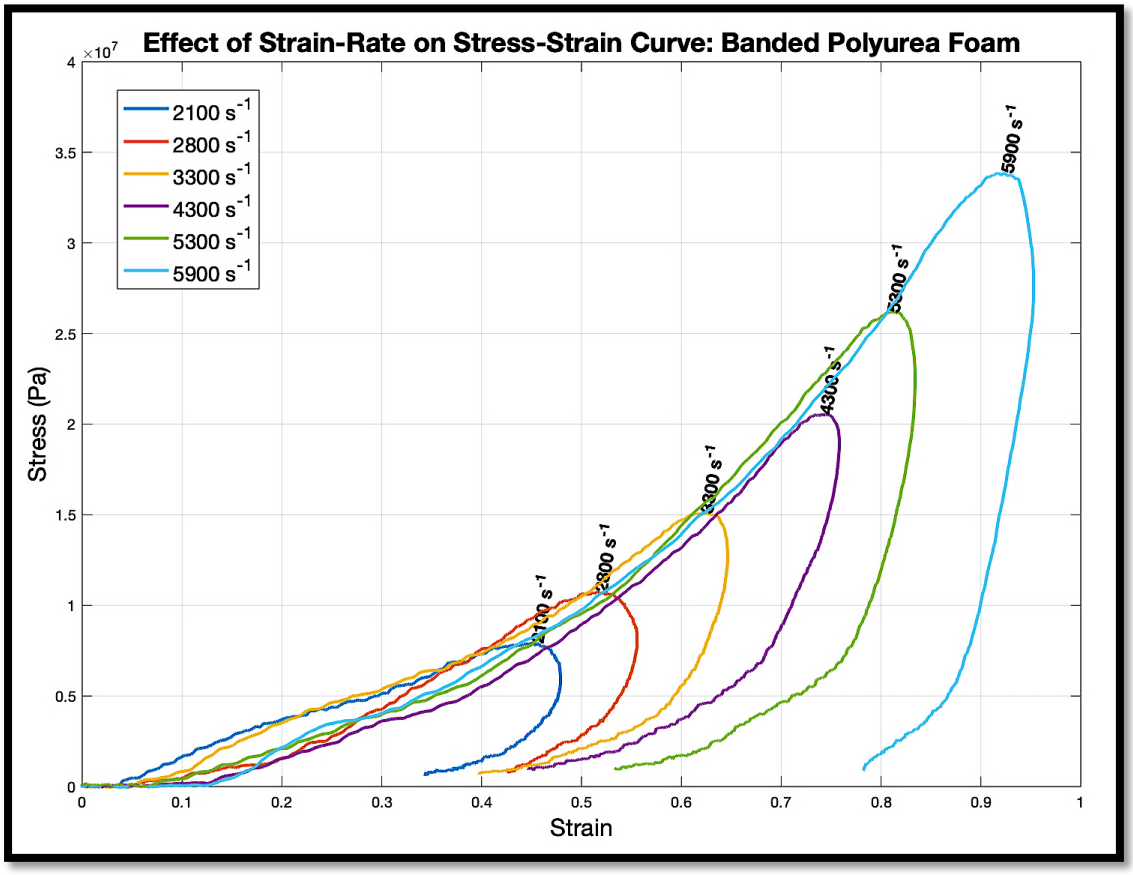

Figure 5.11: Effect of strain-rate on stress-strain curve for banded polyurea foam.

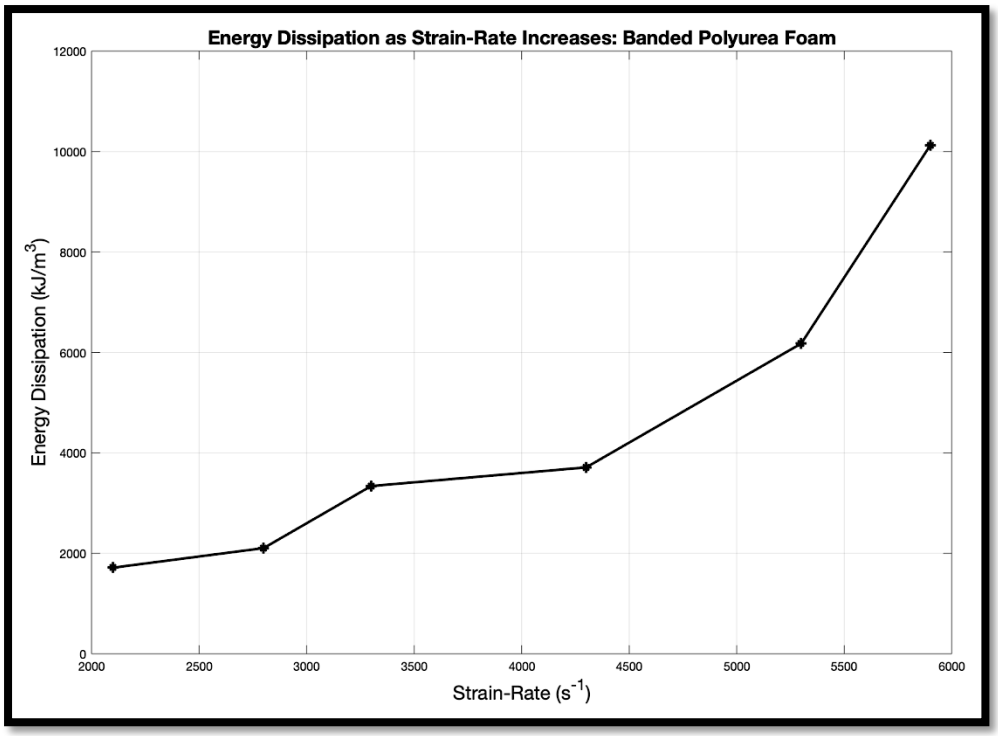

Figure 5.12: Energy dissipation as strain-rate increases for banded polyurea foam.

The stress-strain curves reveal more significant nonlinearities than those of the solid polyurea. There also seems to be only a subtle linear elastic curve region, and the plateau stress region that was observed with the solid polyurea tests is seemingly nonexistent. Based off of the shape of the stress-strain curves, it appears that the majority of the responses behaved in a densification-type manner. Because of the specimens' foam composition and lack of rigidity, these responses were anticipated. Furthermore, it is believed that the reason the initial stress values occur at non-zero strain values is because of the lack in material rigidity. Since the stress values are measured purely using the transmitter bar velocity gauge, a more notable delay in wave propagation between the two gauges could have generated this effect. Despite the banded foams recovering a surprising amount of their original geometry, high-speed video highlights the specimens' softness by showing how they seemingly crush during testing. In addition, it should be

noted that the only stress-strain curve that displayed any sort of linear-viscoelasticity is the 2100 s^{-1} curve. This foreshadows the unsatisfactory results the linear GMM produced when curve fitting to the specimen response data. *Figure 5.12* displays the energy dissipated by the banded polyurea foam tests as a function of strain-rate. These values can also be found in *Appendix C*. Comparing only solid polyurea tests with alike strain-rates, the energy dissipation trend for the banded foams appears similar. However, because higher strain-rates were achievable with the banded foams, a more exponential trend was observable as strain-rate increases, which is a good quality to have for impact-mitigating materials.

5.4.3 *Relaxation Modulus, Storage Modulus, and Loss Factor*

As mentioned, the GMM optimization process for the nonlinear data of the banded polyurea foams produced poor results. For the solid polyurea tests, the linear GMM was able to provide quality data modeling for the majority of the tests collected. In contrast, the GMM was only able to adequately fit the 2100 s^{-1} response data. Although optimal GMM relaxation modulus curves were found, shown in *Figure 5.13*, a comparison of the GMM-calculated stress signals (found using *Equation 3.25*) and the experimental stress signals demonstrated how poorly the model represented the specimen responses. The dashed line of the 5900 s^{-1} test highlights its significant deviation from the other GMM results, but again, most of the results are poor representations of what occurred experimentally.

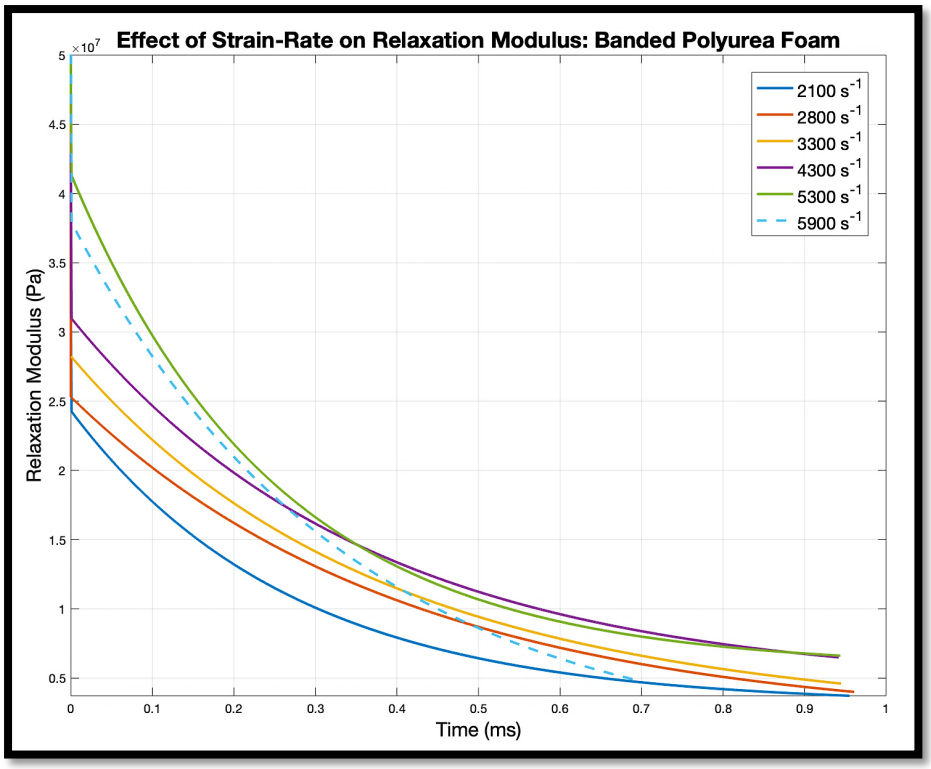

Figure 5.13: Effect of strain-rate on relaxation modulus for banded polyurea foam.

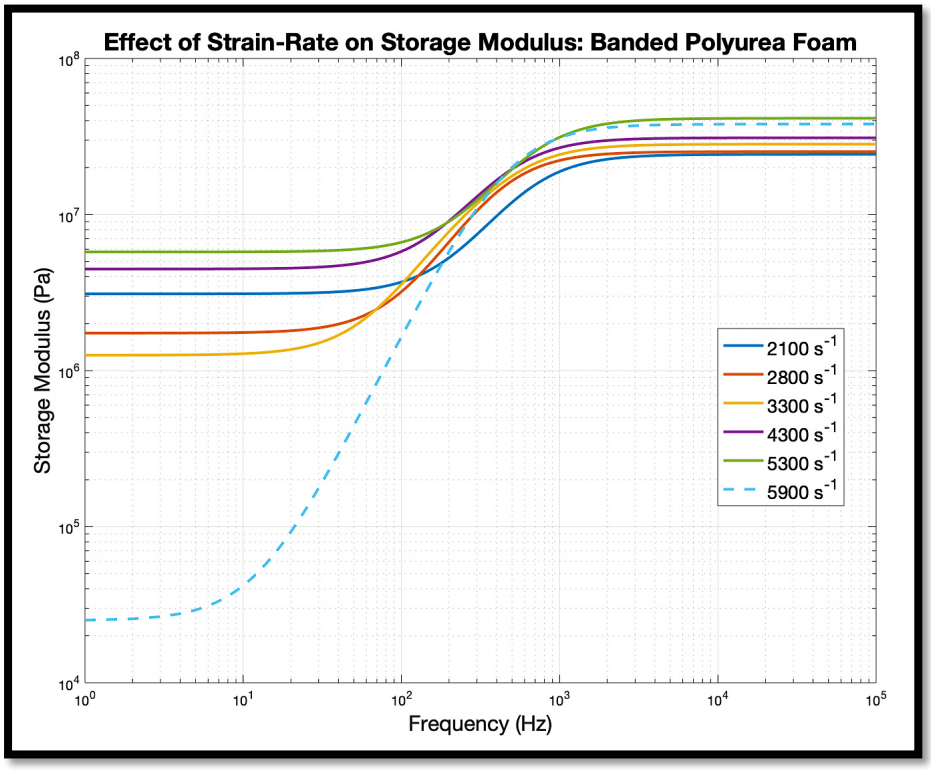

Figure 5.14: Effect of stain-rate on storage modulus for banded polyurea foam.

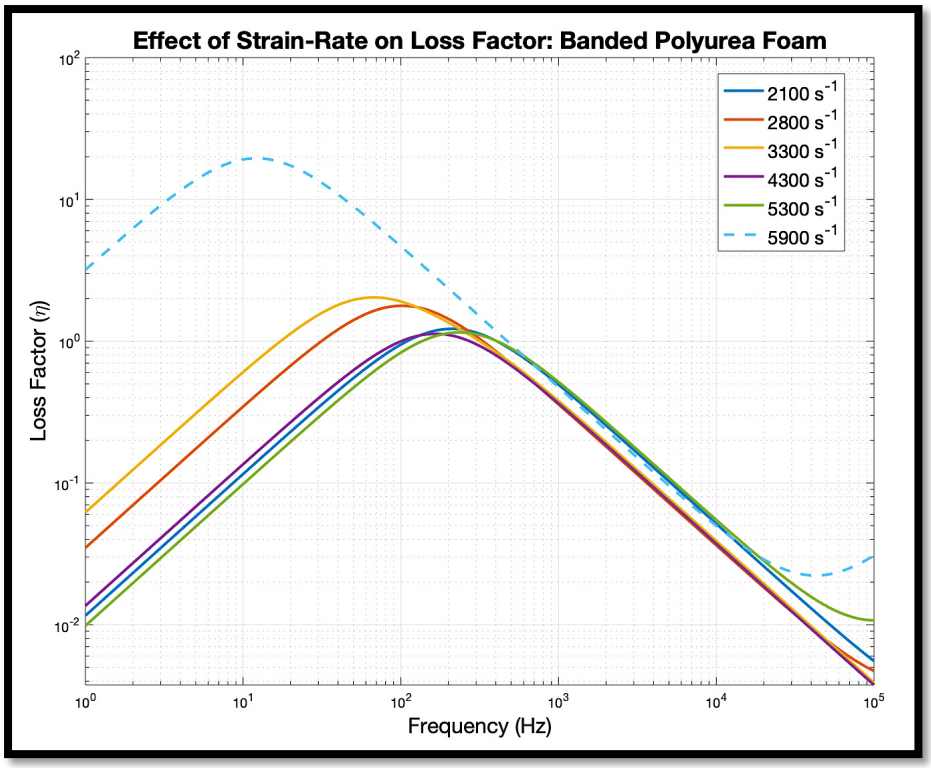

Figure 5.15: Effect of stain-rate on loss factor for banded polyurea foam.

Since the GMM only satisfactorily modeled the 2100 s^{-1} test, only frequency domain results for this test are credible. Analyzing this test's storage modulus plot in *Figure 5.14* shows that, for a strain-rate of 2100 s^{-1}, an elasticity transition region exists between 100 Hz and 2000 Hz. Compared to the solid polyurea tests as a whole, this is a shorter bandwidth of smaller frequency magnitudes, suggesting the banded foams may begin to stiffen at lower excitation frequencies and also reach its glassy region sooner as excitation frequency increases. However, as one may expect, the magnitude of the banded foam storage modulus curve is of smaller magnitude than that of the solid polyurea. Understandably, the addition of foam to the test specimen composition will decrease its total stiffness. The 2100 s^{-1} loss factor results, shown in *Figure 5.15*, suggest that at this strain-rate, the banded foam has optimal damping characteristics around 200 Hz, which is an eye-catching value when compared to that of the solid polyurea results.

For impact-mitigating materials, having effective damping characteristics at lower excitation frequencies is ideal, as many impact wave profiles contain large amounts of low frequency energy. To reiterate once more, despite some of the other strain-rate tests producing frequency domain results similar to the 2100 s^{-1} test, the GMM for these tests did not fit well to the experimental data.

5.4.4 *A Nonlinear Approach*

With the linear GMM properly modelling only one of the banded polyurea foam tests, existing approaches to modeling nonlinear viscoelasticity were researched for possible future work. A further examination of publications by Fung [16], Selyutina et al. [17], and Pryse et al. [18] would serve as an appropriate primer for the continuation of this study. Of the methods presented by Provenzano et al. [19], an approach similar to the quasilinear viscoelasticity (QLV) method was explored. The QLV method, presented by Fung [20] in 1972, introduces an additional function to the BSP convolution integral that is solely dependent on strain, not time. As described by Provenzano et al. [19], the QLV method takes the relaxation modulus of the viscoelastic material to be both time-dependent and strain-dependent, i.e. $E^r(t, \varepsilon)$. Taking the relaxation modulus to be composed of two independent functions of time and strain yields:

$$E^r(t, \varepsilon) = E_t(t)g(\varepsilon) \tag{5.1}$$

*Equation 5.*1 is obtained using the separation of variables principle, where $E_t(t)$ is a time-dependent modulus function and $g(\varepsilon)$ is a strain-dependent nonlinearizing modulus function. The BSP convolution integral is now nonlinearized and given as:

$$\sigma(\varepsilon, t) = \int_0^t E_t(t-\tau)g(\varepsilon)\frac{\partial \varepsilon(\tau)}{\partial \tau}d\tau \tag{5.2}$$

If the linear GMM is independent of strain, $E_t(t)$ can be taken to be $E^r(t)$ from *Equation 3.16*. Furthermore, in order to solve for some $g(\varepsilon)$ that improves the modeling of the experimental response data, $g(\varepsilon)$ was taken to be a seventh order polynomial, or:

$$g(\varepsilon) = \sum_{j=0}^{7} \alpha_j \varepsilon^j \tag{5.3}$$

where α_j are unknown parameters. Thus, given experimental strain-rate and strain data and also the linear GMM results from completing the optimization problem in *Section 3.3*, the nonlinear model stress is:

$$\sigma_{NL}(\varepsilon, t) = \int_0^t \left[E_0 + \sum_{k=1}^{n} E_k e^{-(t-\tau)/\rho_k} \right] \left[\sum_{j=0}^{7} \alpha_j \varepsilon_s^j \right] \frac{\partial \varepsilon_s(\tau)}{\partial \tau} d\tau \tag{5.4}$$

Again, E_k and ρ_k are already determined parameters found by fitting the linear GMM to experimental stress data. The α_j parameters are found by using MATLAB's fmincon( ) function to solve the optimization problem:

$$\left\langle \begin{array}{c} \text{Solve for } \alpha_j \text{ for } j = 0, \dots, 7 \\ \text{to minimize } F = \sum_{t=0}^{t=T} [\sigma_s(\varepsilon, t) - \sigma_{NL}(\varepsilon, t)]^2 \\ \text{such that } -\infty < \alpha_j < \infty \text{ for } j = 0, \dots, 7 \end{array} \right\rangle$$

where $t = 0$ marks the time at the beginning of the stress signal (prior to $t = 0$ there is only zero-valued stress and strain), T marks the end time of the test event, and $\sigma_s(\varepsilon, t)$ is the experimental stress data. As stated in *Section 3.3*, because discrete data points from SHPB tests are being handled and not continuous functions, MATLAB's conv( ) function can be used to convolve the integral functions. The MATLAB script to carry out this process is not included in this thesis, but a thorough understanding of the

optimization process in the script in *Appendix A* should enable one to generate their own code.

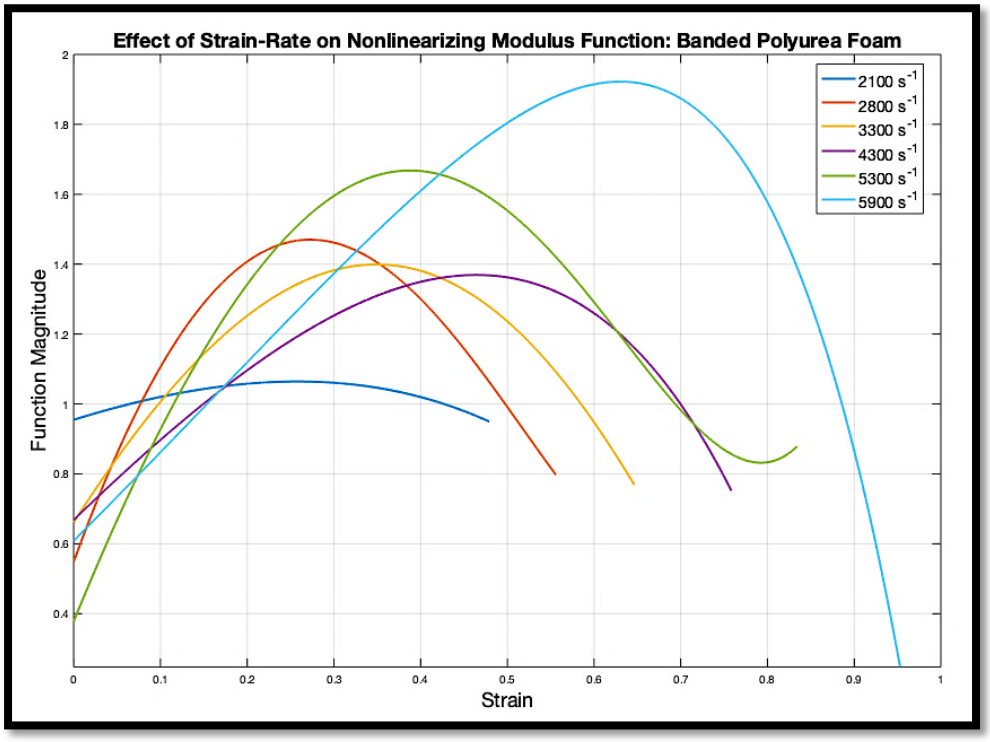

Figure 5.16: Effect of strain-rate on nonlinearizing modulus function for banded polyurea foam.

After carrying out the nonlinear model optimization process for the each banded polyurea foam test, the optimal α_j parameters were found and are listed in *Appendix D*. The corresponding nonlinearizing modulus functions, $g(\varepsilon)$, can be seen in *Figure 5.16*. Note that the closer the function values are to a value of 1, the more the nonlinear model resembles the linear GMM. As mentioned earlier, the 2100 s^{-1} banded foam test was the only test that displayed any sort of linear-viscoelastic response. The corresponding nonlinearizing modulus function for the test supports this statement by demonstrating that $g(\varepsilon)$ holds closer to a value of 1 more than any of the other tests.

Figure 5.17 shows the plots for the modified relaxation modulus: $E^r(t,\varepsilon) = E^r(t)g(\varepsilon)$. Significant differences can be seen when comparing the nonlinear modified

relaxation modulus curves to the linear GMM relaxation modulus curves in *Figure 5.13*. *Figure 5.17* accentuates the type of relaxation modulus function shape needed to properly model some of these nonlinear viscoelastic material responses.

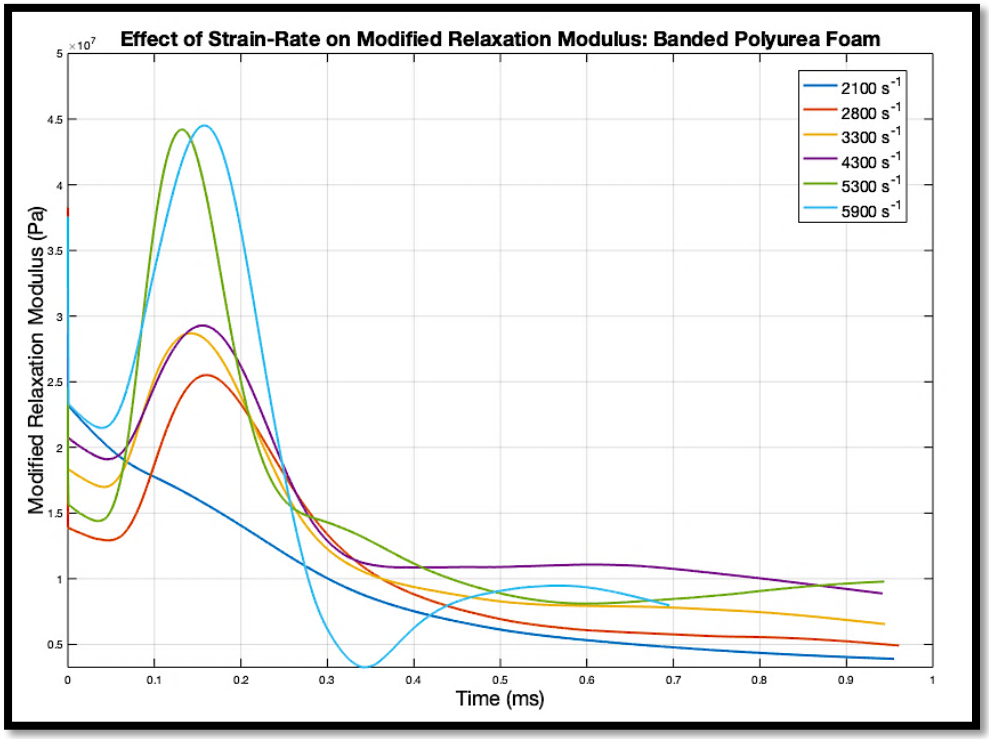

Figure 5.17: Effect of strain-rate on modified relaxation modulus for banded polyurea foam.

Figure 5.18 exhibits the data modelling improvements seen when using the nonlinear model versus the linear GMM. The figure compares the experimentally measured specimen stress from the 5300 s^{-1} strain-rate test, the linear GMM computed stress (using *Equation 3.25*), and the nonlinear model computed stress (using *Equation 5.4*). Note how the linear GMM fails to accurately fit the experimental data, as it did with most of the banded foam test results, and note the substantial improvement made by applying the nonlinear model.

Unfortunately, many complexities are encountered when trying to convert the nonlinear model from the time domain to the frequency domain. Perhaps a unique form

of the nonlinearizing modulus function is necessary to make the model mathematically more suitable for this conversion. Nevertheless, it is anticipated that additional extensive research will be required to develop a method for extracting accurate frequency domain information from the nonlinear specimen response data within this study. The methodology explored here in *Section 5.4.4* was presented to help demonstrate the kind of processes that may be required to accomplish such a task.

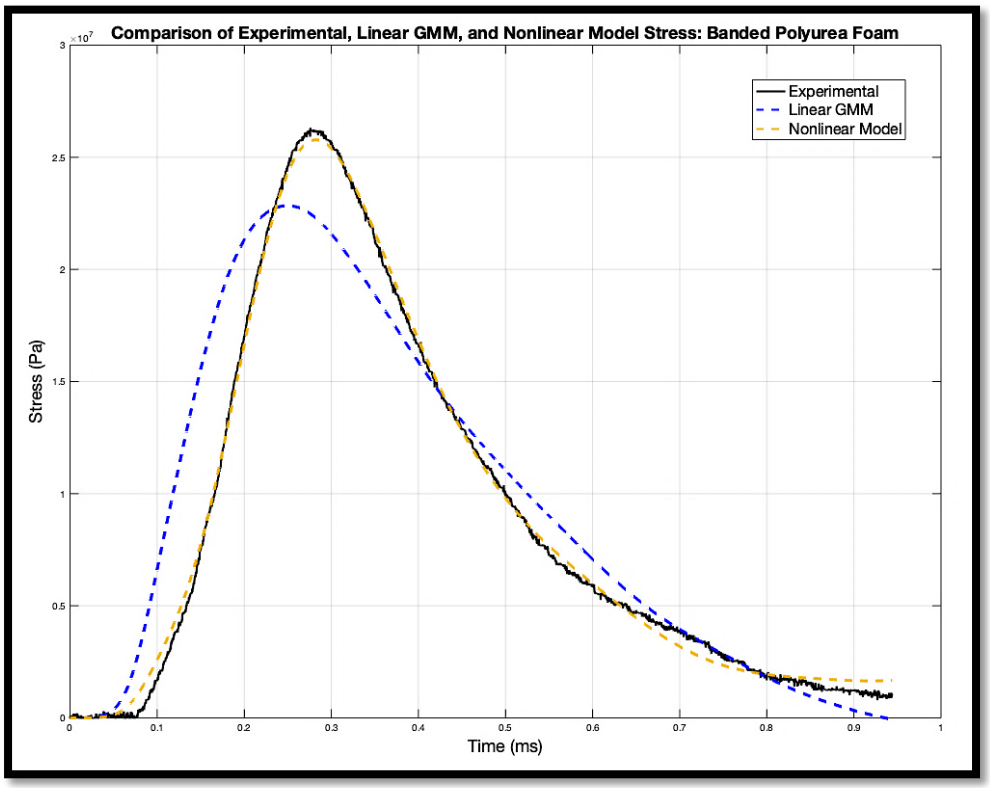

Figure 5.18: Comparison of experimental, linear GMM, and nonlinear model stress.

6. Concluding Remarks

The results obtained from this study are satisfactory, especially given the newness of the test setup to the author. For each material, strain-rates that induced nonlinear material behavior were determined, and energy dissipation trends were examined as strain-rate varied. Furthermore, meaningful frequency-domain characteristics were obtained, and for some strain-rates, GMM parameters that accurately represent the materials were found. These parameters, while an integral part of the frequency-domain analysis, can be used for other purposes such as computer simulations. The parameters and relaxation modulus of the materials when integrated into certain simulations can provide information on how the materials will respond to other stress loads without the need for experimentation. Note that the optimization process, from which the optimal parameters are derived, is not limited to the velocity gauge instrumented SHPB and can be applied to the conventional SHPB test setup or any test setup that captures specimen stress and strain-rate histories.

It should be emphasized that the results presented assumed that the geometry of the test specimens remained the same throughout the test events. As video evidence would support, some of the tests saw significant radial expansion of the viscoelastic specimens. With more rigid materials, these geometric changes are slight and often negligible; however, with the soft materials in this study, these geometric changes are more significant and considerably increase stress measurement error. Implementing a manner in which to track the change in geometry throughout the test event would be ideal, but a more achievable objective would be to complete a study that determines the optimal ratio of specimen diameter to specimen thickness that minimizes radial

expansion while still attaining a stress equilibrium. Thinner specimens were chosen for this study to increase the likelihood that the specimens reach a quasi-static stress equilibrium.

To further improve the SHPB setup used in this study, the use of larger Helmholtz coils would surely be beneficial. A major constraint within the test setup is that the center of the constructed coils had to fall in line with the pressure bar axis. With an aluminum beam base below the bars restricting the maximum coil flange diameter, the coils had to be made rather small. Another limitation was the ability to obtain quality power supplies for the coils. The 10A switch-mode power supplies used contained the largest current output available for the project budget. Supplying larger currents to the coils would allow one to increase the diameter of the coils, and thus the region of field uniformity, without sacrificing magnetic field strength. In the case of this study, properly supplied larger coils would have allowed their position to be moved to the sides of the aluminum beam base, where their height could then be appropriately adjusted to align with the bars. If one is to improve the test setup by changing the coil power supplies, it is recommended that linear-regulated power is used instead of switch-mode. Switch-mode power is not ideal for sensitive measuring applications like that in this study. Noise generated from the 10A power supplies was evident throughout the entire research process.

It is desired that this study serves the reader by providing another take on the application of velocity gauges in SHPB tests. The test setup used, while cost-effective, enables one to obtain material response data comparable to that of setups utilizing more intricate sensors and analyses. Furthermore, it is desired that this thesis described the application of a linear-viscoelastic model in great detail so that other researchers may

confidently apply similar models to their SHPB testing. Above all, it is desired that this study demonstrated the wealth of knowledge that can be obtained from a single SHPB test event when testing viscoelastic material. This thesis was written using theory that hopefully appeals to those with backgrounds in the field of vibrations. This was done to offer a more comprehensible take on the theory, should someone in this field be unfamiliar with the SHPB test. This was also done to facilitate a continuation of research into the frequency domain complexities that were encountered when dealing with nonlinear data.

Appendix A

A.1 MATLAB Script Used to Process SHPB Test Data


```
%% Velocity Gauge Results Tool
% V.1.1 Feb. 2020
% Author: Garrett S. Wiles
%
% Script to accompany research thesis submitted for the degree of Master of
% Science in Mechanical Engineering at The University of Maryland, College Park

clc
close all
clear all

%% Time Domain Characterization
global t2

%Coil/specimen parameters
As = pi*((15.87E-3)/2)^2; %specimen cross-section area [m^2]
Ls = 3.22E-3; %specimen length [m]

%Bar Properties
E0 = 2.2E9; %pressure bar static Young's modulus [N/m^2]
rho = 1200; %pressure bar density [kg/m^3]
c0 = sqrt(E0/rho); %pressure bar static wave speed [m/s]
Ab = pi*(0.015875/2)^2; %pressure bar cross-section area [m^2]

%Experimental data load
fprintf('\nSelect incident bar voltage data .txt file...\n')
[filename,pathname] = uigetfile('*.txt;','Select incident bar voltage data file.');
file = fullfile(pathname,filename);

data = load(file,'-ascii');
t1 = data(:,1); %time data [s]
E1 = -data(:,2); %voltage data [V]
fprintf('Data recieved.\n')

fprintf('\nSelect transmitter bar voltage data .txt file...\n')
[filename,pathname] = uigetfile('*.txt;','Select transmitter bar voltage data file.');
file = fullfile(pathname,filename);
data = load(file,'-ascii');
t2 = data(:,1); %time data [s]
E2 = -data(:,2);  %voltage data [V]
fprintf('Data recieved.\n')

%apply lowpass filter (cuttoff frequency above amp frequency response)
cofreq = 1.5E5; %cutoff frequency (Hz)
fs = length(t1)/(max(t1)-min(t1)); %data sampling rate
filV1 = lowpass(E1,cofreq,fs);
E1 = filV1;

fs = length(t2)/(max(t2)-min(t2)); %data sampling rate
filV2 = lowpass(E2,cofreq,fs);
E2 = filV2;

v1 = 14.126*E1; %apply calibration constant to voltage signal
v2 = 14.126*E2; %apply calibration constant to voltage signal

figure(1)
f1 = subplot(211);
plot(t1.*1000,v1,'-k')
```

```
title('Incident Bar Gauge Raw Data')
xlabel('Time (ms)')
ylabel('Velocity (m/s)')
grid on
f2 = subplot(212);
plot(t2.*1000,v2,'-k')
grid on
title('Transmitter Bar Gauge Raw Data')
xlabel('Time (ms)')
ylabel('Velocity (m/s)')
linkaxes([f1, f2],'xy');

%input start time of test event (used for offset correction), and the test end time
startInc = input('\nDefine start time of wave measured by incident gauge (for signal↙
offset correction) (ms): ')/1000;
startidx = find(t1>=startInc,1);
endTrans = input('\nDefine end time of test event (ms): ')/1000;
endidx = find(t2<=endTrans,1,'last');
close all

%offset correction amount
offsetv1 = sum(v1(1:startidx))/length(v1(1:startidx));
offsetv2 = sum(v2(1:startidx))/length(v2(1:startidx));

%apply offset correction
v1 = v1-offsetv1; %correct signal offset
v2 = v2-offsetv2; %correct signal offset

%trim voltage and time data
v1 = v1(startidx:endidx);
v2 = v2(startidx:endidx);
t1 = t1(startidx:endidx)-t1(startidx);
t2 = t2(startidx:endidx)-t2(startidx);

figure(1)
set(gcf,'windowstyle','docked');
f3 = subplot(211);
plot(t1.*1000,v1,'-k','LineWidth',2)
title('Incident Bar Gauge')
xlabel('Time (ms)')
ylabel('Velocity (m/s)')
grid on
f4 = subplot(212);
plot(t2.*1000,v2,'-k','LineWidth',2)
grid on
title('Transmitter Bar Gauge')
xlabel('Time (ms)')
ylabel('Velocity (m/s)')
linkaxes([f3, f4],'xy');

global epsdot
epsdot = (v1-v2)/Ls; %specimen strain rate [1/s]

figure(2)
set(gcf,'windowstyle','docked');
subplot(311)
plot(t1.*1000,epsdot,'-k','Linewidth',2)
title('Specimen Strain Rate')
```

```
xlabel('Time (ms)')
ylabel('Strain Rate (1/s)')
grid on

epss = cumtrapz(t1,epsdot); %specimen strain

figure(2)
subplot(312)
plot(t1.*1000,epss,'-k','Linewidth',2)
title('Specimen Strain')
xlabel('Time (ms)')
ylabel('Strain')
grid on

global sigmas
sigmas = rho*c0*(Ab/As)*v2; %specimen stress [Pa]

figure(2)
subplot(313)
plot(t1.*1000,sigmas,'-k','Linewidth',2)
title('Specimen Stress')
xlabel('Time (ms)')
ylabel('Stress (Pa)')
grid on

%apply averaging filter to stress data to smooth stress strain curve (avoid
%large window size)
windowSize = 100;
b = (1/windowSize)*ones(1,windowSize);
a = 1;
filsigmas = filter(b,a,sigmas); %filtered stress data (Pa)

figure(3)
set(gcf,'windowstyle','docked');
% plot(epss,sigmas,'-b')
% hold on
plot(epss,filsigmas,'-k','LineWidth',2)
title('Specimen Stress-Strain Curve')
xlabel('Strain')
ylabel('Stress (Pa)')
grid on

energydis = trapz(epss,filsigmas); %energy dissipation [J/m^3]
fprintf('\nEnergy Dissipated: %.4f kJ/m^3\n',energydis/1000)

%% Frequency Domain Characterization (10 Element GMM Model)
fprintf('\nOptimizing rheological model parameters...\n')
pause(2)

A = [];
b = [];
x0 = [1E7 1E7 1.1E7 1.2E7 1.3E7 1.4E7 1.5E7 1.6E7 1.7E7 1.8E7 1.9E7 1E-4 1E-4 1E-4 1E-4↙
1E-4 1E-4 1E-4 1E-4 1E-4 1E-4]; %initial conditions
lb = zeros(1,21); %parameter lower bounds
ub = [1E8 1E8 1E8 1E8 1E8 1E8 1E8 1E8 1E8 1E8 1E8 1E-1 1E-1 1E-1 1E-1 1E-1 1E-1 1E-1 1E-1↙
1E-1 1E-1]; %parameter upper bounds
options = optimset('TolFun',1E-100,'TolX',1E-100,'MaxIter',2000,'MaxFunEvals',↙
4000,'Display','iter','TolCon',0,'DiffMinChange',1E-12,'DiffMaxChange',1E7); %↙
```

```
optimization options
[x,fval,exitflag,output] = fmincon(@relaxop10,x0,A,b,[],[],lb,ub,[],options); %↙
optimization command
fprintf('Optimization complete.\n')

format long
x(1:11)' %GMM moduli [Pa]
x(12:21)' %GMM relaxation times [s]
fval
output

%GMM parameters
E0 = x(1);
E1 = x(2);
E2 = x(3);
E3 = x(4);
E4 = x(5);
E5 = x(6);
E6 = x(7);
E7 = x(8);
E8 = x(9);
E9 = x(10);
E10 = x(11);
p1 = x(12);
p2 = x(13);
p3 = x(14);
p4 = x(15);
p5 = x(16);
p6 = x(17);
p7 = x(18);
p8 = x(19);
p9 = x(20);
p10 = x(21);

ErGMM = E0+E1*exp(-t2/p1)+E2*exp(-t2/p2)+E3*exp(-t2/p3)+E4*exp(-t2/p4)+E5*exp(-t2/p5)↙
+E6*exp(-t2/p6)+E7*exp(-t2/p7)+E8*exp(-t2/p8)+E9*exp(-t2/p9)+E10*exp(-t2/p10); %↙
relaxation modulus [Pa]
figure(4)
set(gcf,'windowstyle','docked');
plot(t2.*1000,ErGMM,'-k','LineWidth',2)
xlabel('Time (ms)')
ylabel('Relaxation Modulus (Pa)')
title('GMM Relaxation Modulus')
grid on

N = length(t2);
dtau = max(t2)/N; %sampling period [s]
sigmaGMM = conv(epsdot,ErGMM)*dtau; %GMM convolution
sigmaGMM = sigmaGMM(1:N); %GMM-calculated stress [Pa]
figure(5)
set(gcf,'windowstyle','docked');
plot(t2.*1000,sigmas,'-k',t2.*1000,sigmaGMM,'--b','LineWidth',1)
title('Comparison of Experimental Stress and GMM-Calculated Stress')
xlabel('Time (ms)')
ylabel('Stress (Pa)')
grid on
legend('Experimental','GMM')
```

```
f = 1:1:10^5; %frequnecies at which to perform frequency domain analysis [Hz]
w = f.*(2*pi); %frequnecies at which to perform frequency domain analysis [rad/s]
Estar = E0+E1*(1i*w*p1)./(1i*w*p1+1)+E2*(1i*w*p2)./(1i*w*p2+1)+E3*(1i*w*p3)./(1i*w*p3+1)↙
+E4*(1i*w*p4)./(1i*w*p4+1)+E5*(1i*w*p5)./(1i*w*p5+1)+E6*(1i*w*p6)./(1i*w*p6+1)+E7*↙
(1i*w*p7)./(1i*w*p7+1)+E8*(1i*w*p8)./(1i*w*p8+1)+E9*(1i*w*p9)./(1i*w*p9+1)+E10*↙
(1i*w*p10)./(1i*w*p10+1); %complex modulus [Pa]
Eprime = real(Estar); %GMM storage modulus [Pa]
eta = imag(Estar)./Eprime; %GMM loss factor [ul]

figure(6)
set(gcf,'windowstyle','docked')
subplot(211)
loglog(f,Eprime,'-k','LineWidth',2)
title('Frequency Domain Characteristics')
xlabel('Frequency (Hz)')
ylabel('Storage Modulus (Pa)')
grid on
subplot(212)
loglog(f,eta,'-k','LineWidth',2)
title('Frequency Domain Characteristics')
xlabel('Frequency (Hz)')
ylabel('Loss Factor (\eta)')
grid on

function fun = relaxop10(x)
global sigmas t2 epsdot
N=length(t2);
dtau = max(t2)/N; %sampling period [s]
prony = x(1)+x(2)*exp(-t2./x(12))+x(3)*exp(-t2./x(13))+x(4)*exp(-t2./x(14))+x(5)*exp(-t2.↙
/x(15))+x(6)*exp(-t2./x(16))+x(7)*exp(-t2./x(17))+x(8)*exp(-t2./x(18))+x(9)*exp(-t2./x↙
(19))+x(10)*exp(-t2./x(20))+x(11)*exp(-t2./x(21)); %parameterized GMM relaxation modulus↙
[Pa]
sigmaGMM = conv(epsdot,prony).*dtau; %GMM convolution
sigmaGMM = sigmaGMM(1:N); %GMM calculated stress [Pa]

fun = sum((sigmas-sigmaGMM).^2,'all'); %optimization problem objective function for↙
minimization

%live plot of optimization process comparing current iteration GMM stress
%and experimental stress
figure(7)
plot(t2.*1000,sigmas,'-k',t2.*1000,sigmaGMM,'--b')
title('Comparison of Experimental Stress and GMM Calculated Stress')
xlabel('Time (ms)')
ylabel('Stress (Pa)')
grid on
legend('Experimental','GMM')

end
```

Appendix B

B.1 Solid Polyurea Stress-Strain Results

B.1.1 *1850 s^{-1}*

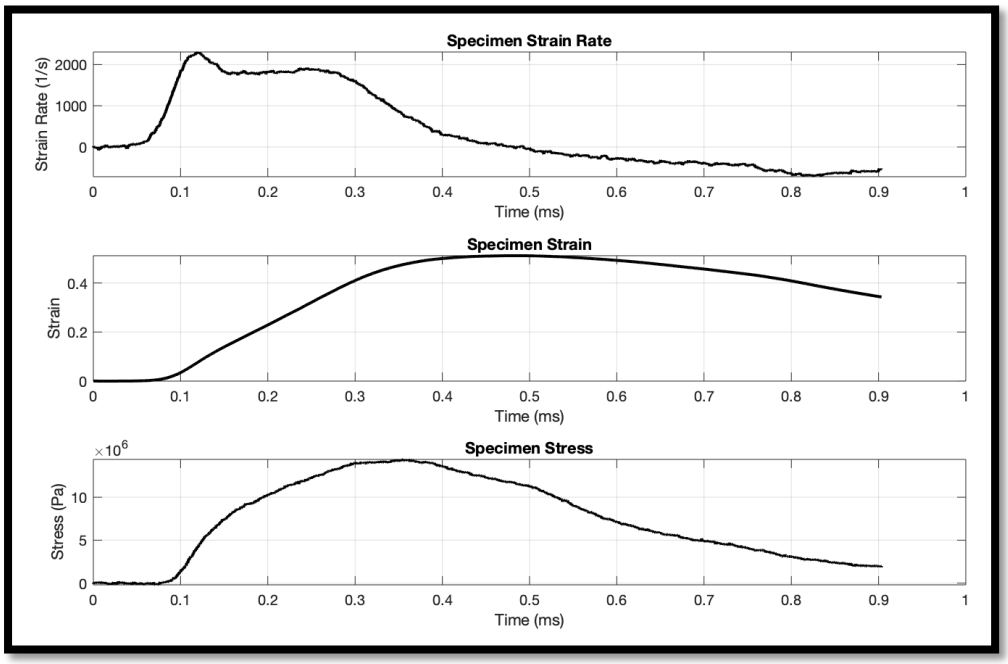

Figure B.1: Solid polyurea stress-strain results for strain-rate of 1850 s^{-1}.

B.1.2 *2200 s^{-1}*

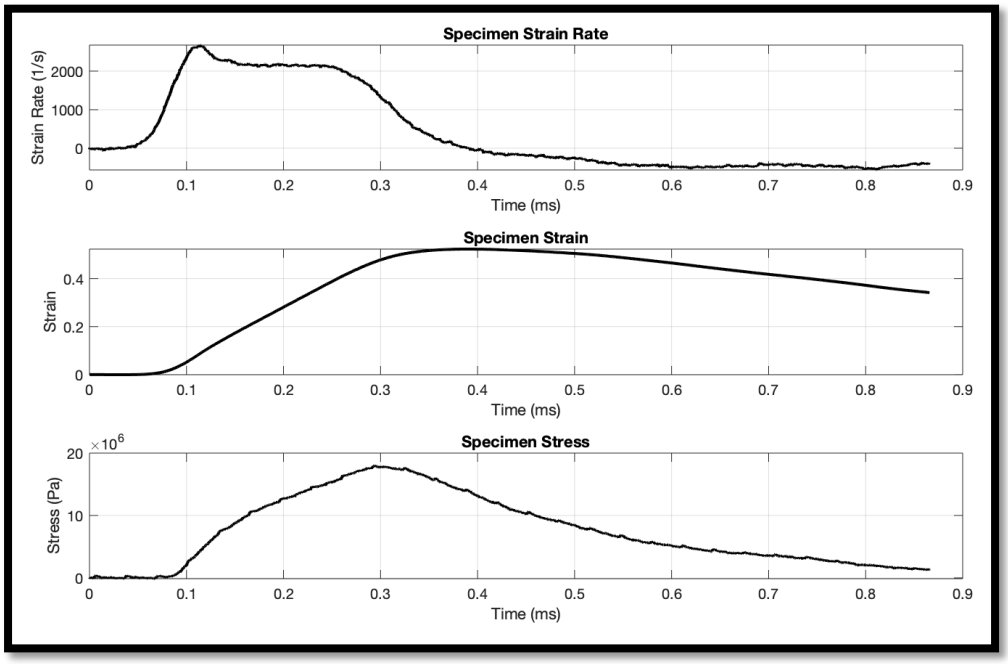

Figure B.2: Solid polyurea stress-strain results for strain-rate of 2200 s^{-1}.

B.1.3 *2900 s^{-1}*

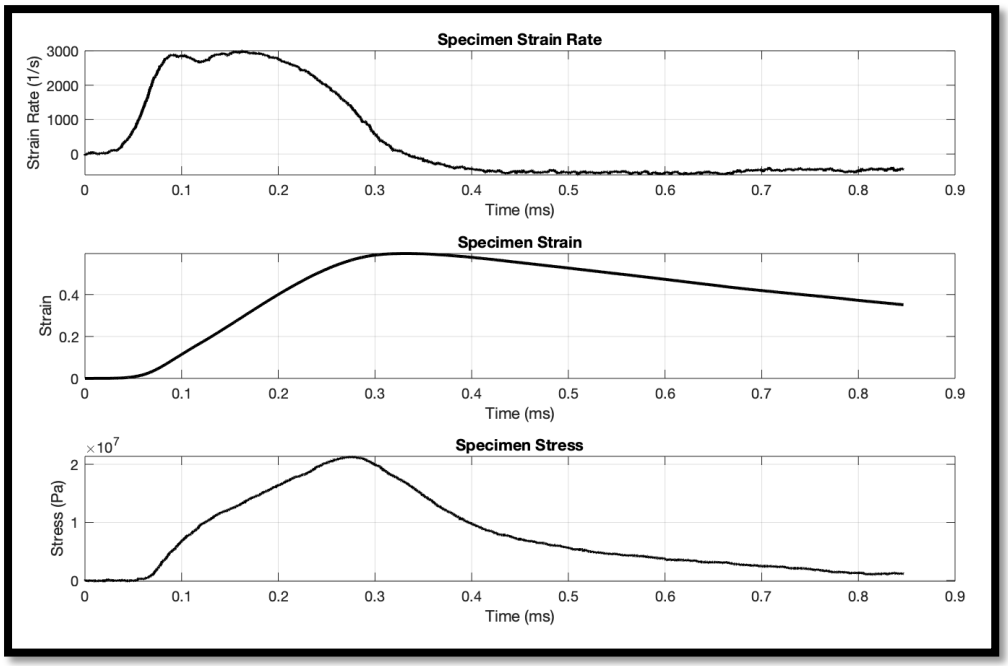

Figure B.3: Solid polyurea stress-strain results for strain-rate of 2900 s^{-1}.

B.1.4 *3300 s^{-1}*

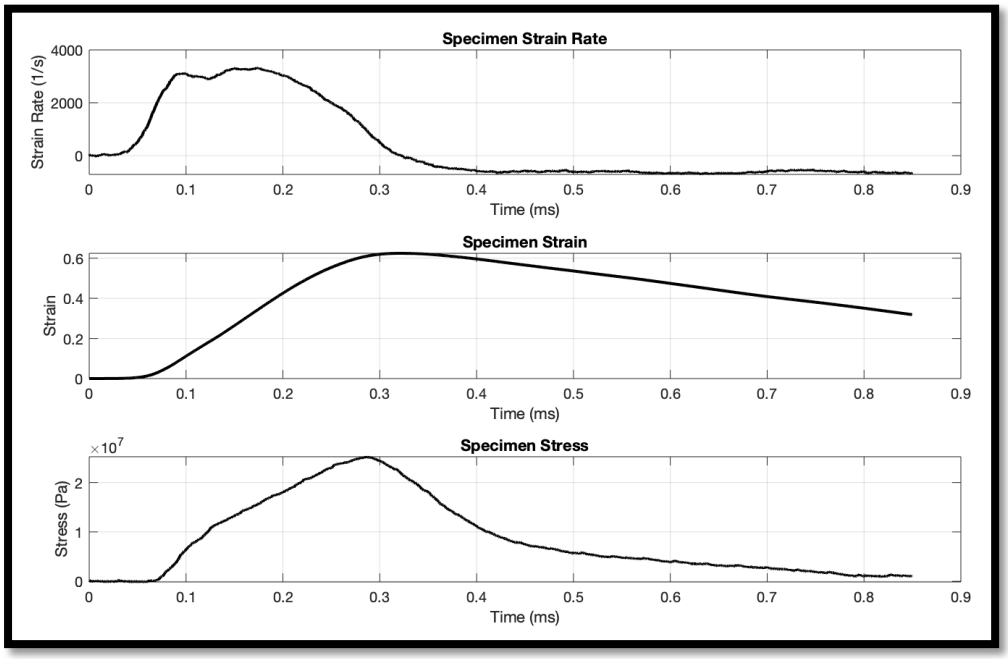

Figure B.4: Solid polyurea stress-strain results for strain-rate of 3300 s^{-1}.

B.1.5 *3500 s^{-1}*

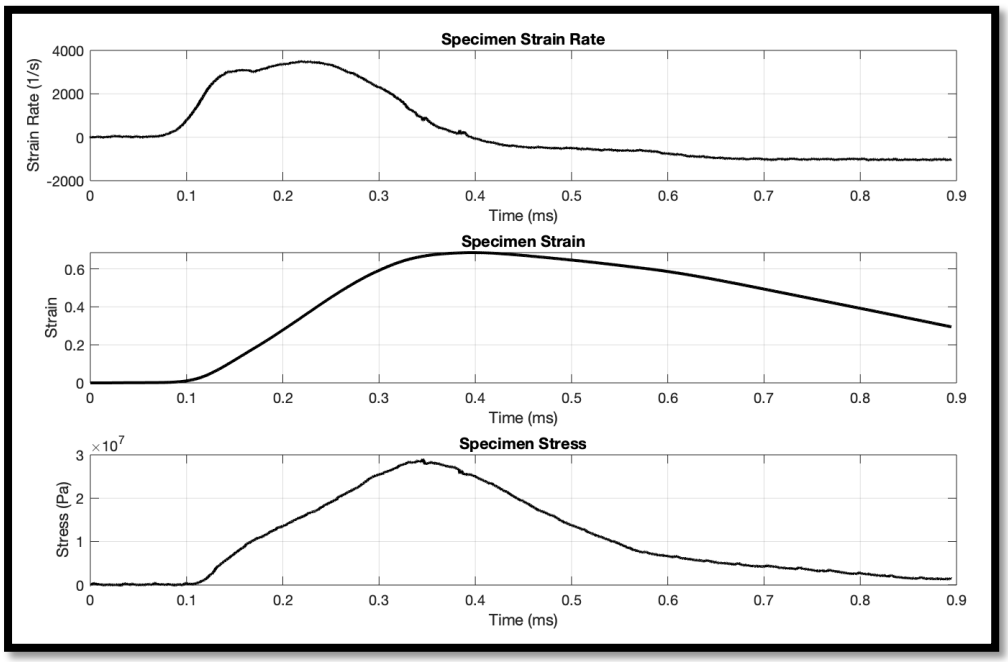

Figure B.5: Solid polyurea stress-strain results for strain-rate of 3500 s^{-1}.

B.1.6 *3800 s^{-1}*

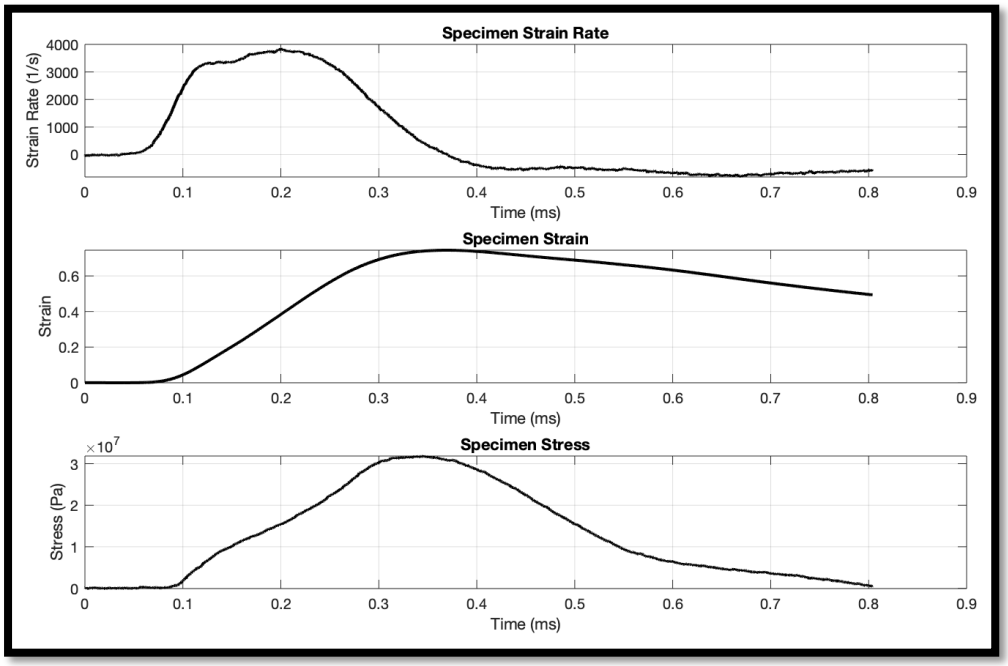

Figure B.6: Solid polyurea stress-strain results for strain-rate of 3800 s^{-1}.

B.1.7 *4300 s^{-1}*

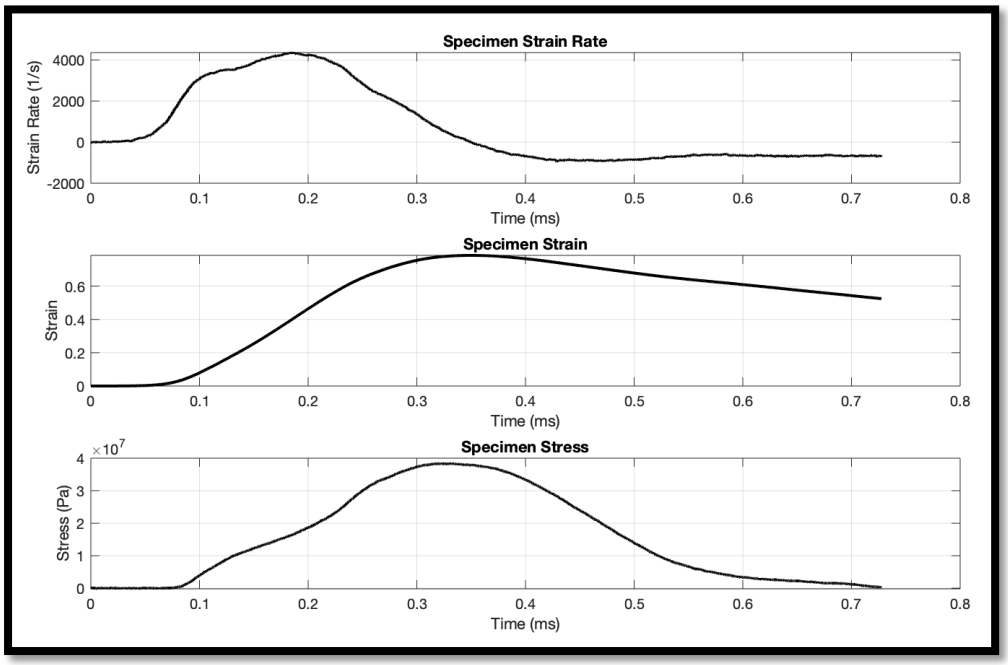

Figure B.7: Solid polyurea stress-strain results for strain-rate of 4300 s^{-1}.

B.1.8 *4600 s^{-1}*

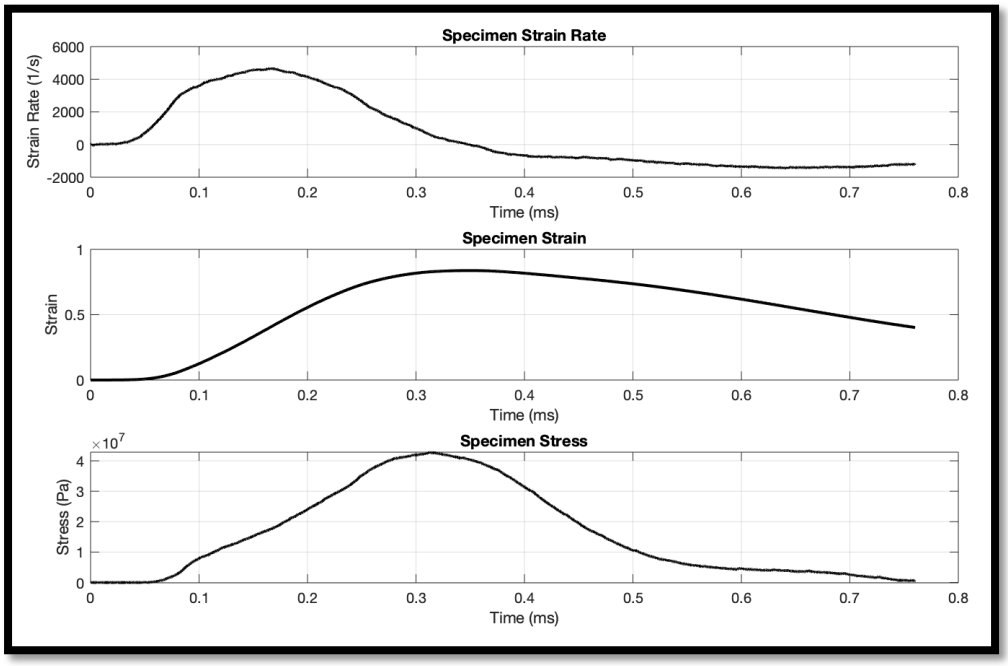

Figure B.8: Solid polyurea stress-strain results for strain-rate of 4600 s^{-1}.

B.2 Banded Polyurea Foam Stress-Strain Results

B.2.1 *2100 s^{-1}*

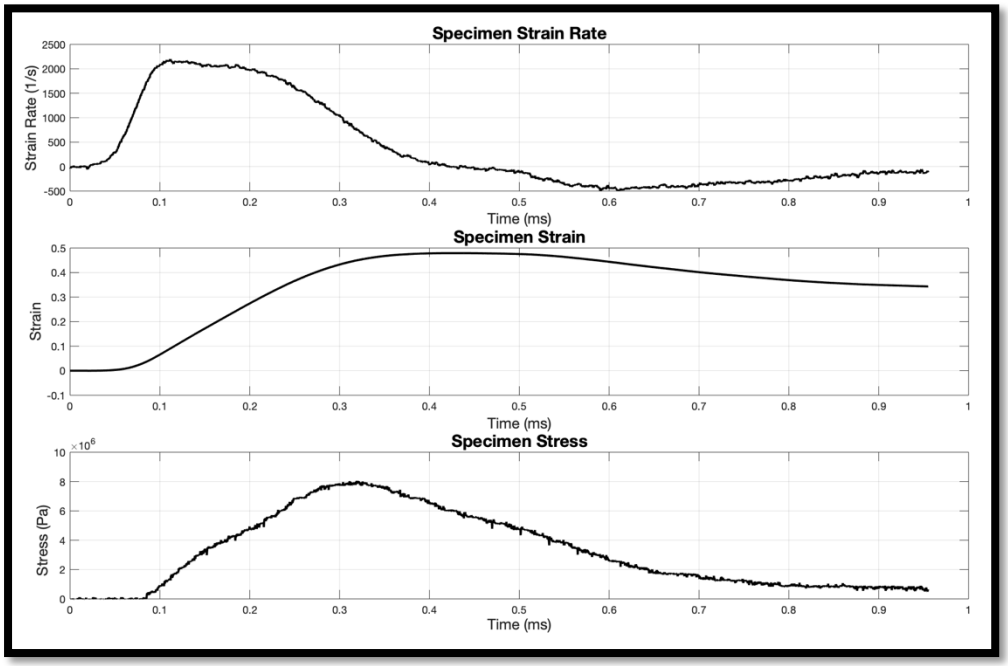

Figure B.9: Banded polyurea foam stress-strain results for strain-rate of 2100 s^{-1}.

B.2.2 *2800 s^{-1}*

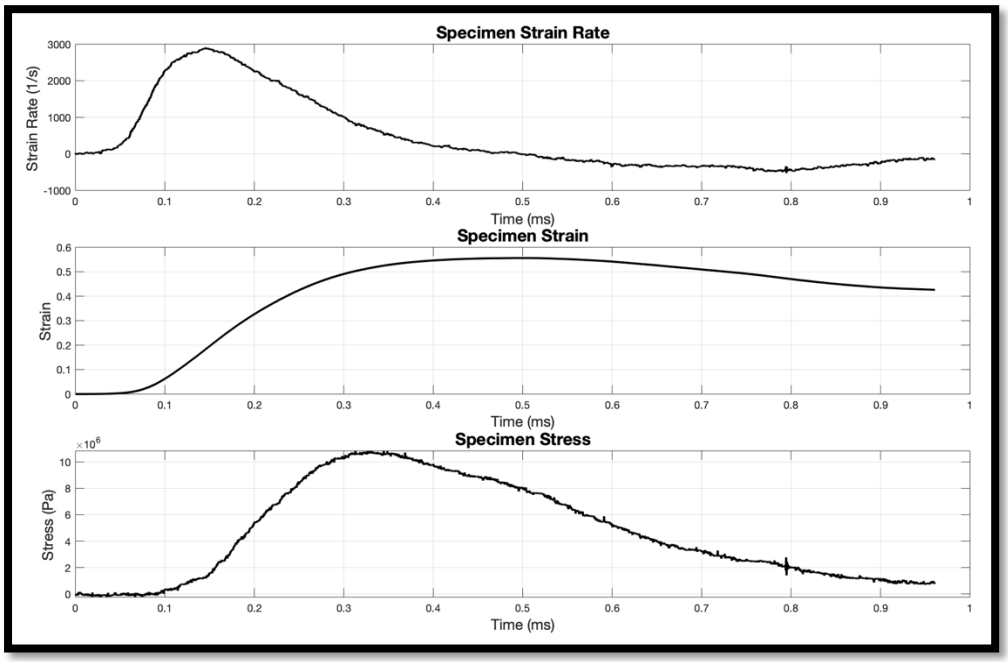

Figure B.10: Banded polyurea foam stress-strain results for strain-rate of 2800 s^{-1}.

B.2.3 *3300 s^{-1}*

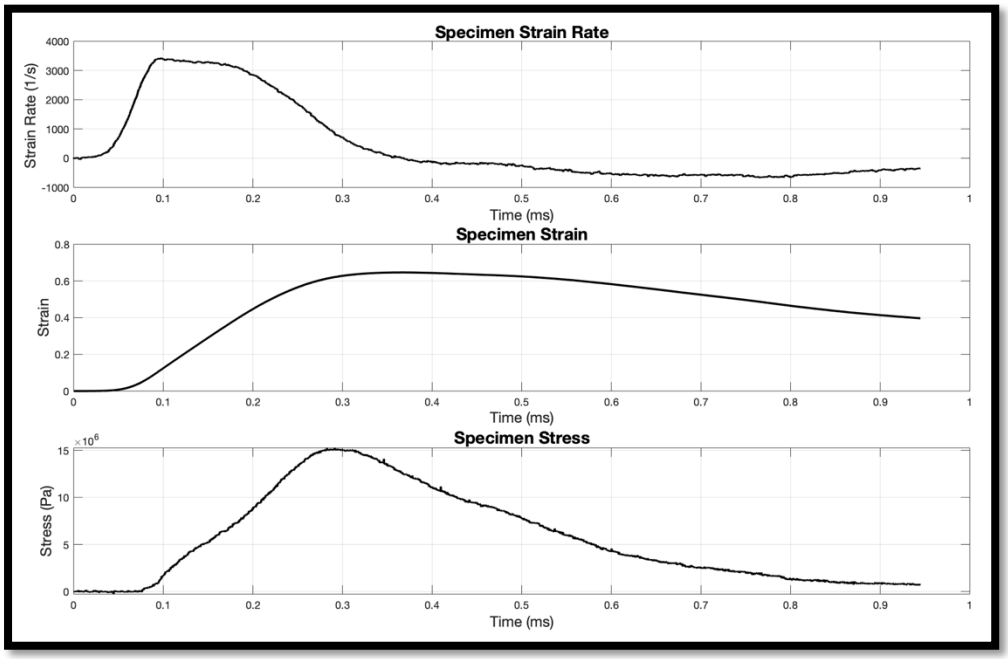

Figure B.11: Banded polyurea foam stress-strain results for strain-rate of 3300 s^{-1}.

B.2.4 *4300 s^{-1}*

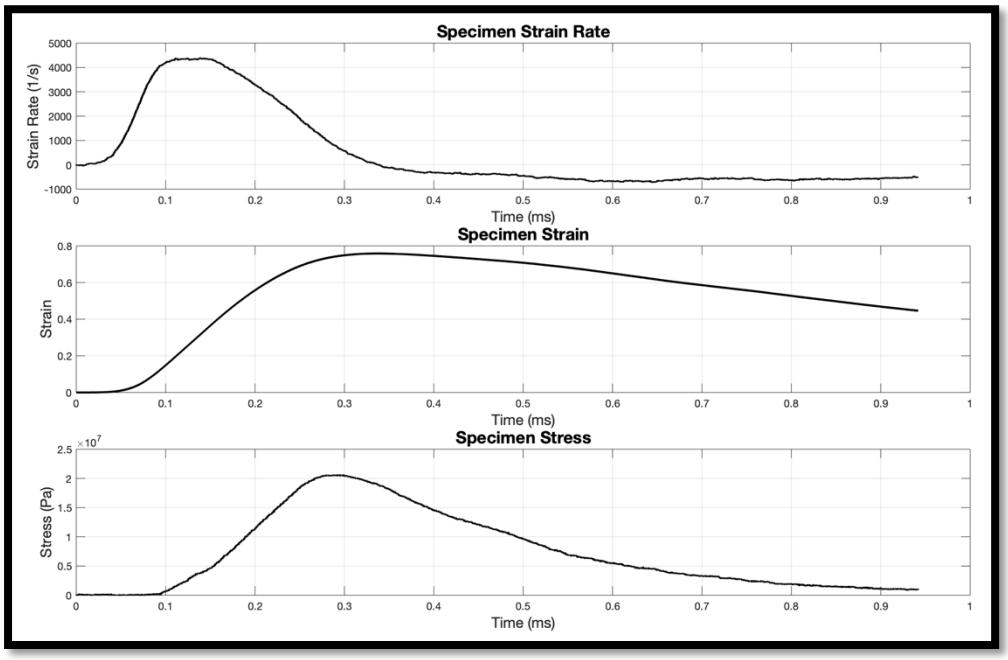

Figure B.12: Banded polyurea foam stress-strain results for strain-rate of 4300 s^{-1}.

B.2.5 *5300 s^{-1}*

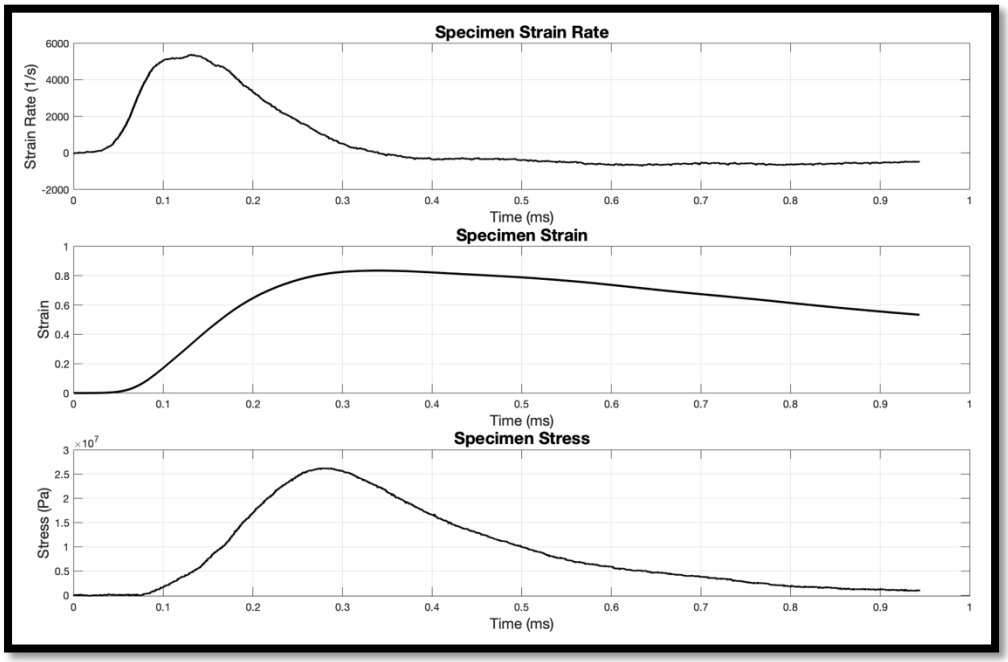

Figure B.13: Banded polyurea foam stress-strain results for strain-rate of 5300 s^{-1}.

B.2.6 *5900 s^{-1}*

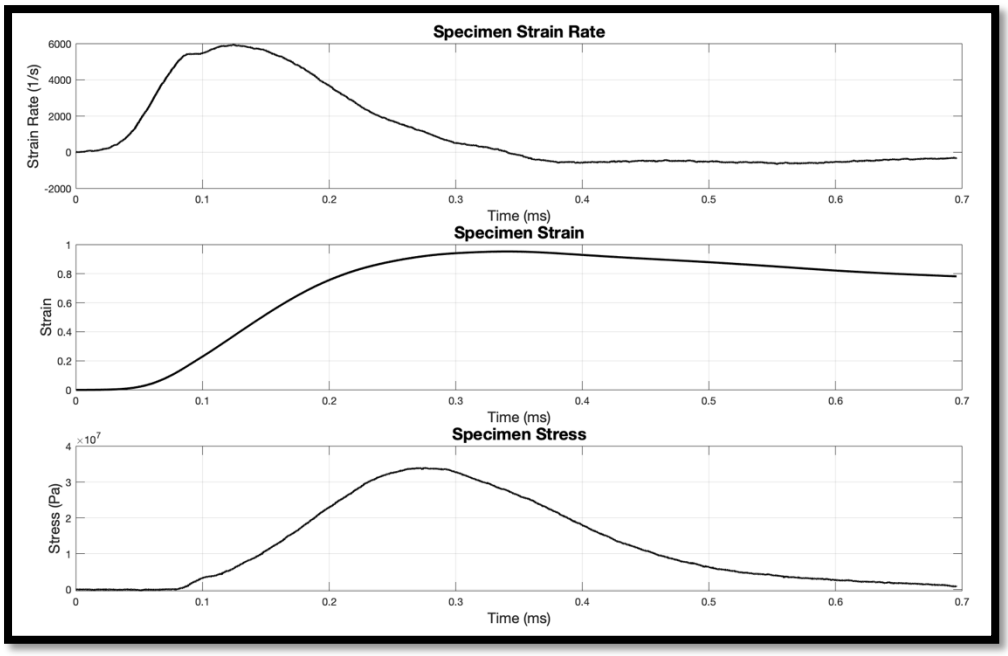

Figure B.14: Banded polyurea foam stress-strain results for strain-rate of 5900 s^{-1}.

Appendix C

C.1 Solid Polyurea Energy Dissipation, GMM Parameter Values, & Model-Calculated Elastic Modulus

Solid Polyurea — = Negligible Terms

Strain-Rate:	1850 s^{-1}				2200 s^{-1}				2900 s^{-1}			
	Energy Dissipation (kJ/m^3):		4178		Energy Dissipation (kJ/m^3):		4817		Energy Dissipation (kJ/m^3):		6375	
	GMM Parameters				GMM Parameters				GMM Parameters			
	Relaxation Times (s)		Relaxation Moduli (Pa)		Relaxation Times (s)		Relaxation Moduli (Pa)		Relaxation Times (s)		Relaxation Moduli (Pa)	
			E_0	1.19824E+07			E_0	1.23301E+07			E_0	1.13437E+07
	ρ_1	1.91022E-04	E_1	1.17266E+06	ρ_1	3.77716E-04	E_1	4.32105E-03	ρ_1	1.87858E-04	E_1	3.66435E+04
	ρ_2	1.89762E-04	E_2	1.21094E+07	ρ_2	1.31854E-04	E_2	6.88487E+06	ρ_2	1.42895E-04	E_2	4.73084E-01
	ρ_3	1.89587E-04	E_3	1.36084E+07	ρ_3	1.31484E-04	E_3	1.99192E+07	ρ_3	1.19145E-04	E_3	1.38566E+07
	ρ_4	9.05842E-05	E_4	1.99700E+07	ρ_4	1.31437E-04	E_4	2.49056E+07	ρ_4	1.19015E-04	E_4	1.37520E+07
	ρ_5	1.58961E-05	E_5	2.10942E+02	ρ_5	4.51680E-05	E_5	7.48000E-06	ρ_5	1.18943E-04	E_5	2.56925E+07
	ρ_6	2.74170E-06	E_6	1.34144E+07	ρ_6	8.62626E-10	E_6	2.03963E+07	ρ_6	4.11675E-06	E_6	1.55258E+07
	ρ_7	3.73253E-10	E_7	1.13296E+07	ρ_7	2.27899E-10	E_7	1.63095E+07	ρ_7	4.73569E-09	E_7	1.32319E+07
	ρ_8	2.48832E-10	E_8	1.95267E+07	ρ_8	2.10851E-10	E_8	9.84527E+06	ρ_8	2.34778E-09	E_8	2.23569E+07
	ρ_9	1.33811E-10	E_9	1.37678E+07	ρ_9	7.03831E-11	E_9	1.45075E+07	ρ_9	1.97549E-09	E_9	1.35078E+07
	ρ_{10}	4.15184E-12	E_{10}	2.97182E+07	ρ_{10}	4.69697E-11	E_{10}	5.17120E+06	ρ_{10}	3.16818E-11	E_{10}	3.54640E+07
	Model-Calculated Elastic Modulus (MPa): $E'(t=0) = E_0 + \sum E_k$ (k = 1:6)			72.26	Model-Calculated Elastic Modulus (MPa): $E'(t=0) = E_0 + \sum E_k$ (k = 1:5)			64.04	Model-Calculated Elastic Modulus (MPa): $E'(t=0) = E_0 + \sum E_k$ (k = 1:6)			80.21
Strain-Rate:	3300 s^{-1}				3500 s^{-1}				3800 s^{-1}			
	Energy Dissipation (kJ/m^3):		7079		Energy Dissipation (kJ/m^3):		8192		Energy Dissipation (kJ/m^3):		9275	
	GMM Parameters				GMM Parameters				GMM Parameters			
	Relaxation Times (s)		Relaxation Moduli (Pa)		Relaxation Times (s)		Relaxation Moduli (Pa)		Relaxation Times (s)		Relaxation Moduli (Pa)	
			E_0	1.35059E+07			E_0	1.25597E+07			E_0	2.11079E+05
	ρ_1	3.46070E-04	E_1	6.30435E+00	ρ_1	1.00000E-01	E_1	3.28499E+06	ρ_1	3.80284E-04	E_1	8.93594E+06
	ρ_2	1.19419E-04	E_2	1.79884E+06	ρ_2	1.99277E-02	E_2	3.90410E+02	ρ_2	3.80264E-04	E_2	2.27629E+07
	ρ_3	1.19350E-04	E_3	1.36929E+07	ρ_3	1.64960E-04	E_3	1.73700E+07	ρ_3	3.80263E-04	E_3	2.26896E+07
	ρ_4	1.19341E-04	E_4	1.56733E+07	ρ_4	1.64939E-04	E_4	2.70854E+07	ρ_4	3.79657E-04	E_4	2.90680E+04
	ρ_5	1.19303E-04	E_5	2.49363E+07	ρ_5	5.65096E-06	E_5	9.56729E+06	ρ_5	6.05430E-11	E_5	8.85555E+01
	ρ_6	5.67260E-08	E_6	5.65034E+03	ρ_6	5.32500E-12	E_6	2.11225E+03	ρ_6	2.04552E-11	E_6	3.27571E+07
	ρ_7	1.03390E-09	E_7	1.43895E+00	ρ_7	4.71000E-13	E_7	1.46205E+07	ρ_7	3.22813E-13	E_7	5.80542E+06
	ρ_8	1.48738E-11	E_8	7.93970E+06	ρ_8	1.16000E-13	E_8	1.43864E+07	ρ_8	2.55623E-13	E_8	1.50588E+07
	ρ_9	8.84277E-12	E_9	1.46264E+07	ρ_9	8.60000E-14	E_9	1.88729E+07	ρ_9	1.72198E-13	E_9	1.21786E+07
	ρ_{10}	6.04970E-13	E_{10}	1.10866E+07	ρ_{10}	1.60000E-14	E_{10}	1.53929E+07	ρ_{10}	4.00000E-14	E_{10}	2.11676E+07
	Model-Calculated Elastic Modulus (MPa): $E'(t=0) = E_0 + \sum E_k$ (k = 1:5)			69.61	Model-Calculated Elastic Modulus (MPa): $E'(t=0) = E_0 + \sum E_k$ (k = 1:5)			69.87	Model-Calculated Elastic Modulus (MPa): $E'(t=0) = E_0 + \sum E_k$ (k = 1:4)			54.63
Strain-Rate:	4300 s^{-1}				4600 s^{-1}							
	Energy Dissipation (kJ/m^3):		10252		Energy Dissipation (kJ/m^3):		12642					
	GMM Parameters				GMM Parameters							
	Relaxation Times (s)		Relaxation Moduli (Pa)		Relaxation Times (s)		Relaxation Moduli (Pa)					
			E_0	3.39531E+05			E_0	1.03113E+07				
	ρ_1	3.21367E-04	E_1	3.73402E+07	ρ_1	2.63669E-04	E_1	1.13855E+07				
	ρ_2	3.21075E-04	E_2	3.18299E+07	ρ_2	2.63647E-04	E_2	3.44919E+07				
	ρ_3	2.23147E-11	E_3	1.92203E+07	ρ_3	2.63626E-04	E_3	4.94297E+06				
	ρ_4	1.04335E-11	E_4	8.66742E+06	ρ_4	2.63474E-04	E_4	4.19175E+06				
	ρ_5	1.01279E-11	E_5	1.05191E+07	ρ_5	2.30279E-04	E_5	2.44156E+02				
	ρ_6	9.43319E-12	E_6	3.55544E+07	ρ_6	1.93900E-09	E_6	1.36785E+07				
	ρ_7	9.17621E-12	E_7	1.22712E+07	ρ_7	1.16781E-09	E_7	1.38826E+07				
	ρ_8	8.73930E-12	E_8	2.22245E+07	ρ_8	8.46696E-10	E_8	1.83056E+07				
	ρ_9	5.31565E-12	E_9	1.71703E+07	ρ_9	3.31622E-10	E_9	1.05648E+07				
	ρ_{10}	4.77146E-12	E_{10}	7.46041E-01	ρ_{10}	2.76698E-11	E_{10}	2.18033E+07				
	Model-Calculated Elastic Modulus (MPa): $E'(t=0) = E_0 + \sum E_k$ (k = 1:2)			69.51	Model-Calculated Elastic Modulus (MPa): $E'(t=0) = E_0 + \sum E_k$ (k = 1:5)			65.32				

Table C.1: Solid polyurea energy dissipation, GMM parameter values, & model-calculated elastic modulus.

C.2 Banded Polyurea Foam Energy Dissipation, GMM Parameter Values, & Model-Calculated Elastic Modulus

Banded Polyurea Foam									= Negligible Terms			
Strain-Rate:	**2100 s^{-1}**				**2800 s^{-1}**				**3300 s^{-1}**			
	Energy Dissipation (kJ/m^3):		1715		**Energy Dissipation (kJ/m^3):**		2105		**Energy Dissipation (kJ/m^3):**		3340	
	GMM Parameters				**GMM Parameters**				**GMM Parameters**			
	Relaxation Times (s)		**Relaxation Moduli (Pa)**		**Relaxation Times (s)**		**Relaxation Moduli (Pa)**		**Relaxation Times (s)**		**Relaxation Moduli (Pa)**	
			E_0	3.10334E+06			E_0	1.73932E+06			E_0	1.25595E+06
	ρ_1	7.50747E-04	E_1	9.36487E+02	ρ_1	4.09683E-04	E_1	8.09941E+05	ρ_1	1.32067E-03	E_1	2.49359E-01
	ρ_2	2.69963E-04	E_2	6.48532E+06	ρ_2	4.09667E-04	E_2	5.96878E+06	ρ_2	8.73924E-04	E_2	6.21858E+06
	ρ_3	2.69836E-04	E_3	3.27165E+06	ρ_3	4.09657E-04	E_3	1.49521E+07	ρ_3	3.34678E-04	E_3	3.07750E+05
	ρ_4	2.69749E-04	E_4	1.14493E+07	ρ_4	4.09627E-04	E_4	1.83239E+06	ρ_4	3.34624E-04	E_4	1.11699E+06
	ρ_5	1.24129E-08	E_5	6.38405E+05	ρ_5	1.61524E-09	E_5	3.67862E+06	ρ_5	3.34571E-04	E_5	4.22239E+06
	ρ_6	2.86196E-09	E_6	2.09735E+06	ρ_6	1.47699E-09	E_6	4.38373E+06	ρ_6	3.34517E-04	E_6	2.31906E+05
	ρ_7	5.23596E-10	E_7	2.16829E+06	ρ_7	1.41796E-09	E_7	9.75974E+06	ρ_7	3.34516E-04	E_7	8.02095E+06
	ρ_8	4.62792E-10	E_8	4.09931E-01	ρ_8	8.93033E-10	E_8	2.00332E+06	ρ_8	3.34492E-04	E_8	6.86733E+06
	ρ_9	2.31915E-10	E_9	9.67877E+05	ρ_9	6.64360E-10	E_9	2.45424E+07	ρ_9	3.27395E-04	E_9	2.38468E+02
	ρ_{10}	7.10000E-17	E_{10}	1.30824E+06	ρ_{10}	4.66268E-10	E_{10}	1.92824E+02	ρ_{10}	2.28275E-04	E_{10}	6.34848E+02
	Model-Calculated Elastic Modulus (MPa): $E^r(t=0) = E_0 + \sum E_k\ (k = 1:4)$			24.31	**Model-Calculated Elastic Modulus (MPa):** $E^r(t=0) = E_0 + \sum E_k\ (k = 1:4)$			25.30	**Model-Calculated Elastic Modulus (MPa):** $E^r(t=0) = E_0 + \sum E_k\ (k = 1:10)$			28.24
Strain-Rate:	**4300 s^{-1}**				**5300 s^{-1}**				**5900 s^{-1}**			
	Energy Dissipation (kJ/m^3):		3712		**Energy Dissipation (kJ/m^3):**		6178		**Energy Dissipation (kJ/m^3):**		10123	
	GMM Parameters				**GMM Parameters**				**GMM Parameters**			
	Relaxation Times (s)		**Relaxation Moduli (Pa)**		**Relaxation Times (s)**		**Relaxation Moduli (Pa)**		**Relaxation Times (s)**		**Relaxation Moduli (Pa)**	
			E_0	4.47888E+06			E_0	5.76119E+06			E_0	2.50000E+04
	ρ_1	4.13574E-04	E_1	1.26212E+01	ρ_1	1.58749E-03	E_1	2.49997E+04	ρ_1	3.36321E-04	E_1	2.58192E+06
	ρ_2	3.65210E-04	E_2	4.24112E+06	ρ_2	2.52062E-04	E_2	3.01833E+06	ρ_2	3.36308E-04	E_2	3.78484E+06
	ρ_3	3.65203E-04	E_3	5.76875E+06	ρ_3	2.52021E-04	E_3	4.59652E+06	ρ_3	3.36285E-04	E_3	5.86660E+06
	ρ_4	3.65196E-04	E_4	7.31560E+06	ρ_4	2.51970E-04	E_4	8.55920E+06	ρ_4	3.36266E-04	E_4	7.47745E+06
	ρ_5	3.65178E-04	E_5	9.21972E+06	ρ_5	2.51959E-04	E_5	9.19783E+06	ρ_5	3.36250E-04	E_5	8.78189E+06
	ρ_6	1.24054E-05	E_6	5.70869E-01	ρ_6	2.51936E-04	E_6	1.02598E+07	ρ_6	3.36241E-04	E_6	9.48261E+06
	ρ_7	6.93947E-08	E_7	1.68443E+02	ρ_7	1.79094E-08	E_7	5.41103E+06	ρ_7	1.03201E-07	E_7	5.71981E+06
	ρ_8	1.59954E-10	E_8	3.84602E+06	ρ_8	1.64125E-08	E_8	6.09195E+06	ρ_8	1.01698E-07	E_8	5.89624E+06
	ρ_9	1.06193E-10	E_9	4.87242E+06	ρ_9	1.35393E-08	E_9	6.04500E+06	ρ_9	3.92678E-08	E_9	5.79971E+06
	ρ_{10}	8.90887E-11	E_{10}	3.15918E+06	ρ_{10}	1.19382E-08	E_{10}	5.93576E+06	ρ_{10}	2.88587E-08	E_{10}	5.73091E+06
	Model-Calculated Elastic Modulus (MPa): $E^r(t=0) = E_0 + \sum E_k\ (k = 1:6)$			31.02	**Model-Calculated Elastic Modulus (MPa):** $E^r(t=0) = E_0 + \sum E_k\ (k = 1:6)$			41.42	**Model-Calculated Elastic Modulus (MPa):** $E^r(t=0) = E_0 + \sum E_k\ (k = 1:6)$			38.00

Table C.2: Banded polyurea foam energy dissipation, GMM parameter values, & model-calculated elastic modulus.

Appendix D

D.1 Banded Polyurea Foam Nonlinearizing Modulus Function Parameter Values

Banded Polyurea Foam						
Strain-Rate:	2100 s^{-1}		2800 s^{-1}		3300 s^{-1}	
	Nonlinearizing Modulus Function Parameters		Nonlinearizing Modulus Function Parameters		Nonlinearizing Modulus Function Parameters	
	α_0	0.9549	α_0	0.5492	α_0	0.6616
	α_1	0.0222	α_1	2.1691	α_1	0.9017
	α_2	-0.0555	α_2	3.0675	α_2	0.8200
	α_3	-0.2031	α_3	3.7600	α_3	0.3786
	α_4	-0.4650	α_4	3.0646	α_4	-0.7093
	α_5	-0.8550	α_5	-1.7032	α_5	-2.6109
	α_6	-1.0937	α_6	-12.5511	α_6	-4.1224
	α_7	0.7719	α_7	6.8378	α_7	3.8884
Strain-Rate:	4300 s^{-1}		5300 s^{-1}		5900 s^{-1}	
	Nonlinearizing Modulus Function Parameters		Nonlinearizing Modulus Function Parameters		Nonlinearizing Modulus Function Parameters	
	α_0	0.6686	α_0	0.3790	α_0	0.6089
	α_1	-0.1310	α_1	3.5604	α_1	-0.8924
	α_2	-0.3341	α_2	2.6687	α_2	-0.9373
	α_3	-0.6331	α_3	1.0596	α_3	-0.9266
	α_4	-1.0175	α_4	-1.3845	α_4	-0.8034
	α_5	-1.3453	α_5	-4.2991	α_5	-0.4478
	α_6	-0.9972	α_6	-5.3493	α_6	0.4168
	α_7	2.4015	α_7	6.0658	α_7	2.4955

Table D.1: Banded polyurea foam nonlinearizing modulus function parameter values.

References

[1] Kolsky, H., 1949, "An Investigation of the Mechanical Properties of Materials at Very High Rates of Loading," Proc. Phys. Soc., **62**(11), pp. 676–700.

[2] Hopkinson, B., 1914, "A Method of Measuring the Pressure Produced in the Detonation of High Explosives or by the Impact of Bullets," Philos. Trans. Royal Soc., **213**(497–508), pp. 437–456.

[3] Davies, R. M., 1948, "A Critical Study of the Hopkinson Pressure Bar," Philos. Trans. Royal Soc., **240**(821), pp. 375–457.

[4] Kolsky, H., 1963, *Stress Waves In Solids*, Dover Publications, New York.

[5] Graff, K. F., 1991, *Wave Motion in Elastic Solids*, Dover Publications, New York.

[6] Chen, W., and Song, B., 2011, *Split Hopkinson (Kolsky) Bar: Design, Testing and Applications*, Springer, New York.

[7] Meirovitch, L., 2001, *Fundamentals of Vibrations*, Waveland Press, Inc., Long Grove, IL.

[8] Baz, A. M. S., 2019, *Active and Passive Vibration Damping*, John Wiley & Sons, Hoboken, NJ.

[9] Casem, D. T., 2000, "High Strain-Rate Testing of Low-Impedance Materials," Dissertation, University of Maryland.

[10] Casem, D. T., 2003, "A Polymeric Split Hopkinson Pressure Bar Instrumented with Velocity Gages," Experimental Mechanics, **43**(4), pp. 420–427.

[11] Fowles, G. R., 1972, "Experimental Technique and Instrumentation," *Dynamic Response of Materials to Intense Impulsive Loading*, Air Force Materials Laboratory, Wright Patterson Air Force Base, Ohio, pp. 405–480.

[12] Wang, J., She, S., and Zhang, S., 2002, "An Improved Helmholtz Coil and Analysis of Its Magnetic Field Homogeneity," Review of Scientific Instruments, **73**(5), pp. 2175–2179.

[13] Akl, W., and Baz, A. M., 2018, "Dynamic Behavior and Damping Characteristics of Carbon Black Polymer Composites at High Strain Rates," Advances in Polymer Technology, **37**(8), pp. 3364–3375.

[14] Brinson, H. F., and Brinson, L. C., 2008, *Polymer Engineering Science and Viscoelasticity: An Introduction*, Springer, New York.

[15] Fan, J., and Chen, A., 2019, "Studying a Flexible Polyurethane Elastomer with Improved Impact-Resistant Performance," Polymers, **11**(3), p. 467.

[16] Fung, Y. C., 1993, *Biomechanics: Mechanical Properties of Living Tissues*, Springer, New York.

[17] Selyutina, N. S., Argatov, I. I., and Mishuris, G. S., 2015, "On Application of Fung's Quasi-Linear Viscoelastic Model to Modeling of Impact Experiment for Articular Cartilage," Mechanics Research Communications, **67**, pp. 24–30.

[18] Pryse, K. M., Nekouzadeh, A., Genin, G. M., Elson, E. L., and Zahalak, G. I., 2003, "Incremental Mechanics of Collagen Gels: New Experiments and a New Viscoelastic Model," Annals of Biomedical Engineering, **31**, pp. 1287–1296.

[19] Provenzano, P. P., Lakes, R. S., Corr, D. T., and Vanderby Jr., R., 2002, "Application of Nonlinear Viscoelastic Models to Describe Ligament Behavior," Biomechanics and Modeling in Mechanobiology, **1**(1), pp. 45–57.

[20] Fung, Y. C., 1972, "Stress-Strain History Relations of Soft Tissues in Simple Elongation," *Biomechanics: Its Foundations and Objectives*, Y.C. Fung, N. Perrone, and M. Anliker, eds., Prentice-Hall, New Jersey, pp. 181–208.